

Analog and Digital Quantum Simulation of Fermionic Systems: Superconducting Emulator Circuits and Effects of Gate Errors

Zur Erlangung des akademischen Grades eines
DOKTORS DER NATURWISSENSCHAFTEN
von der KIT-Fakultät für Physik des Karlsruher Instituts für Technologie (KIT)

genehmigte
DISSERTATION
von

Jan-Michael Reiner, M.Sc.

aus Waiblingen

Tag der mündlichen Prüfung: 25. Januar 2019

Referent: Prof. Dr. Gerd Schön
Korreferent: Prof. Dr. Alexander Shnirman

Nature isn't classical, dammit, and if you want to make a simulation of nature, you'd better make it quantum mechanical, and by golly it's a wonderful problem, because it doesn't look so easy.

— Richard P. Feynman, 1982

List of publications

This thesis is based on the research published in the following three papers:

[1] J.-M. Reiner, M. Marthaler, J. Braumüller, M. Weides, and G. Schön, *Emulating the one-dimensional Fermi-Hubbard model by a double chain of qubits*, Phys. Rev. A **94**, 032338 (2016).

[2] J.-M. Reiner, S. Zanker, I. Schwenk, J. Leppäkangas, F. Wilhelm-Mauch, G. Schön, and M. Marthaler, *Effects of gate errors in digital quantum simulations of fermionic systems*, Quantum Sci. Technol. **3**, 045008 (2018).

[3] J.-M. Reiner, F. Wilhelm-Mauch, G. Schön, and M. Marthaler, *Finding the ground state of the Hubbard model by variational methods on a quantum computer with gate errors*, Quantum Sci. Technol. **4**, 035005 (2019).

These publications are, in that order, the foundations of Chaps. 3, 4, and 5, where they have been modified and extended to a certain degree. Reuse of copyrighted material from these publications is explicitly permitted within this thesis by the respective copyright holders, the American Physical Society (APS) and IOP Publishing Ltd.

Further publications as coauthor:

[4] P. Macha, G. Oelsner, J.-M. Reiner, M. Marthaler, S. André, G. Schön, U. Hübner, H.-G. Meyer, E. Il'ichev, and A. V. Ustinov, *Implementation of a quantum metamaterial using superconducting qubits*, Nat. Commun. **5**, 5146 (2014).

[5] I. Schwenk, S. Zanker, J.-M. Reiner, J. Leppäkangas, and M. Marthaler, *Estimating the Error of an Analog Quantum Simulator by Additional Measurements*, Phys. Rev. Lett. **119**, 240502 (2017).

[6] I. Schwenk, J.-M. Reiner, S. Zanker, L. Tian, J. Leppäkangas, and M. Marthaler, *Reconstructing the ideal results of a perturbed analog quantum simulator*, Phys. Rev. A **97**, 042310 (2018).

[7] J. Leppäkangas, J. Braumüller, M. Hauck, J.-M. Reiner, I. Schwenk, S. Zanker, L. Fritz, A. V. Ustinov, M. Weides, and M. Marthaler, *Quantum simulation of the spin-boson model with a microwave circuit*, Phys. Rev. A **97**, 052321 (2018).

[8] S. Zanker, I. Schwenk, J.-M. Reiner, J. Leppäkangas, and M. Marthaler, *Analyzing the spectral density of a perturbed analog quantum simulator using the Keldysh formalism*, Phys. Rev. B **97**, 214301 (2018).

These papers contain work which is related to the topics discussed in this thesis. The publications are cited in the corresponding text passages.

Contents

1	Introduction	7
2	Theoretical framework	14
2.1	Quantum simulation of fermions via qubits	15
2.1.1	Jordan-Wigner transformation	15
2.2	Analog quantum simulation	17
2.2.1	Tailoring quantum circuits	18
2.3	Digital quantum simulation	20
2.3.1	Quantum gates	21
2.3.2	Trotter expansion	26
2.4	Variational ground state preparation	28
3	Emulating the one-dimensional Fermi-Hubbard model	30
3.1	Mapping the Fermi-Hubbard model onto Qubits	31
3.2	Physical realizations of the qubit chains	33
3.3	Initialization, Readout, Control of the quality	37
3.4	Chapter conclusion	39
4	Effects of gate errors in digital quantum simulations	41
4.1	Error model and method	43
4.1.1	Method and assumptions	43
4.1.2	Effects of gate errors	45
4.2	Example system: Fermi-Hubbard model	48
4.2.1	Fermi-Hubbard model with spin-flip interaction	48
4.2.2	Algorithm and effects of gate errors	49
4.2.3	Scaling up to larger systems	52
4.3	Numerical analysis	56
4.3.1	Verification of the method	56
4.3.2	Comparison of different implementations	58
4.4	Gate fidelity and adiabatic state preparation	60
4.4.1	Fidelity of over-rotated gates	60
4.4.2	Error size in the numerics	62
4.4.3	Adiabatic state preparation	64

4.5 Chapter conclusion	65
5 Variational ground state preparation with gate errors	67
5.1 From the adiabatic evolution to the variational Hamiltonian ansatz (VHA)	68
5.2 Model Hamiltonian and its decomposition	69
5.3 Mapping to qubits and gate sequence	70
5.4 Error model and procedure	72
5.5 VHA versus adiabatic evolution	72
5.6 Scaling up	74
5.6.1 Choice of start parameters	75
5.6.2 Improved results	76
5.7 Chapter conclusion	76
6 Summary and outlook	78
Appendix	83
A Transmon circuit calculations	83
A.1 Tunable transmon	83
A.2 ZZ coupling	84
A.3 XX coupling	88
A.4 Experimental realization	89
Bibliography	92

Chapter 1

Introduction

Today, the term *computer* is a synonym for the modern digital computer that became omnipresent in our every day life. While the history of digital computers begins only as recently as in the 20th century, the earliest computers date back millennia:

In abstract terms, a computer is an purposely build device which receives an input, performs – based on that input – some calculation or operation, and yields the result as output. The earliest examples of such devices are *analog* computers. During the first millennium BC, the south-pointing chariot was invented in China [9]. It was a two-wheeled carriage with a pointer on top that indicated the direction of south, even when the carriage was turned, which was most likely deployed for navigation. Depending on the difference of revolutions of the wheels when the carriage turned, differential gears moved the pointer on top such that it compensated the angle the vehicle was rotated. Hence, it calculated the rotation angle of the carriage based on the rotation of the wheels. Another (more complicated) example is the Antikythera mechanism [10], an ancient (~ 100 BC) Greek orrery that, relying on an elaborate gear box, could predict astronomical positions decades in advance.

The electronic era. Such mechanical analog computers were used throughout history since then, but the technology of analog computers took a tremendous leap forward with the emergence of electrical circuits. The linear electrical elements replaced the mechanical elements of prior analog computers, and far more complex and versatile designs could be achieved. For example, the similarity between electrical current flow and the flow of a fluid made electronic analog computers useful for the simulation of fluid dynamics. More generally, the behavior of electrical circuits is governed by differential equations, hence, they can be employed to simulate such equations. A basic example would be an LC-circuit that resembles a harmonic oscillator.

Electronic analog computers were used by large companies and research facilities until the 1970s, when they were eventually replaced by *digital* computers [11]. Producing computers that encode information into binary bits, and subsequently process that information by applying logical and arithmetic functions on it by the means of logic gates

between the bits, is technologically far more demanding than the analog method. However, once the technology for digital computers became more and more accessible, the digital computer was favored over its analog counterpart due to some clear advantages. Digital computers were more versatile and – more importantly – resilient to noise. The state of a bit can be flawlessly determined by a voltage signal even if the signal is noisy, as long as the noise is below some threshold. For analog computers, the precise value of an analog signal (such as voltage or current) for in- and output is meaningful; any noise directly affects the analog computers accuracy, which becomes more and more tedious when analog devices are scaled up.

Nowadays, analog computers are mostly forgotten; on the other hand digital computers are all the more prevalent. With personal computers and laptops at home and at work, smartphones in our pockets, and where for virtually any object in our every day life a version with integrated chips exist, we became so accustomed to the technology surrounding us, that we rarely truly appreciate how staggering the capabilities of these devices actually are.

Fundamental limitations. However, despite all technological advances, and even though computers keep improving, they do have their limitations. Some problems cannot be solved efficiently by digital computers, since frequently the computation time or required computational resources increase exponentially with the problem size. Many optimization problems are examples for such exponentially scaling problems. Another very difficult task for current computers is the simulation of a quantum-mechanical system, in particular the simulation of fermionic systems:

Consider, e.g., a system of 50 fermionic orbitals. The quantum state of the system is then described by an element of the corresponding Hilbert space, hence, a vector containing 2^{50} complex numbers. Expressing such an amount of complex numbers as double-precision floating-point numbers would yield 18014 petabytes of data, which is more than six times of the 2802 PB of RAM available in today’s (Nov. 2018) most powerful supercomputer, the IBM Summit (or OLCF-4) [12]. Hence, a complete simulation of 50 fermionic orbitals is unfeasible at this point, but 50 orbitals is still tiny in comparison to the number of electrons in chemicals or condensed matter systems. And the underlying problem is clear: If one has constructed a supercomputer that is just able to store the quantum state of 50 orbitals, in order to store 51 orbitals it’s capacity has to double. Similarly, the computation time would also scale exponentially. Even if Moore’s law [13] continues to hold and the computational capabilities of supercomputers will double every one to two years, true large-scale fermionic simulations will remain impractical on such devices.

At the moment, the solution to allow for larger scale simulations is to rely on perturbative or approximative methods. Among the most popular of such approaches are those derived from Hartree-Fock and mean field methods, as well as density functional theory. However, when simulating strongly correlated systems, the full quantum mechanics matter significantly and approximative methods are insufficiently accurate [14].

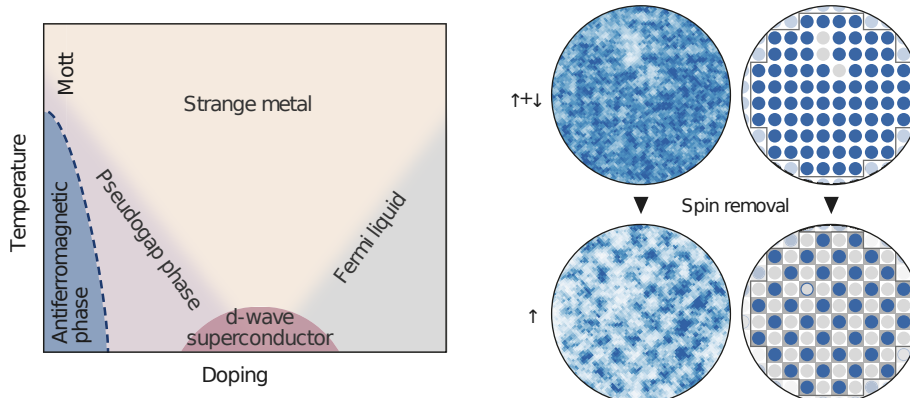


Figure 1.1: On the left is a schematic of the phase diagram of the two-dimensional Fermi-Hubbard model with respect to hole doping and temperature, including predicted phases. On the right, experimental evidence for the antiferromagnetic phase is shown. Depicted are raw and processed microscopy images of a quantum gas in an optical lattice. The particles' interactions and lattice are such that the gas represents a 2D Hubbard model. The pictures show the atomic distribution of a single experimental realization. In the upper part, both spin components are present, in the lower part, the spin-down particles were removed. The observed checkerboard structure indicates that the system was in an antiferromagnetic phase. *Figure from Ref. [16]. Reprinted with permission. Copyright 2017, Nature.*

New technology emerges. The obstacle of simulating exponentially large Hilbert spaces on classical computers calls for a new technology. Based upon precisely this obstacle, Richard Feynman established over three and a half decades ago the notion of harvesting the exponential size of Hilbert spaces as a computational resource, by constructing quantum-mechanical hardware [15]:

What he had in mind, were (in today's language) *analog quantum simulators*, quantum counterparts of the classical analog computers. An analog quantum simulator is an artificial device whose intrinsic quantum-mechanical behavior mimics that of a different quantum system of interest. The system of interest can then be studied with the help of the artificial device that is more controllable and accessible to measurement. Such *quantum emulators* have since become reality, e.g., via ultra-cold gases [16–19] or ion traps [20–22]. In the latter technology, ions are trapped via electromagnetic fields. The ions can then be manipulated such that the interactions among them can then be modified. The former mentioned technology relies on cooling gases of up to hundreds of particles down to ultra-low temperatures until quantum phenomena emerge. Then, the particles can, e.g., be arranged in solid-state like structures via optical lattices formed by lasers [17]. Particles sit in the minima of the potential created through the optical lattice and the particles' interactions define a Hamiltonian that can be equivalent to that of another system of interest. Currently, cold gases and ion traps are the leading platforms for analog quantum simulation, with already impressive results that start challenging classical simulation. An explicit example is the recent realization of a repulsive Fermi-Hubbard model in an optical lattice with circa 80 sites, where doping and temperature could be varied to analyze the phase diagram [16]. In this way, the transition towards a long-range ordered antiferromagnet could be observed and studied, which is shown in Fig 1.1.

At the same time as Feynman's proposal, pioneering work in the field of *digital quantum simulation* (and quantum computing in general) was conducted by Paul Benioff, Yuri Manin, and David Deutsch [23, 24]. Similar to the classical digital computers, digital quantum simulation relies on the application of gates: In conventional computers, information is stored in a register of bits. Sequences of gates acting on a small number of bits at a time implement arbitrary logic or arithmetic operations which allows for generic information processing. In the quantum world, the register consists of quantum bits, or *qubits*, whose state can not only be a certain sequence of zeros and ones, but also be in a superposition or an entangled state. Quantum gates acting on a small number of qubits implement generic unitary transformations on the quantum state of the qubit register. Soon after the introduction of digital quantum simulation, algorithms were proposed that showed computational advantages of quantum hardware over conventional computers. Probably the most famous example is Shor's algorithm for finding the prime factor of large integers [25], which was demonstrated by a small scale quantum computer already in 2001 [26]. This algorithm has exponentially better scaling than all known classical counterparts. Further examples of algorithms with (exponentially) superior scaling in comparison to classical algorithms are database search algorithms [27], or algorithms solving linear equations [28]. In particular, quantum computers can perform the simulation of quantum systems without exponential resource demands [29, 30]. As of today, several realizations of *universal* quantum hardware, i.e., hardware that in principle allows performing any quantum algorithm, have been demonstrated, e.g., with ion traps [31, 32], semiconductor quantum dots [33], or superconducting qubits [34–36].

However, there is one remaining obstacle for digital quantum simulators that needs to be overcome in order to employ them as multi-purpose quantum computers. Unlike classical bits which are resilient to noise, the quantum state of the qubits is affected by finite errors due to decoherence and faulty control. These errors can never be avoided completely, and they are non-trivial to detect since performing measurements would alter the state. However, there are schemes for *quantum error correction*, that can detect and correct errors [37]. Here, many (redundant) physical qubits are combined to form a single *logical* qubit. For the physical qubits – which as quantum two level systems can be represented as spins – errors are modeled by applications of Pauli matrices with a small probability, e.g., the action of σ^x would cause a qubit flip, σ^z would cause a sign change of the phase. One can then, for each specific error, measure operator products of two physical qubits which effectively answer the question: “Has an error of the specific type occurred in one of the qubits?”, hence, projecting the state onto a subspace such that the application of the Pauli operator has in fact either happened or not. No other information is gained, and the qubit state is not altered in any other way. If an error occurred, by repeating the process with other pairs of physical qubits, one can identify the faulty qubit and eventually correct the error. If the error rate for each performed operation is below a certain threshold, this process reduces the overall error in the system; otherwise the scheme would cause more errors than it corrects. Once the threshold has been overcome, the error of the logical qubit can be suppressed further and

further by combining more and more physical qubits. Quantum hardwares with error rates below the threshold for quantum error correction have been demonstrated [34, 35, 38]. However, the devices are only barely below the threshold such that of the order 10^3 to 10^4 or more physical qubits would be needed to form an error-resilient logical qubit. Unfortunately, this is unfeasible for at least the next several years [37, 39, 40].

On the other hand, current quantum hardware – even without error correction – is beginning to enter a regime where it may soon challenge supercomputers. Quantum simulators may even surpass their classical competitors in specific problems, achieving *quantum advantage* [41]. Especially superconducting qubits have made significant progress in the last few years. A decade ago the technology was only at the point of achieving interactions between two qubits [42], whereas now fully controllable quantum processors with up to 20 qubits are accessible through IBM’s quantum experience cloud service [43]. In late 2017 and early 2018, Intel, IBM and Google presented 49, 50, and 72 qubit chips, respectively [44, 45]. While these devices have yet to demonstrate their full capabilities, they show that quantum hardware is now at a point where the size of the Hilbert space they can potentially simulate becomes intractable for classical simulation.

Thesis aim and contents. The goal of this thesis is to study the prospects of near-future quantum devices when operating them without quantum error correction. It focuses on quantum simulation of fermionic systems because of their importance in nature and the difficulties they pose for conventional simulation or analytic calculations. For this purpose, both analog and digital quantum simulators based on qubits are studied. Specifically, superconducting qubits are considered with respect to their use as analog quantum simulators. As for digital quantum simulation, the effects of gate errors on the results of these simulations are studied. In extension to this, the performance of so-called variational algorithms in the presence of gate errors is investigated.

In the following chapter, Chap. 2, the theoretical framework of the thesis is established. At first, it is discussed how to simulate fermionic systems with qubits. The idea is to represent fermionic orbitals – which can be occupied or unoccupied – by qubits as quantum two level systems. However, qubit excitations are bosonic and a mapping of fermions onto qubits is non-trivial. Specifically, the Jordan-Wigner transformation [46], that is employed throughout this thesis, is discussed (with its complications). In the following section, Sec. 2.2, analog quantum simulators and their requirements are explained in more detail. The methods for designing quantum emulators based on superconducting qubits are introduced. These methods will be important for Chap. 3 and the calculations presented in Appx. A. Sec. 2.3 then deals with digital quantum simulation. It is explained what quantum gates are and how they form the building blocks for quantum algorithms. The Trotter expansion [47] is introduced as a tool that helps constructing algorithms simulating complex Hamiltonians with digital quantum simulators. These principles are employed in Chaps. 4 and 5. Finally, Sec. 2.4 explains the concept of variational algorithms which are used in Chap. 5.

Chap. 3 presents a design for an analog quantum simulator of the one-dimensional

Fermi-Hubbard model. The Fermi-Hubbard model has been studied with atoms in optical lattices [16, 48]. In these experiments one can use actual fermionic particles, which allows a straightforward mapping of the artificial system onto the fermionic model of interest. On the other hand, in these systems the available range of coupling strengths, or equivalently of effective temperatures, is limited [16, 49], and it is unclear how to scale up optical traps much further. To avoid these restrictions, superconducting qubits are considered in Chap. 3 as a scalable architecture with broad parameter range. When spin is included, the 1D Fermi-Hubbard model can be mapped onto a double chain of qubits via the Jordan-Wigner transformation. The corresponding qubit system contains XX and ZZ interactions of neighboring qubits along and between the chains, respectively. Two realizations based on superconducting qubits are presented. The first one relies on charge qubits and offers, in principle, the simulation for a very wide parameter range. The second realization utilizes the transmon qubit [50] that is less sensitive to charge noise and is currently the favored superconducting qubit in experiments. Implementations of the necessary couplings on the hardware level are shown explicitly (with the calculations carried out in Appx. A), and the achievable parameter range is analyzed. Both realizations are reviewed with respect to the criteria which an analog quantum simulator should satisfy.

Chap. 4 deals with simulations of fermionic systems based on digital quantum simulators without quantum error correction. While the use of such devices to simulate quantum systems is highly anticipated [41], little research has been conducted to predict effects of unavoidable errors in digital quantum simulations without error correction. In Chap. 4, the effects of gate errors on simulation results are investigated. An error model is established, where gates are interpreted as rotations of the qubit state, and unitary gate errors arise due to stochastic over-rotations (or under-rotations). Based on this model, the *physical meaning* of gate errors in a simulation is analyzed. More precisely, it is analyzed how gate errors lead to the simulation of an altered physical system with a modified Hamiltonian. Depending on the particular algorithm, gate errors may lead to effectively simulated disorder, or they may correspond to unphysical errors, e.g., violating particle number conservation. The analysis is substantiated by numerical simulations of model systems. In addition a relation is established between the strength of the over-rotations and the gate fidelity, a widely used measure for the quality of quantum gates. This allows providing estimates for the maximum number of gates which can be performed with sufficient accuracy with present-day technology.

Chap. 5 investigates the performance of variational algorithms under the influence of gate errors. Such algorithms can be used, e.g., to prepare and analyze the ground state of a Hamiltonian. They are promising candidates for near-future applications of digital quantum computing, because they have been shown to produce good results with relatively low gate counts [51, 52]. On a small scale, successful applications of variational algorithms have already been demonstrated [53, 54] (see Fig. 1.2). These methods operate by introducing variational parameters to a specific algorithm, which are then optimized to maximize the algorithms efficiency. It was expected that errors are

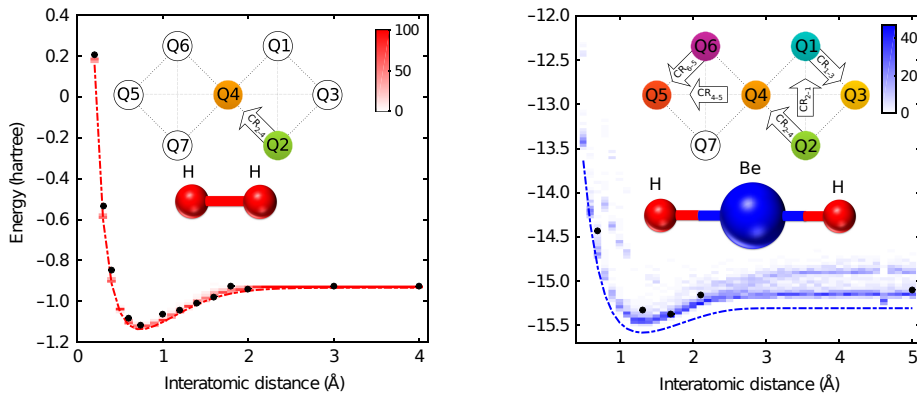


Figure 1.2: Energy surface of H_2 (left) and BeH_2 (right) depending on the interatomic distance. The dotted lines are the exact values. The black dots are the results of digital quantum simulations using a variational algorithm on a superconducting seven-qubit chip from IBM. The qubits which are deployed for the respective simulation are highlighted, as well as which qubits were interacting among each other during the simulation. The shaded area in each plot represents a density plot obtained from (classical) stochastic simulations to predict the experimental results for the applied quantum algorithms. *Figure from Ref. [53]. Reprinted with permission. Copyright 2017, Nature.*

mitigated during this procedure [51], but this has never been shown explicitly. In Chap. 5 the gate error model of the preceding chapter is applied to variational algorithms. The complete procedure of a variational ansatz involving up to 18 qubits is simulated. The results show how quasi-static errors are suppressed within the algorithm. The considered gate error strengths correspond to realistic gate fidelities. Therefore, one can conclude that variational algorithms are indeed a promising application for near-future quantum hardware.

Finally, Chap. 6 provides a summary of the work presented in this thesis, drawing the conclusion and giving an outlook on upcoming developments.

Chapter 2

Theoretical framework

This chapter is a compilation of the theory that is essential to the understanding of the following chapters. Its contents are well known concepts among the community of quantum information and quantum computing. In order to render this thesis more accessible to a broader audience of physicists, the fundamental theory is presented briefly to facilitate the understanding of the presented research.

The first of the below sections, Sec. 2.1, deals with a topic affecting all later chapters. The main theme of the thesis is the quantum simulation of fermionic systems using qubits, a task which requires to encode fermions into qubits. Sec. 2.1 describes the underlying difficulties of this task, and how it is performed throughout this thesis.

The subsequent section, Sec. 2.2, addresses analog quantum simulation and establishes the foundation for Chap. 3 (and the corresponding Appx. A). There, analog quantum simulators based on superconducting qubits are considered. In Sec. 2.2, analog quantum simulators as well as their requirements are examined, and the theoretical means to conceptualize analog quantum simulators based on superconducting qubits are elucidated.

Sec. 2.3 explains the concepts of digital quantum simulation. Quantum gates as the basic elements for digital quantum simulation are introduced, as well as the Trotter expansion which enables handling the quantum simulation of complex systems. This is relevant for Chap. 4, where effects of gate errors in digital quantum simulations are studied.

Finally, Sec. 2.4 introduces variational algorithms, which can be used by digital quantum simulators to prepare the ground state of a model and measure its ground state properties. In Chap. 5, the performance of variational methods is analyzed in the presence of gate errors, with the gate error model already established in the preceding chapter.

2.1 Quantum simulation of fermions via qubits

This thesis focuses on the simulation of fermionic systems, which of course are very important in nature. Understanding fermionic systems is key to unravel a variety of many-body physics or quantum chemistry problems. However, finding the analytic solution of such systems pose an immense challenge, and, as mentioned in the introduction, completely simulating large Hilbert spaces with conventional computers is intractable. On the other hand, due to strong electron correlations, the quantum mechanics of the systems matter to a great extent.

This thesis discusses quantum hardware that is in principle capable of efficiently simulating fermionic systems. The most straightforward way is to perform analog quantum simulations utilizing quantum hardware with actual fermionic excitations, e.g., fermionic ultra-cold gases [16–18]. In contrast, the following work is addressing qubits with bosonic excitations. Examples are the superconducting qubits described in Chap. 3 and Appx. A.1, i.e., either the charge qubit where an excitation corresponds to the tunneling of an additional Cooper pair from a reservoir onto a superconducting island, or the transmon for which excitations are those of an electromagnetic anharmonic oscillator. It is tempting to directly represent a fermionic orbital that can be occupied or empty by a qubit as a two level system. Here, “directly represent” means the annihilation and creation operators of a fermion (which a fermionic Hamiltonian in second quantization is composed of) would be directly replaced by the lowering and raising operators of a qubit. In doing so one faces a difficulty:

The qubits can be described as spins and represented by Pauli matrices. Consider a numbered set of qubits with the lowering and raising operators σ_j^- and σ_j^+ of the j^{th} qubit defined via $\sigma_j^\pm = \frac{1}{2}(\sigma_j^x \pm i\sigma_j^y)$ where σ_j^x and σ_j^y are Pauli matrices. For one qubit we find $\{\sigma_j^-, \sigma_j^+\} = 1$ and $\{\sigma_j^-, \sigma_j^-\} = \{\sigma_j^+, \sigma_j^+\} = 0$ which look like the anti-commutation relations for fermionic annihilation and creation operators. However, for $j \neq j'$ it holds that $[\sigma_j^-, \sigma_{j'}^+] = [\sigma_j^-, \sigma_{j'}^-] = [\sigma_j^+, \sigma_{j'}^+] = 0$, i.e., the operators of different qubits commute, whereas for fermions one would find anti-commuting behavior. Directly identifying a qubit excitation with a fermion would therefore not yield the desired physics in a quantum simulation. Fortunately, there are solutions to this problem.

2.1.1 Jordan-Wigner transformation

One way to map fermions onto qubits is given by the Jordan-Wigner transformation [46]. Here, considering again a numbered set of qubits, one defines the operators

$$c_j = \prod_{k=1}^{j-1} (-\sigma_k^z) \sigma_j^-. \quad (2.1)$$

The product $\prod_{l=k}^{j-1} (-\sigma_l^z)$ of Pauli matrices essentially gives a minus sign for each excited qubit before the j^{th} qubit and thus encodes a fermionic parity. The operator product can be seen as a string of σ^z matrices and is consequently often referred to as Jordan-Wigner



Figure 2.1: Illustration of the problem of non-locality when applying the Jordan-Wigner transformation: On the left is a two-dimensional lattice of eight numbered fermionic orbitals. The Hamiltonian of the system is considered to contain a hopping term between the nearest neighbor orbitals two and six (highlighted in green). On the right is the corresponding qubit lattice consisting of eight numbered qubits. While in the fermionic system, the hopping term is only affecting two neighboring fermionic orbitals, after the Jordan-Wigner mapping this term becomes a complicated five-qubit interaction (highlighted in orange) that exceeds nearest-neighbor couplings.

string. One can check that the newly defined operators obey the relations

$$\{c_j, c_{j'}^\dagger\} = \delta_{jj'} \text{ and } \{c_j, c_{j'}\} = \{c_j^\dagger, c_{j'}^\dagger\} = 0, \quad (2.2)$$

i.e., they obey fermionic anti-commutation relations. Therefore, the Jordan-Wigner transformation allows to encode fermionic operators onto qubits and enables the simulation of fermionic systems using qubits while respecting the correct physical behavior.

However, encoding the fermionic parity in a product of σ^z operators has a particular drawback: Consider the simulation of a system where the Hamiltonian contains hopping terms of the form $c_j^\dagger c_{j'} + c_{j'}^\dagger c_j$ with $j < j'$. Mapping this two-orbital term onto qubits yields

$$c_j^\dagger c_{j'} = \sigma_j^+ \prod_{k=j+1}^{j'-1} (-\sigma_k^z) \sigma_{j'}^-, \quad (2.3)$$

i.e., we obtain a residual Jordan-Wigner string $\prod_{k=j+1}^{j'-1} (-\sigma_k^z)$ such that we end up with an interaction involving not only qubit j and j' but also the qubits with numbers between j and j' . This creates non-locality with terms involving potentially a very large number of qubits, as visualized in Fig. 2.1. In the worst case, a hopping between the first and the last fermionic orbital leads to a qubit term involving all qubits, i.e., the non-locality is of the order of the total number of fermionic orbitals. Therefore, after mapping the fermionic system onto qubits, the qubit Hamiltonian corresponding to the initial fermionic problem may now contain complex multi-qubit interactions which appears difficult to simulate using quantum hardware that usually only features two-qubit interactions. In order to simulate the considered fermionic system one has to find solutions to deal with this issue.

Regarding analog quantum simulation we show in Chap. 3 in the special case of one-dimensional systems with nearest-neighbor hopping one can eliminate Jordan-Wigner strings altogether. Chap. 4 shows explicitly how unavoidable Jordan-Wigner strings can

be treated in digital quantum simulation, which is then also used in Chap. 5.

It should be noted that there are other methods to map fermions onto qubits. For example, the Bravyi-Kitaev transformation uses an encoding with improved locality [55]. Here, the maximum number of interacting qubits per hopping term is of the order of the logarithm of the total number of fermionic orbitals which is exponentially less compared to the Jordan-Wigner transformation. This potentially reduces the requirements for the quantum hardware. But there are the encoding's downsides of being much less transparent and creating overhead at other places, where the Jordan-Wigner transformation does not do so.

The work in this thesis uses throughout the Jordan-Wigner transformation. Its intuitive mapping is beneficial for the designing of analog quantum simulators, where we explicitly show in Chap. 3 how interesting systems can be emulated that are not impaired by Jordan-Wigner strings. The clarity of the transformation also aids the comprehensibility of the analysis in Chap. 4. Finally, as we will argue later, the Jordan-Wigner transformation is in fact very efficient for the digital quantum simulation of Hubbard models considered in Chaps. 4 and 5.

2.2 Analog quantum simulation

As already mentioned in the introduction, analog quantum simulation refers to the simulation of a quantum system of interest by an artificial quantum system that mimics the behavior of the system of interest. In other words, the analog quantum simulator *emulates* the system of interest which is why analog quantum simulation is often called quantum emulation.

More precisely, the quantum mechanics of the artificial system used as emulator are governed by a Hamiltonian that is equivalent to the Hamiltonian of the system of interest. The quantum mechanics of the system of interest can thus be studied by investigating the artificial system.

Since each simulator is purposely build for a specific system of interest, their use appears limited as compared to digital quantum simulators (described below in Sec. 2.3) which are much more versatile. However, this may actually be an advantage: By limiting oneself to a specific system, the emulator may be much less demanding on the quantum hardware, requiring lower overhead, and making the most out of the finite coherence time available in near future quantum devices.

There are requirements one should impose on an analog quantum simulator. In order to be useful an emulator should suffice four criteria [56]:

1. **Relevance:** The emulated systems should be of some relevance for applications or our understanding.
2. **Controllability:** An analog quantum simulator should allow for broad control of the parameters of the emulated system, and for control of preparation, initialization, manipulation, evolution, and detection of the relevant observables of the system.

3. Reliability: Within some prescribed error, one should be assured that the observed physics of the quantum emulator corresponds faithfully to that of the ideal model whose properties we seek to understand.
4. Efficiency: The quantum simulator should solve problems more efficiently than it is practically possible on a classical computer or through analytical calculation.

Examples for analog quantum simulators are cold gases and ion traps. Here, physical particles are manipulated in a controlled fashion such that their actual physical interactions model a particular system of interest. Currently, such simulators are the leading technology for emulation with already impressive results [16–22, 57].

However, at this point it is unclear how to scale up these systems much further, which in the end restricts the size of the emulated systems, limiting their relevance, i.e., the first of the above criteria. Also, even at the very low temperatures where these devices operate the energy scale corresponding to these temperatures is still quite large, or at least comparable, in relation to the intrinsic physical interactions among the particles. Hence, they effectively emulate systems with (high) finite temperature [16, 49], and true low temperature physics remain to be demonstrated. This limits the parameter range available for simulation, i.e., affects criterion 2.

Superconducting circuits are a promising candidate for a scalable architecture that can also operate in the regime of effectively low temperatures. In general, the technology offers great versatility. This thesis focuses on superconducting devices. In Chap. 3 an analog quantum simulator for the one-dimensional Fermi-Hubbard model based on superconducting qubits is presented. There, the four criteria above will also be addressed.

The following section introduces the necessary theoretical techniques to construct an emulator using superconducting hardware as presented in Chap. 3, and specifically in Appx. A.

2.2.1 Tailoring quantum circuits

In order to build an emulator using a superconducting circuit, one has to design the circuit first. Similar to classical electrical engineering one starts by planing the circuit using the lumped element model where the circuit's properties can be calculated.

In superconducting chips dissipative elements, i.e., resistors, will be neglected. We find three different electric components: Placing wires close to each other without contact forms a capacitance between them. A piece or loop of wire intrinsically possesses a certain inductance. Connecting two superconducting wires by a weak link yields a Josephson junction.

These junctions are crucial for qubit designs due to quantum tunneling processes and the non-linear behavior of the junction. They are, e.g., fabricated on chips by applying one layer of aluminium as one wire, letting it oxidize, and putting the aluminium of the second wire on top. Aluminium oxide is an electrical insulator, however, with the appropriate thinness of the oxide layer, tunneling processes are still possible, such that the two superconducting wires are weakly coupled.

Contributions to the Lagrangian:


Kinetic energy:

$$T_C = \Phi_0^2 \frac{1}{2} C \dot{\phi}^2$$



Potential:

$$V_L = \Phi_0^2 \frac{1}{2L} (\phi - \phi_e)^2$$



Potential:

$$V_J = -\Phi_0 I_c \cos(\phi)$$

Figure 2.2: Circuit diagrams of a capacitance C , an inductance L and a Josephson junction J (with critical current I_c) with a phase difference of ϕ occurring across each element. The elements then contribute a kinetic or potential term to the Lagrangian $\mathcal{L} = T - V$ as listed, where T is the sum of all kinetic energies, and V is the sum of all potentials.

The quantum mechanics of non-dissipative circuits can be calculated in the following way [58, 59]:

Every piece of wire in the lumped element circuit is assigned a distinct phase. This phase represents the argument of the complex Ginzburg-Landau order parameter, an appropriate variable for superconducting circuits. This yields a certain phase difference ϕ between two wires that are connected to an electrical element.

Every element will then contribute a certain energy to the Lagrangian of the system depending on the phase difference ϕ across the element, as summarized in Fig. 2.2. A capacitance C gives the kinetic energy $T_C = \Phi_0^2 \frac{C}{2} \dot{\phi}^2$, an inductance L yields the potential energy $V_L = \Phi_0^2 \frac{1}{2L} (\phi - \phi_e)^2$, and a Josephson junction contributes the potential energy $V_J = -\Phi_0 I_c \cos(\phi)$. Here, $\Phi_0 = \frac{\hbar}{2e}$ is the magnetic flux quantum, $\phi_e = \frac{\Phi_e}{\Phi_0}$ is the external phase associated with an external flux Φ_e through the inductance, and I_c is the critical current of the Josephson junction, a structural constant of the junction.

By summing up all kinetic contribution to T and all potential energies to V one obtains the Lagrangian $\mathcal{L} = T - V$ which now depends on all the independent phases of the circuit. The quantum mechanics are found by transforming the Lagrangian to the Hamiltonian of the system, where the new canonical variables are regarded as operators with canonical commutation relations.

The origins of the contributions from the electrical elements according to Fig. 2.2 can be motivated easily. We start by investigating the Josephson junction where the voltage U across and the current I through it obey the Josephson equations

$$U = \Phi_0 \dot{\phi} \quad \text{and} \quad I = I_c \sin(\phi). \quad (2.4)$$

The time integral over the power therefore yields the energy

$$V_J = \int UI dt = -\Phi_0 I_c \cos(\phi), \quad (2.5)$$

as stated above. The Josephson equation for the voltage gives – in combination with the law of inductance $\dot{\Phi} = U$ – a relation between the phase ϕ and the (generalized) flux $\Phi = \Phi_0 \phi$. In fact, a junction in a loop effectively behaves like a (non-linear) inductance.

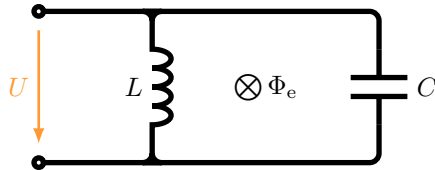


Figure 2.3: Circuit diagram of an LC circuit with inductance L and capacitance C , with a voltage U across the elements. An external magnetic flux Φ_e is passing through the loop.

With the relation for the flux and the first Josephson equation applied on the terms of Fig. 2.2 one obtains the familiar energies $V_L = \frac{1}{2L}(\Phi - \Phi_e)^2$ and $T_C = \frac{C}{2}U^2$. One finds that the Lagrangian composed in the manner proposed above yields equations of motion that represent Kirchhoff's law for the currents.

As an example, consider a simple LC circuit depicted in Fig. 2.3. An inductance L and capacitance C are connected to form a loop with an external flux Φ_e through the loop. Assigning the upper wire the phase ϕ , and the lower (grounded) wire a phase of zero, the above rules yield the Lagrangian

$$\mathcal{L}_{LC} = \Phi_0^2 \frac{C}{2} \dot{\phi}^2 - \Phi_0^2 \frac{1}{2L} (\phi - \phi_e)^2, \quad (2.6)$$

which transforms to the Hamiltonian

$$H_{LC} = \frac{1}{\Phi_0^2} \frac{1}{2C} p_\phi^2 + \Phi_0^2 \frac{1}{2L} (\phi - \phi_e)^2, \quad (2.7)$$

with the canonical momentum $p_\phi = \frac{\partial \mathcal{L}}{\partial \dot{\phi}}$.

Interpreting ϕ and p_ϕ as operators with canonical commutation relations $[\phi, p_\phi] = i\hbar$, one can immediately identify the expected result of an quantum harmonic oscillator with eigenfrequency $\omega = \frac{1}{\sqrt{LC}}$. Comparing the energy contribution of the capacitance, $\frac{1}{\Phi_0^2} \frac{1}{2C} p_\phi^2 = (\frac{2e}{\hbar})^2 \frac{1}{2C} p_\phi^2$, to the familiar form $\frac{Q^2}{2C}$ with the charge Q one recognizes the physical meaning of the canonical momentum; $N = \frac{p_\phi}{\hbar}$ counts the charge in units of $2e$ and is therefore often called the (canonical) charge number operator.

Introducing Josephson junctions as non-linear elements to the circuit creates anharmonicity. This creates distinct distinguishable energy level transitions such that a subspace of two computational levels for a qubit can be well-defined. Chap. 3 and Appx. A rely on such qubits and describes them in more detail.

2.3 Digital quantum simulation

Unlike analog quantum simulators (see above in Sec. 2.2) that emulate one specific quantum system as a whole with all its interactions, digital quantum simulators use a more flexible approach:

The system of interest is encoded into the qubits of the simulator, e.g., the occupa-

tions of fermionic orbitals are represented by excitations of qubits (with the complications described in Sec. 2.1.1). Quantum operations like the time evolution of the system of interest are implemented by a sequence of quantum gates. Quantum gates, described in more detail below in Sec. 2.3.1, are operations acting on usually only one or two qubits. There exist sets with only a limited number of different gates that allow for the approximation of any quantum operation to arbitrary accuracy, and multiple hardware platforms possessing such complete gate sets have been demonstrated [31, 32, 34, 36]. The possibility to encode a variety of systems of interest onto a given number of qubits, and to subsequently simulate the application of any sort of operator, yields the high versatility of digital quantum simulations.

More generally, quantum gate-based calculation is what is usually referred to as quantum computing. In a broader sense, any type of quantum information may be encoded into qubits; complete gate sets allow for the execution of arbitrary arithmetic calculations. The name *digital* quantum simulation stems from the analogy to conventional, classical, digital computing. There, logic gates are performed on bit registers to account for a given computation.

Quantum computers have the advantage over conventional computers that – unlike classical bits – qubits can be entangled and a qubit register can be in a superposition of multiple states. This feature is employed, e.g., in Shor’s algorithm for factoring integers [25]. This famous example provides an exponentially better scaling behavior than any known classical algorithms for the – computationally hard – problem of finding the prime factors of a large integer. The situation is similar for digital quantum simulation. On classical computers, simulating quantum mechanics is computationally hard due to the exponential growth of the Hilbert space with increasing system size. Digital quantum simulators, on the other hand, are efficient at simulating quantum systems [29, 30], because they themselves pose a quantum mechanical system, and their computational power lies within their (large) intrinsic Hilbert space. Since simulating a quantum system with another quantum system has relatively low overhead compared to more abstract gate-based quantum algorithms it is anticipated to be one of the first meaningful applications of quantum hardware [41].

The following subsections describe quantum gates in more detail and introduce the Trotter expansion as a key element to implement digital quantum simulation of large and complex Hamiltonians. These concepts will play a role in Chaps. 4 and 5 which consider digital quantum simulations without quantum error correction. The former chapter establishes an error model for gates and investigates the effect of such errors on a digital quantum simulation. The latter one is expanding the study of this error model onto variational algorithms (see Sec. 2.4).

2.3.1 Quantum gates

Quantum gates are the building blocks of digital quantum simulators in analogy to logic gates in conventional digital computing. Classical gates typically have one or two inputs,

and one output with the result of a logical operation on the inputs. Examples are the gates NOT, AND, OR, as well as NAND. Classical gates are not necessarily reversible. While for a given output of a NOT gate, the input can be reconstructed, this is not true, e.g., for the AND gate: If the output is 1, both inputs were 1, but for an output of 0, all remaining three input scenarios – both inputs 0 or only one of them 1 – are possible. Quantum gates on the other hand have always the same number of inputs as outputs, typically one or two; the input qubits are the same as the output qubits. Quantum computation is always reversible:

Qubits are a quantum two-level system. In gate-based quantum technologies like superconducting circuits which are mostly considered in this thesis, the qubits are bosonic degrees of freedom and can be denoted as spins, where one identifies the spin-up and spin-down states as the computational basis, i.e.,

$$|\uparrow\rangle = |1\rangle \quad \text{and} \quad |\downarrow\rangle = |0\rangle. \quad (2.8)$$

Here, $|\uparrow\rangle$, $|\downarrow\rangle$ are the eigenstates of the σ^z Pauli matrix with $\sigma^z|\uparrow\rangle = |\uparrow\rangle$ and $\sigma^z|\downarrow\rangle = -|\downarrow\rangle$.¹ A register of qubits is therefore an ensemble of spins, the state of the register is given by its wave function that lies in the Hilbert space spanned by the spin ensemble. A quantum gate applies a unitary transformation to a register of qubits, i.e., to the wave function of the qubits, where the transformation acts only on the subspace of the input qubits of the gate. As unitary transformations gates are of course reversible, since an inverse transformation exists.

Applying quantum gates

The unitary transformation is realized by a time evolution of the quantum state of the qubits. It performs the desired gate in the corresponding subspace and applies the unity operation on the rest of the Hilbert space. The Hamiltonian defining the action of the time evolution has to contain the corresponding single qubit terms or multi-qubit interactions such that after a given time the single- or multi-qubit gate is executed. Consider as an example the quantum NOT gate that inverses a qubit, i.e., maps $|1\rangle \mapsto |0\rangle$ and $|0\rangle \mapsto |1\rangle$. The quantum version, that also acts accordingly on superpositions, can be written as a unitary 2×2 matrix, which in the basis $\{|1\rangle, |0\rangle\}$ reads:

$$\text{NOT} = \begin{pmatrix} 0 & 1 \\ 1 & 0 \end{pmatrix}. \quad (2.9)$$

The depiction of a NOT gate in a quantum algorithm is given in Fig. 2.4. It holds that

$$\text{NOT} = \sigma^x = i \cdot e^{-i\frac{\pi}{2}\sigma^x}, \quad (2.10)$$

¹In the quantum information community $|1\rangle$ and $|0\rangle$ are often chosen the other way around such that $|1\rangle$ has the eigenvalue -1 and $|0\rangle$ the eigenvalue 1 , which has certain notational benefits. However, this thesis consistently uses $\sigma^z|1\rangle = |1\rangle$ and $\sigma^z|0\rangle = -|0\rangle$, which might generally be more intuitive for physicists.



Figure 2.4: Examples of a gate depiction in quantum algorithms. The line represents a qubit, where a NOT gate is applied (circled plus in the middle). In some cases, in- and output are given explicitly; here, the input and output state is written to the left and right, respectively, where $|a_0|^2 + |a_1|^2 = 1$.

with the Pauli matrix σ^x of the qubit on which the gate should act. In a multi-qubit space the matrix from Eq. (2.9) would be nested in a Kronecker product of identity matrices accounting for the other qubits. Omitting the global phase,² the exponential in Eq. (2.10) can be realized by a time evolution $e^{-i\tau_{\text{NOT}}H_{\text{NOT}}}$ for a time $\tau_{\text{NOT}} = \frac{1}{g}$ under the Hamiltonian $H_{\text{NOT}} = g\sigma^x$.³

Such a Hamiltonian could for instance be realized in a superconducting circuit based on transmon qubits [50]. Coupling capacitively to a transmon couples to the qubit via the operator σ^x which is also investigated in Chap. 3, resp. in Appx. A.3. Connecting a transmission line by a capacitance allows realizing a Hamiltonian alike H_{NOT} , when a microwave pulse is send through the transmission line with a frequency resonant to the level splitting of the transmon. The energy g in H_{NOT} depends on the value of the capacitance and the pulse strength, applying the pulse for the appropriate time $\tau_{\text{NOT}} = \frac{1}{g}$ yields the correct application of a NOT gate.

The NOT operation initializes of a qubit from its ground state $|0\rangle$ to the excited state $|1\rangle$. Hence, quantum hardware should have some means to perform this operation. Note, that the realization via an external pulse described above creates – by varying g or τ_{NOT} – the means to implement an arbitrary rotation $e^{-i\frac{\varphi}{2}\sigma^x}$ around the x axis with angle φ . In fact, quantum devices usually allow performing arbitrary single-qubit rotations around different axes, i.e., performing an x , y , or z rotation gate with angle φ :

$$R_{x,y,z}(\varphi) = e^{-i\frac{\varphi}{2}\sigma^{x,y,z}}. \quad (2.11)$$

Two-qubit gates

In extension to single-qubit gates, quantum hardware should be able to perform two-qubit gates. An example would be a controlled version of the above introduced NOT gate, i.e., a controlled NOT or in short CNOT, depicted in Fig. 2.5: It applies NOT to a second qubit (the target) if and only if a first qubit (the control) is in state $|1\rangle$. The unitary

²Typically, the global phase of a quantum state is not of particular interest. Also, qubits are usually investigated in a rotating frame, rotating with the qubits eigenfrequency determined by the energy difference of the two computational states. The global phase may be absorbed by a shift of the rotating frame.

³Note, that $\hbar \equiv 1$ is used throughout this thesis in the context of digital quantum computing for convenient notation of time evolution operators.

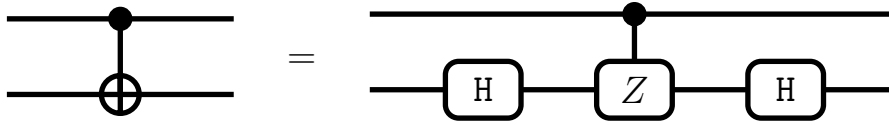


Figure 2.5: Further examples of gate depictions and an example of a gate decomposition. The horizontal lines again represent qubits. On the left, one can see a controlled NOT gate (CNOT), that applies NOT to the lower qubit if and only if the upper qubit is in the state $|1\rangle$. This operation can entangle the qubits (consider the situation where the first qubit is in a superposition). Note, that a CNOT is in fact a controlled application of σ^x , or controlled X gate. On the right, an equivalent gate sequence is presented. Here, a controlled Z gate is applied in the middle, nested in additional Hadamard gates acting on the lower target qubit. The Hadamard gate rotates the lower qubit from the Z to the X basis and back. Therefore, the controlled Z in the new basis is a controlled X (i.e., a CNOT) in the old basis.

operation can be written as a 4×4 matrix which in the basis $\{|11\rangle, |10\rangle, |01\rangle, |00\rangle\}$ reads

$$\text{CNOT} = \begin{pmatrix} 0 & 1 & 0 & 0 \\ 1 & 0 & 0 & 0 \\ 0 & 0 & 1 & 0 \\ 0 & 0 & 0 & 1 \end{pmatrix}. \quad (2.12)$$

To see how such a gate would be applied as a time evolution, one again expresses it as exponential:

$$\text{CNOT} = e^{-i\pi \frac{1+\sigma_1^z}{2} \frac{1-\sigma_2^x}{2}}. \quad (2.13)$$

Here, the indices 1 and 2 belong to the control and target qubit respectively. By expanding the exponent, one can see that along a global phase, a z rotation of the first, and an x rotation of the second qubit, and a $\sigma_1^z \sigma_2^x$ interaction – or ZX interaction – between the qubits needs to be realized.

However, a ZX interaction might not be available on the hardware level. Consider the scenario where only a ZZ interaction is available. In this case, one is able to realize a controlled Z gate, in short CZ: Here, instead of NOT, i.e., σ^x , the Pauli operator σ^z is applied to the target if and only if the control is in state $|1\rangle$. The matrix reads

$$\text{CZ} = \begin{pmatrix} 1 & 0 & 0 & 0 \\ 0 & -1 & 0 & 0 \\ 0 & 0 & 1 & 0 \\ 0 & 0 & 0 & 1 \end{pmatrix}, \quad (2.14)$$

and the gate has a similar exponential expression as the CNOT gate with

$$\text{CZ} = e^{-i\pi \frac{1+\sigma_1^z}{2} \frac{1-\sigma_2^z}{2}}. \quad (2.15)$$

By the means of additional single-qubit Hadamard gates H that transform from the σ^z

eigenbasis to the σ^x eigenbasis and back with the matrix

$$\mathbb{H} = \frac{1}{\sqrt{2}} \begin{pmatrix} 1 & 1 \\ 1 & -1 \end{pmatrix}, \quad (2.16)$$

one can transform a CZ into a CNOT gate, as shown in Fig. 2.5. The transformation of the basis of the target qubit leads to the application of σ^z being equivalent to the application of σ^x without the additional basis transformation, which can be checked by explicit matrix multiplication: $\text{CNOT} = (\mathbb{1} \otimes \mathbb{H})\text{CZ}(\mathbb{1} \otimes \mathbb{H})$, where $\mathbb{1}$ is the 2×2 identity matrix and \otimes the Kronecker product. The Hadamard gate is possible to implement if one has full control over single-qubit rotations since $\mathbb{H} = i \cdot \text{R}_y(\frac{\pi}{2})\text{R}_z(\pi)$.

Gate decompositions and universal gate sets

The above translation between CZ and CNOT is an example of a gate decomposition, where a gate that is not available on the hardware level is applied by a equivalent sequence of gates that are directly implementable. This shows the versatility of the digital quantum computing approach, which extends beyond two-qubit gates:

Consider first the analog in classical digital computing. Famously, any logic function of a number of bits in a register can be implemented solely by a sequence of two-bit operations, specifically NAND gates (or the NOR operations). This feature of the NAND (or NOR) gate is called functional completeness. Another prominent example of a complete set of gates is {AND, OR}, i.e., there is a variety of different possibilities for complete gate sets. Note, that all logic functions are contained in the set of unitary transformations, where additional in- and outputs may be necessary to store additional information such that the gates are reversible [60, 61].

In the scope of quantum computing, a set of gates is called *universal* if any given unitary transformation on a qubit register can be approximatively implemented to arbitrary precision by a finite sequence of gates from that set of gates. A sequence with efficient gate count is guaranteed [62]. There exist a handful of finite gate sets that are explicitly proven to be universal [63]. Note, that finite gate sets can only approximate an arbitrary unitary transformation with a finite gate sequence since the set of unitary transformations is uncountable. There exist also gate sets restricted to only single and two-qubit gates that are *exactly universal*, i.e., they can represent an arbitrary unitary transformation exactly. Probably the most important statement in this context is the fact that the set of all single-qubit gates combined with the CNOT gate is exactly universal [64], which can even be generalized further where the CNOT can be exchanged by any two-qubit gate that is *not primitive*, i.e., can generate entanglement between qubits [65].⁴ Furthermore, the set of single-qubit gates can be represented by the set of

⁴Note that, e.g., $\text{CNOT} \frac{1}{\sqrt{2}}(|1\rangle + |0\rangle) \otimes |0\rangle = \frac{1}{\sqrt{2}}(|11\rangle + |00\rangle)$, i.e., CNOT can map a product state (on the left) to an entangled state (on the right-hand side of the equation).

single-qubit rotations $R_{x,y,z}(\varphi)$.⁵

A variety of quantum hardware platforms have been experimentally realized that have single-qubit control via rotation gates and some physical interaction between two qubits to realize a non-primitive two-qubit gate [31–34, 36]. Hence, these platforms each offer a universal set of gates.

Gate errors

Unfortunately, the application of a quantum gate always contains some small error. The error rate of current hardware is below the threshold for the utilization of quantum error correction [34, 35, 38], where a large number of physical qubits is combined to form one logical qubit, and errors of individual physical qubits may be detected and corrected without destroying the quantum state encoded in the logical qubit. However, with the error rates presently at hand, of the order of 10^3 to 10^4 qubits or more would need to be combined into one logical qubit, which is unfeasible for at least several years [37, 39, 40].

There are two major sources of errors: Errors due to decoherence and errors due to faulty control. Decoherence errors are non-unitary and stem from undesired, yet inevitable coupling of a qubit to external degrees of freedom which affect the qubit state during the time a gate is applied. Unitary control errors can, e.g., stem from imprecise external pulses to apply a gate as described above. Such errors might cause over- or under-rotations, an error model established and thoroughly investigated in Chap. 4, and also Chap. 5 where a variational algorithm (see Sec. 2.4) is considered that reduces gate count and mitigates gate errors.

The question that is addressed in these chapters is how digital quantum simulation may be utilized before full quantum error correction becomes feasible. There, the simulation of quantum-mechanical systems is of particular relevance as a computationally hard problem on conventional computers, that has comparatively low demands on quantum hardware in contrast to general quantum computation and is considered to be one of the first beneficial applications of quantum computing.

With a universal set of gates at hand, in order to simulate the time evolution of complex Hamiltonians, one still has to derive gate sequences that implement such time evolutions. The next section provides an important tool to aid with this task.

2.3.2 Trotter expansion

Consider the situation where one seeks to simulate the time evolution $e^{-iH\tau}$ for the time τ under the Hamiltonian $H = \sum_{\alpha=1}^N H_{\alpha}$ consisting of N sub-Hamiltonians H_{α} . Assume that for each H_{α} a gate sequence implementing $e^{-iH_{\alpha}\tau}$ is known and applicable on a given digital quantum simulator. This is a common situation where the local

⁵Actually, a universal gate set may contain even less gates, namely only one additional single qubit gate in a addition to CNOT [66]. Ultimately, CNOT may be replaced to create a universal gate set consisting of only a single two-qubit gate, since, in fact, almost all two-qubit gates are universal [67]. Such a gate may, e.g., be realized by a controlled rotation with an angle irrationally related to π . However, it is not beneficial to unnecessarily restrict the allowed gates if the hardware is capable of more, since otherwise the gate counts of algorithms will increase, which makes calculations slower and more error-prone.

summands of a Hamiltonian can be realized by interactions between some of the qubits on the hardware. It is also the reason why digital quantum simulation has rather low algorithmic overhead, since the terms of a Hamiltonian often look very similar to the qubit interactions that realize a quantum gate (see Chap. 4).

However, the sequences may not be applicable at once. For example, H_1 could contain interactions between qubits one and two, H_2 between qubits two and three. Since the gate sequences implementing H_1 and H_2 would now involve interactions with qubit number two, they cannot be executed simultaneously. On the other hand, applying the exponentials sequentially rather than simultaneously in general yields a different result since H_1 and H_2 do not necessarily commute.

More precisely, it holds that

$$e^{-iH\tau} = e^{-i\sum_{\alpha=1}^N H_{\alpha}\tau} = \prod_{\alpha=1}^N e^{-iH_{\alpha}\tau} + \mathcal{O}((g\tau)^2), \quad (2.17)$$

where $g = \max_{\alpha} \|H_{\alpha}\|$ is the largest energy scale of the Hamiltonian. This is a corollary of the Baker-Campbell-Hausdorff formula, resp. of the Zassenhaus formula. If the H_{α} do not commute among each other, we find that applying the time evolution under the whole Hamiltonian differs from sequentially applying the sub-Hamiltonians' time evolutions by a term that grows quadratically for larger times τ .

The Trotter expansion allows to simulate the time evolution by decomposing the system into the sub-Hamiltonians without introducing large errors [47]. Here, one splits the time τ into n time slices $\frac{\tau}{n}$. For each time slice one decomposes the time evolution into gate sequences for the individual H_{α} . This process yields an error that scales linearly with $\frac{1}{n}$:

$$\begin{aligned} e^{-iH\tau} &= \left(e^{-iH\frac{\tau}{n}} \right)^n = \left(e^{-i\sum_{\alpha=1}^N H_{\alpha}\frac{\tau}{n}} \right)^n = \left(\prod_{\alpha=1}^N e^{-iH_{\alpha}\frac{\tau}{n}} + \mathcal{O}\left(\left(\frac{g\tau}{n}\right)^2\right) \right)^n \\ &= \left(\prod_{\alpha=1}^N e^{-iH_{\alpha}\frac{\tau}{n}} \right)^n + \mathcal{O}\left(\frac{(g\tau)^2}{n}\right). \end{aligned} \quad (2.18)$$

Hence, for large n , the error is suppressed. The application of the decomposed time evolution for the time $\frac{\tau}{n}$ is called a Trotter step; therefore, the number n is typically referred to as the number of Trotter steps.

Other names for the Trotter expansion are Trotter decomposition, Trotterization, and also Trotter-Suzuki expansion. The latter stems from Suzuki's work on generalizing the decomposition to enhanced schemes such that the error is of arbitrarily high order in $\frac{1}{n}$ [68, 69]. Most prominently, for an even number n , by taking the evolution

$$e^{-iH_1\frac{\tau}{n}} e^{-iH_2\frac{\tau}{n}} \dots e^{-iH_N\frac{\tau}{n}} e^{-iH_1\frac{\tau}{n}} e^{-iH_2\frac{\tau}{n}} \dots \quad (2.19)$$

and reversing the order of the sub-Hamiltonians every other Trotter step, i.e.,

$$e^{-iH_1 \frac{\tau}{n}} e^{-iH_2 \frac{\tau}{n}} \dots e^{-iH_N \frac{\tau}{n}} e^{-iH_N \frac{\tau}{n}} e^{-iH_{N-1} \frac{\tau}{n}} \dots, \quad (2.20)$$

one reduces the Trotter error from $\mathcal{O}(\frac{1}{n})$ to $\mathcal{O}(\frac{1}{n^2})$. This alternation is often possible without large effort. However, higher order decompositions generate cumbersome overhead, i.e., significantly increase the number of gates that need to be performed.

While the Trotter expansion in principle allows for large scale simulations with arbitrary precision, this is only true for error corrected quantum devices. On noisy hardware, increasing the number of Trotter steps leads to longer simulation time and the application of more gates. At some point, the impact of decoherence and gate errors outweigh the benefit of lower Trotter errors such that an optimal number of Trotter steps exists [70]. Chap. 4 studies this in more detail, where, using a particular error model, the effects of gate errors on a Trotterized time evolution are examined.

2.4 Variational ground state preparation

As already mentioned above in Sec. 2.3, quantum gates suffer from finite error rates. Therefore, optimal utilization of near future digital quantum simulators requires the employment of efficient algorithms that make the most out of the limited amount of gates one is able to run without quantum error correction; before the fidelity of the quantum state drops below an acceptable threshold. Variational algorithms are a promising candidate to achieve remarkable results with relatively low requirements on the quantum hardware. Their aim is to prepare the ground state of a system of interest in a quantum simulator. Subsequently, one can extract properties of the ground state, such as the energy, from the quantum device. This is evidently useful for the simulation of quantum mechanical systems, e.g., in quantum chemistry, but also more abstract problems could be encoded into a problem of finding the ground state of a particular Hamiltonian, e.g., optimization problems [71].

The idea behind variational algorithms is the following: Starting point is a quantum state $|\psi_0\rangle$ that is easy to prepare in the quantum simulator. A unitary operator $U(\boldsymbol{\theta})$ depending on a set of parameters $\boldsymbol{\theta}$ is applied and the energy

$$E(\boldsymbol{\theta}) = \langle \psi_0 | U^\dagger(\boldsymbol{\theta}) H U(\boldsymbol{\theta}) | \psi_0 \rangle \quad (2.21)$$

is measured, where H is the Hamiltonian of the system of interest. The procedure is repeated while varying the parameters in order to minimize the energy. Minimizing the energy from equation (2.21) with respect to $\boldsymbol{\theta}$ yields $\boldsymbol{\theta}_{\min}$ such that $E(\boldsymbol{\theta}_{\min}) = \min_{\boldsymbol{\theta}} E(\boldsymbol{\theta})$. Since per definition the ground state is the state with the lowest energy, this should yield $U(\boldsymbol{\theta}_{\min})|\psi_0\rangle$ to be (a good approximation of) the ground state of H – that is under the condition that $|\psi_0\rangle$ and $U(\boldsymbol{\theta})$ are chosen such that an evolution towards the ground state is in principle possible given a suitable set of parameters $\boldsymbol{\theta}$. Hence, the choice of initial

state and unitary operator should have some physical motivation.

There is a multitude of variational methods. The most prominent example of (quantum) variational algorithms is the variational quantum eigensolver [51]. It is based on unitary coupled cluster theory for quantum chemistry problems [72, 73]. Here the initial state is usually the Hartree-Fock state and the unitary operator is effectively a time evolution containing the action of all possible types of hopping terms and interactions. Note, that this ansatz is beneficial even for classical computing and widely used, but the computation time scales exponentially with the number of orbitals in the quantum system. On quantum hardware on the other hand it scales polynomial offering the possibility to simulate much larger systems.

The benefit of variational algorithms for noisy quantum simulators lies in a short runtime on the actual quantum hardware. Only initialization of $|\psi_0\rangle$, application of $U(\boldsymbol{\theta})$ and measurement of $E(\boldsymbol{\theta})$ need to be executed. Afterwards the quantum device is reset. The minimization protocol of adjusting the parameters for a next iteration can be carried out on conventional (super) computers in a quantum-classical hybrid approach. Once optimal parameters $\boldsymbol{\theta}_{\min}$ are found one has – by preparing $U(\boldsymbol{\theta}_{\min})|\psi_0\rangle$ – a protocol for rapid ground state preparation using only marginal resources, such that ground state properties other than the energy may be studied efficiently.

Variational methods are expected to be particularly valuable for quantum simulators without error correction. It is believed that they perform well only using very few gates [52] and errors alike in a Trotter expansion using only a limited number of gates are calibrated out during the optimization of $\boldsymbol{\theta}$. Also errors due to faulty gates should be suppressed [51], which would be very important for noisy simulators.

Chap. 5 analyzes the performance of a variational algorithm inspired by an adiabatic evolution from the non-interacting to the interacting ground state of a system. The algorithm uses particularly few resources and is therefore a viable candidate for near future application. The analysis has a specific focus on the performance under the influence of gate errors with the error model for faulty gates established in Chap. 4.

Chapter 3

Emulating the one-dimensional Fermi-Hubbard model

This chapter is based on the the publication

- [1] J.-M. Reiner, M. Marthaler, J. Braumüller, M. Weides, and G. Schön, *Emulating the one-dimensional Fermi-Hubbard model by a double chain of qubits*, Phys. Rev. A **94**, 032338 (2016).

Reprinting of copyrighted material from this publication is explicitly permitted within this thesis by the American Physical Society (APS).

This thesis revolves around the simulation of quantum systems. As already mentioned in the introduction, this is a difficult task for classical computers because of the exponential growth of the Hilbert space for increasing particle number. This chapter addresses the potential solution for this problem by using *analog* quantum simulators (AQS), or *emulators*. For this purpose one needs to design artificial systems governed by Hamiltonians which can be mapped onto those of the quantum systems to be studied. An example with more than 300 artificial spins with sufficient coherence properties has been realized recently in experiments [57]. In spite of such progress, the strategy of emulating further model Hamiltonians by artificially created systems remains a challenging task.

Of particular interest and in the focus of this thesis, because of the difficulties they pose, are *fermionic* systems. Great progress in the simulation of such systems has been made by using cold atom gases [74] or trapped ions [75–77]. Specifically, the Fermi-Hubbard model has been studied with atoms in optical traps [16, 48]. In these experiments one can use actual fermionic particles, which allows a straightforward mapping of the artificial system onto the fermionic model of interest. On the other hand, in these systems the available range of coupling strengths, or equivalently of effective temperatures, is limited [16, 49]. In addition, the individual control and readout of atoms still poses problems, which makes it difficult to, e.g., read out correlation functions.

Controlled access to individual “particles” is routinely achieved for systems consisting of superconducting qubits. In one dimension, the properties of (spin-less) fermions can be mapped by the Jordan-Wigner transformation onto those of a chain of qubits. In extension to this, the on-site interaction and the hopping of a spin-full 1D Fermi-Hubbard model can be modeled by using a double chain (ladder) structure of qubits with XX (more precisely transversal) and ZZ couplings of neighboring qubits along the chains and between the chains, respectively [78]. This mapping has been exploited in numerical treatments of the problem [79]. Here, we discuss how these systems can be used for the purpose of quantum emulations and analyze different physical realizations of the qubits, including charge qubits and transmons. Josephson junction arrays of charge qubits [80–84] are conceptually the simplest model and allow all needed operations, but they are known to suffer from the random offset charge problem. Transmon qubits [50] are more stable against noise and, therefore, are frequently favored. Their energy splitting can be tuned via a SQUID loop providing the effective Josephson coupling; the ZZ interaction arises due to a mutual inductance, and the XX interaction via a capacitive interaction. On the other hand, when using transmons we find restrictions on the accessible range of parameters of the Fermi-Hubbard model. For both systems it is routinely possible to measure local operators and correlators. By performing several of such measurements one can also gain confidence in the quality of the simulation.

The chapter is organized as follows: In the next section we review how the Hamiltonian of the spin-full one-dimensional Fermi-Hubbard model can be mapped onto the double chain of qubits. Then we discuss the physical realizations of the qubit double chain by superconducting qubits. Finally, we suggest methods of read-out and initialization as well as measurements which allow testing the quality of the emulation. Physical properties of transmon qubits and their coupling required for the simulation are discussed in detail in Appx. A.

3.1 Mapping the Fermi-Hubbard model onto Qubits

Sec. 2.1 already explained how a mapping between fermions and qubit has to respect the different commutation relations between the fermions and the bosonic qubit excitations. We introduced the Jordan-Wigner transformation in Sec. 2.1.1 as a possible mapping of fermionic orbitals that can be occupied or unoccupied onto qubits as quantum two-level systems. Here, for a numbered set of qubit with raising and lowering operators σ_j^\pm one defines

$$c_j = \prod_{k=1}^{j-1} (-\sigma_k^z) \sigma_j^-. \quad (3.1)$$

The operators c_j are now fermionic with the corresponding anticommutation relations.

However, Sec. 2.1.1 also made clear how using this approach, simple hopping terms (in the fermionic language) may translate to complicated multi-qubit interactions. On

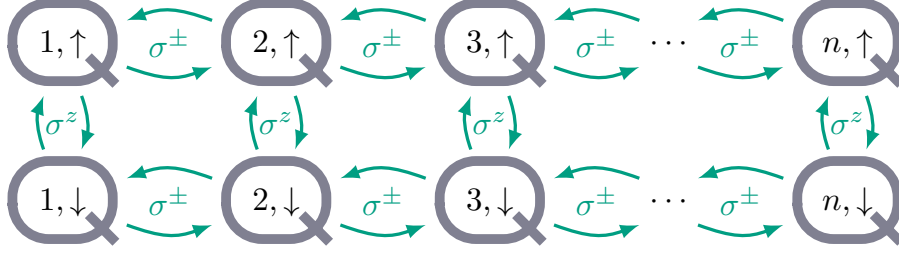


Figure 3.1: Layout of a qubit system consisting of two chains (labeled \uparrow, \downarrow) of n qubits, where the neighboring qubits of each chain are coupled via a SWAP interaction of the form $\sigma_{j,s}^+ \sigma_{j+1,s}^- + \text{H.c.}$ The two chains form a ladder, with qubits belonging to the same rung coupled through terms involving $\sigma_{j,\uparrow}^z \sigma_{j,\downarrow}^z$. With the resulting Hamiltonian H_{QS} (3.3) the qubit system can serve as an analog quantum simulator (AQS) of the 1D Fermi-Hubbard model H_{FH} (3.7).

the other hand, the Jordan-Wigner transformation can be very efficient for one-dimensional systems. From Eq. (3.1) follows, that

$$\begin{aligned} c_j^\dagger c_j &= \sigma_j^+ \sigma_j^- = \frac{1}{2}(\sigma_j^z + 1), \\ c_j^\dagger c_{j\pm 1} &= \sigma_j^+ \sigma_{j\pm 1}^-. \end{aligned} \quad (3.2)$$

This allows for an easy mapping of 1D *spinless* fermionic systems onto a chain of spins as long as the exchange interaction couples only nearest neighbors [85, 86].

Emulating n interacting fermions *with spin-1/2* is possible by using the ladder-type array of qubits displayed in Fig. 3.1 [78, 79]. The qubit system consists of two chains of qubits of length n , with exchange interactions expressed by σ^\pm operators between neighboring qubits in each chain. In addition, the two qubits of the different chains belonging to the same rung of the ladder are coupled by σ^z operators. Assuming that the qubit level spacings ϵ are all the same, and similarly the coupling strengths g^x of the σ^\pm -type couplings as well as the strengths g^z of the σ^z -type couplings, we arrive at the Hamiltonian

$$H_{\text{QS}} = \sum_{j=1}^n \sum_{s=\uparrow,\downarrow} \frac{1}{2} \epsilon \sigma_{j,s}^z + g^z \sum_{j=1}^n \sigma_{j,\uparrow}^z \sigma_{j,\downarrow}^z + g^x \sum_{j=1}^{n-1} \sum_{s=\uparrow,\downarrow} (\sigma_{j,s}^+ \sigma_{j+1,s}^- + \sigma_{j+1,s}^+ \sigma_{j,s}^-). \quad (3.3)$$

The index $(j, s) \in \{1, \dots, n\} \times \{\uparrow, \downarrow\}$ refers to the qubit at the j^{th} position in the upper or lower chain. In order to perform the Jordan-Wigner transformation we need a consecutive, strictly one-dimensional numbering. It can be generated by the bijection $(j, \downarrow) \mapsto j$ and $(j, \uparrow) \mapsto j + n$. Using this and Eqs. (3.2) we can transform the three contributions in the Hamiltonian (3.3). The first sum is easy to treat since

$$\begin{aligned} \sigma_{j,\downarrow}^z &\mapsto \sigma_j^z = 2c_j^\dagger c_j - 1, \\ \sigma_{j,\uparrow}^z &\mapsto \sigma_{j+n}^z = 2c_{j+n}^\dagger c_{j+n} - 1. \end{aligned} \quad (3.4)$$

The ZZ interactions between nonconsecutive qubits is therefore also unproblematic to map onto fermions since

$$\sigma_{j,\downarrow}^z \sigma_{j,\uparrow}^z \mapsto \sigma_j^z \sigma_{j+n}^z = 4(c_j^\dagger c_j - \frac{1}{2})(c_{j+n}^\dagger c_{j+n} - \frac{1}{2}). \quad (3.5)$$

The exchange interaction, on the other hand, only occurs between nearest neighbors in our chosen order, and we find

$$\begin{aligned} \sigma_{j,\downarrow}^+ \sigma_{j\pm 1,\downarrow}^- &\mapsto \sigma_j^+ \sigma_{j\pm 1}^- = c_j^\dagger c_{j\pm 1}, \\ \sigma_{j,\uparrow}^+ \sigma_{j\pm 1,\uparrow}^- &\mapsto \sigma_{j+n}^+ \sigma_{j\pm 1+n}^- = c_{j+n}^\dagger c_{j\pm 1+n}. \end{aligned} \quad (3.6)$$

Using these relations in the Hamiltonian (3.3) and transforming the indices back through $j \mapsto (j, \downarrow)$ and $j+n \mapsto (j, \uparrow)$, one finds that the qubit system is equivalent to the Fermi-Hubbard model in one dimension with the Hamiltonian

$$H_{\text{FH}} = -\mu \sum_{j=1}^n \sum_{s=\uparrow,\downarrow} c_{j,s}^\dagger c_{j,s} + U \sum_{j=1}^n c_{j,\uparrow}^\dagger c_{j,\uparrow} c_{j,\downarrow}^\dagger c_{j,\downarrow} - t \sum_{j=1}^{n-1} \sum_{s=\uparrow,\downarrow} (c_{j,s}^\dagger c_{j+1,s} + c_{j+1,s}^\dagger c_{j,s}). \quad (3.7)$$

The chemical potential μ , the on-site energy U and the transfer energy t are related to the parameters of the qubit system via

$$\mu = -\epsilon + 2g^z, \quad U = 4g^z, \quad \text{and } t = -g^x. \quad (3.8)$$

At this stage we conclude that the considered qubit system with the described XX and ZZ nearest-neighbor interactions is equivalent to the 1D Fermi-Hubbard model (3.7) *including spin* and should allow emulating the latter. We draw attention to the fact that spin flip processes are not allowed (which will be different in Chap. 4). In the following sections we will investigate specific physical realizations of the qubits, including the questions what are the accessible ranges of parameters and what are the available tools for manipulation and measurement.

3.2 Physical realizations of the qubit chains

The spin system shown in Fig. 3.1 with Hamiltonian H_{QS} given by Eq. (3.3), which can serve as an emulator of the 1D spin-full Fermi-Hubbard model, can be realized by superconducting circuits. One possibility is a realization based on an array formed by Josephson charge qubits [80, 81] as pictured in Fig. 3.2. Two nearly degenerate charge states of the superconducting islands are the basis of the charge qubit [82–84]. The islands are coupled via Josephson junctions and capacitances to neighboring ones. The capacitances C^z between islands belonging to the same rung give rise to the ZZ interactions, while the Josephson junctions provide the exchange interactions along the two chains. The junctions have to be designed such that their intrinsic capacitances,

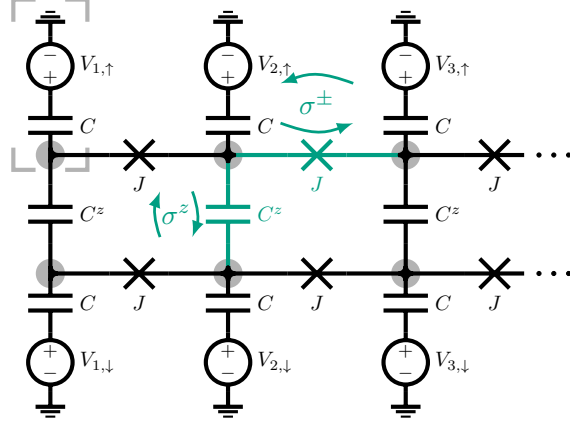


Figure 3.2: Circuit diagram for a physical realization of the quantum simulator of Fig. 3.1 by a ladder array of charge qubits (gray box). Superconducting islands (gray circles) within the same chain are coupled via Josephson junctions J , neighboring islands belonging to the two different chains are coupled via capacitances C^z . Each islands is connected via a capacitance C to a control voltage $V_{j,s}$. Two charge states of the islands form the basis of the qubit. The circuit provides the desired couplings of Fig. 3.1 and allows tuning the chemical potential without further restriction, thus allowing any occupation of the fermionic states.

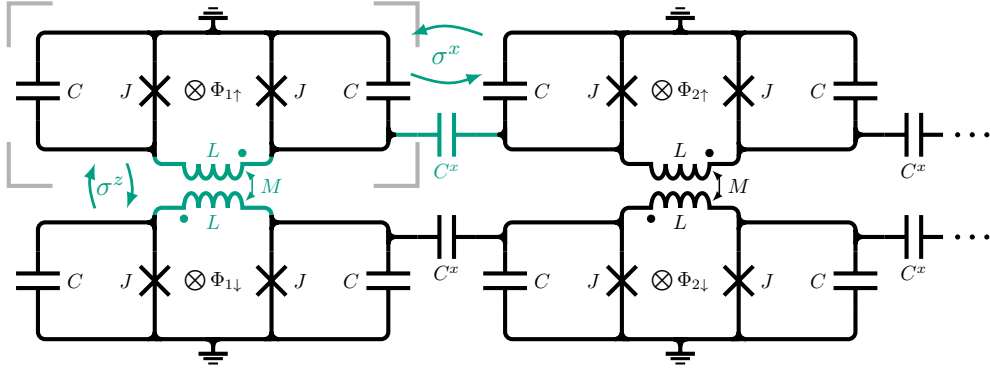


Figure 3.3: Superconducting circuit based on tunable transmon qubits (gray box). Each transmon qubit consists of two Josephson junctions J forming a loop with geometric inductance L ; the junctions are shunted by capacitances C . Each individual transmon is tunable via applied magnetic fluxes $\Phi_{j,s}$ threading the loop. Additional capacitances C^x create an XX coupling between two qubits. Coupling the inductances of two qubits via the mutual inductance M produces a ZZ interaction. The circuit is therefore a realization of the qubit system of Fig. 3.1 (within the rotation wave approximation).

which would lead to unwanted ZZ interaction along the chains, are much smaller than C^z . Each island is further connected via a capacitance C to a gate voltage $V_{j,s}$, which allows adjusting the level spacing of each qubit to the same value ϵ . According to the relation (3.8) this allows tuning the chemical potential μ of the simulated Fermi-Hubbard model (3.7). Equilibrium properties can thus be measured for a wide range of the chemical potential, which also allows studying the important case of half-filling. The values of U and t are fixed during fabrication, but they can be chosen in a wide range. Furthermore, by replacing the Josephson junctions by tunable SQUIDs, one can tune the parameter t .

While the realization via ideal Josephson charge qubits would allow the emulation of the Fermi-Hubbard model in the interesting parameter regime, and conceptually is most easily understood, it suffers from a serious problem. The charge qubits are very sensitive to uncontrolled offset charges and background charge fluctuations. As a consequence it is very difficult to tune the system to a homogeneous chemical potential. This problem has been recognized in the field on superconducting qubits, and the strategy was developed to explore other designs.

An alternative design makes use of qubits with junctions based on phase slip processes [87, 88]. Such phase slip qubits have been fabricated and have been shown to behave in a quantum coherent way [89]. For arrays built of such devices the disorder effects should be much weaker [90]. However, at this time it is too early to judge the quality and potential of these setups. Perhaps the prospects of using them for emulations will encourage further engagement into this new technology.

A successful qubit design, favored nowadays by many experimentalists, is the transmon [50]. It is optimized to be less sensitive to charge noise. We therefore proceed to analyze a circuit based on transmon qubits as shown in Fig. 3.3. In this setup the XX exchange interaction is provided by a capacitive coupling between transmons, and the ZZ -type interaction by a coupling via mutual inductances between the transmons.

In order to explain these couplings we shortly review the properties of a transmon; a detailed derivation is given in the Appendices A.1, A.2, and A.3. One single tunable transmon is built from two Josephson junctions with critical current I_c (here assumed to be equal) and phase differences ϕ_1 and ϕ_2 across them. Each junction is shunted by a capacitance C , and they form a loop with low geometric inductance L . We introduce the external phase $\phi_e = \frac{2e}{\hbar} \Phi_e$ associated with the external flux Φ_e through the loop containing the junctions, and the energy scales $E_C = \frac{e^2}{2C}$, $E_J = \frac{\hbar}{2e} I_c$, and $E_L = \frac{\hbar^2}{e^2 L}$.

For small geometric inductance L , such that $E_L \gg E_J$, the difference ϕ_- of the phases across the two junctions is confined in a very steep potential well and effectively fixed at the value of the external phase. Through this mechanism, the energy difference of the two logical states of the transmon $\epsilon = \sqrt{8E_C E_J} \cos(\phi_e/2)$ is tunable via the external flux.

By coupling the inductances of two qubits (labeled \uparrow and \downarrow) to form a mutual inductance M as shown in Fig. 3.3, we couple their potentials, and attain an effective

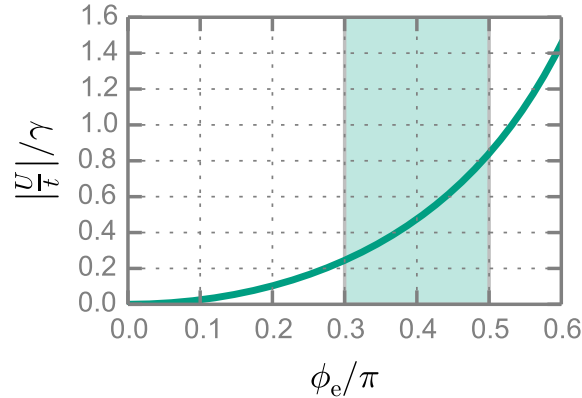


Figure 3.4: For a quantum simulator realized by transmon qubits, the parameter U/t of the Fermi-Hubbard model (3.7) to be emulated is plotted against the external phase ϕ_e (assuming all external fluxes to be equal). The shaded area indicates the accessible range for ϕ_e , and γ is a scaling factor (see main text).

interaction of the form $g^z \sigma_{\uparrow}^z \sigma_{\downarrow}^z$. The resulting coupling energy scale is

$$g^z = -\frac{1}{16} \frac{M}{L} \tan\left(\frac{\phi_{\uparrow}}{2}\right) \tan\left(\frac{\phi_{\downarrow}}{2}\right) \frac{\epsilon_{\uparrow} \epsilon_{\downarrow}}{E_L}, \quad (3.9)$$

where $\phi_{\uparrow, \downarrow}$ are the phases associated with the external fluxes through the qubits. The coupling energy g^z is now tunable through the external phases $\phi_{\uparrow, \downarrow}$, and even the sign of g^z can be changed. Since $g^z \propto \epsilon_{\uparrow} \epsilon_{\downarrow} / E_L \propto E_J / E_L$, the coupling energy is very low. For it to be above the qubit linewidth one has to use transmon designs with not too low inductance. A possible experimental realization with substantial inductance is the concentric transmon qubit [91] (see Appx. A.4 for details).

To achieve the XX -type interaction between two transmons we suggest a coupling via the charge operators through the capacitances C^x (see Fig. 3.3). For low coupling capacitances, $C^x \ll C$, we find an interaction of the form $g^x \sigma_j^x \sigma_{j+1}^x$ between nearest neighbor qubits with

$$g^x = \frac{1}{4} \frac{C^x}{C} \epsilon. \quad (3.10)$$

Since $|g^x| \ll \epsilon$ the rotating wave approximation can be used, and we reproduce the exchange interaction in Eq. (3.3).¹

The AQS built in this way has an important feature: The tunability of g^z through external fields enables to tune the ratio U/t of the parameters of the Fermi-Hubbard model. Figure 3.4 displays a plot of $|U/t|$ over the external phase (which is assumed to

¹Note that this result is only valid in first order, and terms in $\mathcal{O}((C^x/C)^2)$ have been dropped. They would lead to finite-range interactions decaying proportional to $(C^x/C)^k \sigma_j^x \sigma_{j+k}^x$. While it appears interesting to include interactions beyond nearest neighbors, one should note that such couplings in the qubit system do not map to a meaningful interaction in the fermionic system through the Jordan-Wigner transformation.

be equal for all qubits). After absorbing the parameters of the circuit elements into the scaling factor $\gamma = \frac{C}{C^x} \frac{M}{L} \frac{\sqrt{8E_C E_J}}{E_L}$ we find a universal behavior. The shaded area indicates (roughly) the allowed range of values of the external phase: If we choose ϕ_e too small the value of g^z will drop below the qubit linewidth, if we choose it too large, the transmons' susceptibility to noise increases. The sign of U can be switched by reversing the external flux in either the upper or the lower chain of qubits, hence, we can simulate repulsive or attractive on-site interactions.

Both types of couplings discussed here have energies that are small compared to the qubit energy splitting, i.e., $|g^x|, |g^z| \ll \epsilon$. For transmons this restriction is needed, since they are effectively anharmonic oscillators and the coupling strengths have to be weaker than the anharmonicity. Otherwise excitations of energy levels higher than the two logical states of the qubits play a role. This imposes a serious restriction on the parameters of the Fermi-Hubbard model (3.8), namely it effectively amounts to $\mu \sim -\infty$. This means we can explore equilibrium properties of the system only in the limit of very low particle number.

We are, however, able to excite in a controlled way some of the qubits in the system and therefore initiate particles in the AQS. If the frequencies of the qubits to be excited are initially tuned far from the other ones in the AQS, and then tuned again to degeneracy adiabatically after the excitation, we should arrive in the ground state of the Fermi-Hubbard model with a given number of particles. Furthermore, after initiating specific excitations in the AQS, we can study the resulting non-equilibrium properties. This is especially interesting, as such properties are hard to treat either analytically or numerically. For these nonequilibrium dynamics there is no restriction on the filling of the system; i.e., we cover a wider range of parameters than in the equilibrium case.

3.3 Initialization, Readout, Control of the quality

The fabrication process of the transmon Josephson junctions is not precise enough to guarantee the Josephson energies to be exactly equal (on the energy scale of the couplings). On the other hand, the qubit energies of the emulator's qubits have to be degenerate. For this reason, the proposed circuit in Fig. 3.3 includes separate magnetic fields to tune individually each transmon. This extension should be manageable, adding one DC connection for each of the transmons to create the local fields. In addition, the individual tunability is useful for the initialization and readout, as well as for protocols to be used as tests of the quality of the simulation.

As an initialization scheme we suggest to couple a part of the qubit system capacitively to a transmission line as a feed line for external signals. By pairwise detuning the qubits in this part the XX interaction between the transmons can be suppressed, which allows addressing every qubit individually through a resonant microwave pulse. Hence, one can excite specific qubits to initialize a desired configuration of excitations in the AQS. Note, that the ZZ interaction may only lead to an effective frequency shift for the excitation of a qubit, depending on whether the partner qubit is already excited

or not. Bringing the transmons back to degeneracy turns the XX exchange interaction back on, which will start the simulation.

Readout can be performed through the usual method of projective measurement in the dispersive regime. We couple resonators to the system, with frequencies far from the qubit frequencies during the simulation. Individual qubits are then tuned out of degeneracy to enter the dispersive regime of a resonator. This way, we can measure the time evolution of the operator σ^z for each transmon.

An important issue to address is the quality of the results produced by the AQS [56] (see criterion 3 in Sec. 2.2). The Emulator does not have error correction implemented. Deviations of the qubit system, where disorder effects cannot be avoided, from the ideal model Hamiltonian (3.3) will modify conclusions to be drawn for the Fermi-Hubbard system, a problem which is largely unexplored. Here we propose tests which may help gaining confidence through several sorts of measurements.

(1) One option is to check symmetries of the system. In our case, it is easy to see from the Hamiltonian (3.7) that the total number of excitations in the spin-up as well as the spin-down chain should be conserved separately. Furthermore, both chains should be equal, hence equal properties should be observed in both chains. In addition, for a sufficiently large system with negligible boundary effects, we expect translational symmetry along the chains.

(2) If one creates fermions only in one of the chains (by exciting the corresponding qubits), one finds effectively a tight-binding model. In this case, the simulation results could be easily compared to analytic results.

(3) Another option is to limit the system size of the AQS such that results could be compared to simulations on a classical computer. To do this, one does not need to build a small emulator. Rather, by tuning the coupling strengths it is possible to switch off the exchange interaction along the chains at a specific position. This will localize the excitations in one part of the simulator, and a comparison between the measurements of the smaller subsystem with numerical simulations could be possible.

Such measurements help in evaluating the quality of the emulator's results. Beyond such tests one should investigate the effects of disorder in the parameters of the emulator. First steps in this direction show for certain models (including the Fermi-Hubbard model) a remarkable stability of the AQS against disorder, which arises due to the symmetries [92].

A limitation of the proposed emulator arises due to the limited coherence time of the qubits. But we estimate that qubit designs are available with sufficient quality to simulate the quantum state evolution on interesting, long time scales before decoherence dominates the dynamics. The effects of a bath coupled to a quantum emulator have been investigated in part [5, 6, 8, 93] but need to be explored further. For a first estimate we have to compare the microscopic time scales with the decoherence time, or inversely, the coupling energies with the decoherence rate. For example, for the Xmon qubit coherence times of the order of $10\ \mu\text{s}$ to $100\ \mu\text{s}$ were reported [94], corresponding to rates from $100\ \text{kHz}$ down to $10\ \text{kHz}$. These rates are orders of magnitude smaller

than the capacitive coupling energies ranging from 10 MHz to 100 MHz. While this ratio looks very promising, we have to note that it is unclear how the required magnetic coupling can be realized with the Xmon design. Therefore, we concentrated in this chapter on the concentric transmon [91], for which coherence times of the order of 10 μ s and capacitive coupling energies between 10 MHz and 100 MHz appear possible as well, and which allows for the magnetic coupling. First estimates for the magnetic coupling between two adjacent qubits yielded results only slightly above the decoherence rate, but proper adjustments in the circuit could provide sufficiently strong coupling energies (see Appx. A.4).

An actual quantity of interest in an emulation is a time- and space-dependent correlation function of the Fermi-Hubbard model on time scales which significantly exceed the microscopic time scales given by the inverse of the hopping matrix elements and the interaction strength. Accordingly, the correlation functions of the qubit circuit should be studied for times significantly exceeding the equivalent microscopic time scales determined by the inter-qubit couplings (3.8). These time scales have to be compared with the coherence time of the $2n$ -qubit double chain circuit. In the extreme case, if we are interested in long-range correlation functions, say of sites at opposite ends of the system, the relevant coherence time is reduced by a factor $2n$ as compared to the single-qubit coherence time. Thus, even with very promising ratios between single-qubit decoherence rates and coupling strengths, the study of long-range correlation functions is more difficult. But for not too large n (say between 10 and 100) it should be possible to study with present technology the time dependence of correlation functions in an interesting regime. We finally note that with our proposed emulator we are potentially in a more favorable situation than with a digital quantum computer (without error correction), where the simulation of the time evolution requires executing a very large number of quantum gates making the limitations due to the finite coherence time much more serious.

3.4 Chapter conclusion

A double chain of qubits with XX and ZZ couplings of neighboring qubits along and between the chains, respectively, can be mapped via the Jordan-Wigner transformation on a spin-full 1D Fermi-Hubbard model. The qubit system can thus be used to emulate the quantum properties of this model. It constitutes a different approach to analog quantum simulation with, e.g., fermionic ultra-cold gases [16, 48], or a recent effort with an emulator based on dopant atoms in a semiconductor [95]. We analyzed different physical implementations of such analog quantum simulators. The conceptually simplest, with the broadest range of available parameters and highest flexibility is a realization based on an array of Josephson charge qubits. It would also allow simulations corresponding to half-filling of the fermionic problem. Unfortunately, Josephson charge qubits suffer from the strong dependence on background charge fluctuations, which makes them difficult to handle in experiments. An alternative would be provided by using junctions based on

phase slip processes [87–89]. For arrays built with such devices disorder effects should be much weaker [90] which should make it worthwhile investing into this new technology. Because they are widely used nowadays, we discussed in detail tunable transmon qubits, where the ZZ interaction arises due to an inductive coupling and the XX interaction due to a capacitive interaction. This appears a promising approach as far as the experimental realization is concerned, and therefore it is discussed in more detail in Appx. A.4. Although for this realization the parameter range is restricted, we could propose several interesting scenarios to be explored in an emulation, including protocols which can provide confidence in the results of the simulation through measurements of local operators.

We focused in this chapter on analog quantum simulation. One should note that superconducting qubits are on the other hand also a prime candidate for digital quantum simulation of the Fermi-Hubbard model [96, 97]. In the next chapter, we will switch from studying emulators to investigating digital quantum simulation of fermionic systems.

Chapter 4

Effects of gate errors in digital quantum simulations

This chapter is based on the the publication

[2] J.-M. Reiner, S. Zanker, I. Schwenk, J. Leppäkangas, F. Wilhelm-Mauch, G. Schön, and M. Marthaler, *Effects of gate errors in digital quantum simulations of fermionic systems*, Quantum Sci. Technol. **3**, 045008 (2018).

Reprinting of copyrighted material from this publication is explicitly permitted within this thesis by IOP Publishing Ltd.

In comparison to analog quantum simulations as discussed in the previous chapter, the approach of digital quantum simulation is in principle much more versatile. Another benefit of digital quantum simulation is that, eventually, quantum error correction offers a route to resolve the issue of decoherence [39], and qubits with fidelities at the threshold for the implementation of quantum error correction have been demonstrated [34, 35, 38, 98]. Nevertheless at present the number of qubits required for full quantum error correction appears prohibitive [37, 40].

In a situation where only small-size and imperfect quantum simulators are within reach, it is crucial to gain a better understanding of the effect of errors on their performance. For some examples, methods to estimate the quality of quantum simulators with errors have been suggested [5, 99], and proposals for error reduction exist [6, 100]. However, all in all it remains largely unexplored how errors will affect the results of quantum simulations, and even whether the results obtained in this way have a physical meaning [56].

In this chapter, we evaluate the effect of gate errors on digital quantum simulations. Digital simulations are highly esteemed due to their wide range of applicability [101–103], e.g., for quantum chemistry or many-body physics. Specifically, we study simulations of fermionic systems, such as the Hubbard model, which are considered to be prime targets of quantum simulations [104, 105]. In a digital quantum simulation the time evolution

operator of the system is evaluated by splitting the Hamiltonian into parts acting in smaller subspaces via the Trotter expansion and, instead of a continuous time evolution, the simulator implements a succession of short-time Trotter steps (see Sec. 2.3.2). This short-time evolution in the appropriate subspace is then simulated by an algorithm based on a sequence of quantum gates which are available on the hardware level. The quality of the Trotter expansion requires short time steps, and for a many-particle system the Hamiltonian consists of many terms. Hence, a very large number of gates are needed [106]. It cannot be avoided that the gates are subject to some errors. Even if they are small for each individual gate, due to their large number a substantial error will accumulate, and the gain from implementing finer time steps will be limited [70].

In addition, we address here the question whether gate errors in a digital quantum simulation have a *physical meaning*. Generally, the exact form of gate errors is not well known. Standard gates perform a rotation of the many-qubit state. We, therefore, model the gate errors as over-rotations (or under-rotations). For such gate errors we show that the simulation, rather than modeling the time evolution under the original Hamiltonian H , models the time evolution under an *effective Hamiltonian* $H + \delta H$. The added term δH is proportional to the strength of the over-rotations; its specific details depend on the chosen algorithm. We show that for some algorithms it can be interpreted as a disorder term. With this knowledge one can interpret the results of the simulation, such as, e.g., the spectral resolution. However, other algorithms may introduce contributions δH such that the physical properties of the effective Hamiltonian are very different from the original ones.

The magnitude of the over-rotation can be related to the gate fidelity, a widely used measure for the quality of a quantum gate. Specifically, as shown in Sec. 4.4.1, an over-rotation by an angle $\delta\varphi$ reduces the minimal gate fidelity \mathcal{F}_{\min} (i.e., the fidelity minimized with respect to all possible input states) to the value $\mathcal{F}_{\min} = \cos(\delta\varphi)$.¹ Reversing this relation, $|\delta\varphi| \approx \sqrt{2(1 - \mathcal{F}_{\min})}$, shows that the fidelity has to be very close to 100% to keep the gate errors small. Typically the over-rotation angles are stochastic variables. Assuming that in independent runs of the experiment the over-rotations vanish on average with a given variance $\text{Var}(\delta\varphi)$, we find for the average minimal fidelity $\overline{\mathcal{F}}_{\min} = 1 - \text{Var}(\delta\varphi)^2/2$. The fidelity can be determined experimentally by examining each gate individually before the simulation.

The extra contribution to the Hamiltonian introduced by the over-rotations scales as $|\delta H| \propto n \text{Var}(\delta\varphi)$, i.e., it increases proportional to the number of Trotter steps n . Note, that this property is a consequence of the fact that we chose the over-rotation variance $\text{Var}(\delta\varphi)$ to be independent of the duration of the Trotter time steps $\propto 1/n$, and errors do not get weaker if we choose shorter time steps (in actual simulations the opposite may be relevant, namely that the errors increase with increasing length of the Trotter steps. Our model then covers the limit of short steps). In addition, with increasing system size one has to perform an increasing number of gates per Trotter step. In the

¹Here we follow the notation of Nielsen and Chuang [63], often the square of \mathcal{F}_{\min} is called fidelity. See Sec. 4.4.1 for a precise definition.

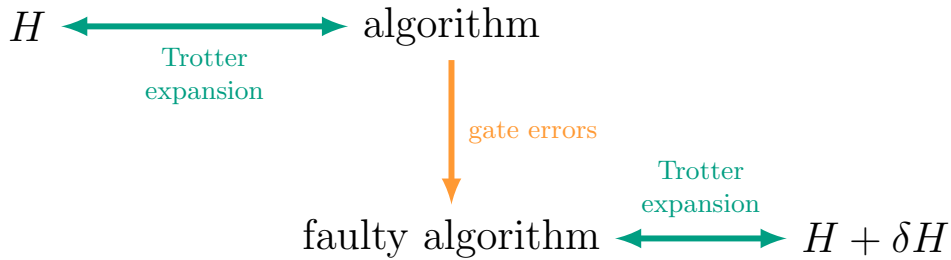


Figure 4.1: The time evolution of a (fermionic) quantum system with Hamiltonian H is simulated through digital quantum simulation based on the Trotter expansion. Gate errors in the algorithm arise due to over-rotations with strength related to the fidelity of the gates. The resulting *faulty* algorithm simulates – within the Trotter approximation – a system with Hamiltonian $H + \delta H$. The structure of δH is sensitive to the specific algorithm and often describes disorder.

simulations a balance has to be found between the quality of the Trotter expansion and the errors introduced by the gates. Labeling the number of gates per Trotter step by N_g (as we discuss below this is roughly the number of two-qubit gates per Trotter step), we arrive at the following limitation:

$$nN_g < \frac{1}{\sqrt{2(1 - \bar{\mathcal{F}}_{\min})}}. \quad (4.1)$$

Note, that this is a worst-case estimate. Depending on how errors of various gates add up, the number N_g could effectively be much smaller. This is discussed in more detail in Sec. 4.4.

The present chapter is organized as follows: In the following section we will state our model assumptions and show how gate errors in a digital quantum simulation effectively lead to a time evolution under a modified Hamiltonian. Fig. 4.1 gives a structural overview of our approach and findings. Thereafter we illustrate the method and results by considering a model system. We show that different choices of the algorithms lead to different effective Hamiltonians. We substantiate our findings by a numerical analysis of a minimal model system with varying error strengths which we compare to present-day experimentally achieved gate fidelities. We also study the trade-off between a finer Trotterization, i.e., less Trotter expansion error, and the resulting necessity to run more faulty gates. We add some comments on the effect of errors in the adiabatic state preparation. We conclude with a summary and outlook.

4.1 Error model and method

4.1.1 Method and assumptions

We consider in the following algorithms simulating the time evolution under a Hamiltonian H , or in general $H(t)$, making use of the Trotter expansion. The Trotter approx-

imation was introduced in detail in Sec. 2.3.2, but we will review it here again briefly. It assumes that the time evolution operator during time $0 \leq t \leq \tau$ is broken into a product of a large number of n short segments of length $\frac{\tau}{n}$ (which is a way to assure the proper time order in the time-evolution operator). It further exploits the fact that the usually complicated many-body Hamiltonian H can be decomposed into N parts, $H = \sum_{\alpha=1}^N H_{\alpha}$, each acting in a much reduced Hilbert space. If the Hamiltonian does not depend on time (the generalization is obvious) we have

$$\begin{aligned} e^{-iH\tau} &= \left(\prod_{\alpha=1}^N e^{-iH_{\alpha} \frac{\tau}{n}} + \mathcal{O}\left(\left(\frac{g\tau}{n}\right)^2\right) \right)^n \\ &= \left(\prod_{\alpha=1}^N e^{-iH_{\alpha} \frac{\tau}{n}} \right)^n + \mathcal{O}\left(\frac{(g\tau)^2}{n}\right), \end{aligned} \quad (4.2)$$

where we denote $g = \max_{\alpha} \|H_{\alpha}\|$, the largest energy scale of the Hamiltonian. If the number of Trotter steps is chosen sufficiently large, such that $\frac{g\tau}{n} \ll 1$, the first order Trotter expansion is sufficient. If, furthermore, each H_{α} can be implemented and controlled by the hardware of the quantum simulator, the decomposition (4.2) describes a sequence of gates which simulates the time evolution.

In order to make quantitative predictions on the effect of gate errors on the digital quantum simulation we have to specify their nature. Our primary assumptions and approximations are the following:

- (i) The only type of errors in gates are over-rotations.
- (ii) The strength (i.e., variance) of the gate errors is such that higher order contributions in the Trotter expansion can be neglected.

Additionally we assume – although this could be easily generalized:

- (iii) Errors in single-qubit gates can be neglected as compared to those occurring in gates between two or more qubits.
- (iv) The over-rotations in each individual gate are independent and may vary with time.

By assumption (i) we imply that the needed gates are performed with the correct interaction between qubits, but there is, e.g., an uncertainty in the interaction time [107]. Since a gate (expressed as an exponential of Pauli operators or products thereof) can be seen as a rotation of the state of the qubit register, an error causes an over-rotation (or under-rotation). We also imply that the needed interaction is either realized *intrinsically* as a physical interaction on the hardware-level, or that the gate (e.g., an off-axis rotation) can be decomposed into several intrinsic gates. (In such cases the over-rotations in individual gates, in general, cannot be combined to an over-rotation in the composite one.) More explicitly, we write the gate as an exponential $e^{i\varphi A}$, with an dimensionless operator A with unit norm, $\|A\| = 1$ where $\|\cdot\|$ denotes the standard induced operator

norm,² characterizing the type of interaction of the gate, and an angle φ . An over-rotation is characterized by an addition $\delta\varphi$ to the angle, such that the faulty gate is $e^{i(\varphi+\delta\varphi)A}$.

Assumption (ii) implies bounds for $\delta\varphi$. Rewriting the exponents in Eq. (4.2) as $-iH_\alpha \frac{\tau}{n} = -i\frac{g\tau}{n} \frac{H_\alpha}{g}$ and noting that $\frac{H_\alpha}{g}$ has unit norm or less, shows that – in analogy to what we discussed under assumption (i) – the Trotterization introduces angles of order $\frac{g\tau}{n}$. The over-rotation $\delta\varphi$ should be of smaller magnitude

$$|\delta\varphi| \leq \frac{g\tau}{n}. \quad (4.3)$$

In this case, order $\mathcal{O}(\delta\varphi^2)$ terms and products between $\delta\varphi$ and $\frac{g\tau}{n}$ can be neglected inside a Trotter step, consistent with the Trotter approximation.

The optional assumption (iii) is motivated by the observation that single-qubit gates usually have a significantly better fidelity than two-qubit gates [34, 108–111]. In addition, there are examples, e.g., the Hubbard model with equal on-site energies, which can be simulated using only two-qubit gates. Single-qubit gates are needed if only a limited set of two-qubit gates is available (see the example of a gate decomposition in Sec. 2.3.1). For instance, the hardware may allow only for XX interaction between nearest-neighbor qubits. Examples are capacitively coupled transmon qubits [1, 50], or trapped-ion architectures [112]. In these cases implementing a ZZ interaction requires additional single-qubit rotations. All conclusion drawn in the following do not change if a simulated interaction involves such additional (ideally error-free) single-qubit gates.

As expressed by assumption (iv) we allow the gate errors to vary with time. In the numerical simulation performed below we assume that the errors are normal-distributed with zero mean. Particularly, we will investigate the effect of errors after averaging over many different runs of an algorithm, each one performed with a different realization of the random errors. However, at no point in our discussion this is strictly necessary. A constant error leads to a constant perturbative correction to the Hamiltonian, which can be estimated, and on top of it, it should be possible to reduce its effect more efficiently.

4.1.2 Effects of gate errors

With the assumptions specified, we are now ready to analyze the effects of gate errors due to over-rotations. There are two distinct cases:

Case 1: Consider a Hamiltonian $H = H_1 + H_2$, where $H_\alpha = g_\alpha A_\alpha$ with $\|A_\alpha\| = 1$. For simplicity of the notation in the following we assume $g_1 = g_2 = g$. Also the generalization to a situation with more terms is straightforward. In this first, simple case, we further assume that the quantum simulator allows performing directly – with the available hardware by single gates – the Trotter steps arising from the interactions

²The normalization does not fix the angle of rotation but imposes an upper bound to it. Consider Pauli operators $\sigma^+\sigma^-$ and σ^z : Even though $\|\sigma^+\sigma^-\| = \|\sigma^z\| = 1$, the first operator rotates half as much as the second, since $\sigma^+\sigma^- = \frac{\sigma^z}{2} + \frac{1}{2}$. Below we ignore such constant factors (and global phases). A more thorough definition of A is given in Sec. 4.4.1.

A_α . In this case, the simulation of the time evolution under H is based on the Trotter expansion,

$$e^{-iH\tau} = \left(e^{-i\frac{g\tau}{n}A_1} e^{-i\frac{g\tau}{n}A_2} + \mathcal{O}\left(\left(\frac{g\tau}{n}\right)^2\right) \right)^n. \quad (4.4)$$

Gate errors due to independent over-rotations $\delta\varphi_{(1,2)m}$ during the m^{th} Trotter step lead to the modification

$$\begin{aligned} & e^{-i\frac{g\tau}{n}A_1} e^{-i\frac{g\tau}{n}A_2} \\ \mapsto & e^{-i(\frac{g\tau}{n} + \delta\varphi_{1m})A_1} e^{-i(\frac{g\tau}{n} + \delta\varphi_{2m})A_2} \\ = & e^{-i\frac{g\tau}{n}A_1} e^{-i\frac{g\tau}{n}A_2} e^{-i\delta\varphi_{1m}A_1} e^{-i\delta\varphi_{2m}A_2} + \mathcal{O}\left(\left(\frac{g\tau}{n}\right)^2\right). \end{aligned} \quad (4.5)$$

In the last step we made use of Eq. (4.3). Comparing to the time-dependent generalization of Eq. (4.2), we find that the over-rotations lead to the simulation of the time evolution under an effective Hamiltonian $H + \delta H(t)$, where

$$\delta H(t) = \frac{n}{\tau} \delta\varphi_1(t) A_1 + \frac{n}{\tau} \delta\varphi_2(t) A_2. \quad (4.6)$$

with the fluctuating fields $\delta\varphi_j(t) = \delta\varphi_{jm}$ for $t \in [\frac{\tau}{n}(m-1), \frac{\tau}{n}m)$. We note that in the simple case 1 the structure of the effective Hamiltonian is the same as the original one, except that the interactions strengths fluctuate in time. We also note that the contributions from the errors scale linearly with n , i.e., they become larger when the Trotterization is based on more, finer steps. Thus, as noted in Ref. [70], the gain from a finer Trotterization is limited. On the other hand, we note that the corrections are still small compared to the largest energy scale of the original Hamiltonian, $\frac{n}{\tau} |\delta\varphi_j(t)| \leq g$.

Case 2: The situation is more complex if an interaction, e.g., A_1 , cannot be implemented directly by gates available on the hardware-level of the quantum simulator, and a decomposition involving additional two-qubit gates is required. They are also subject to errors due to over-rotations. An example could be a chain of qubits with only nearest-neighbor XX -couplings. To simulate a Hamiltonian with XX interactions between next-nearest neighbors one needs to introduce, e.g., **SWAP** gates before and after the available nearest-neighbor XX interaction. Other examples for this scenario are simulations of d -dimensional systems by a simulator with a $d-1$ -dimensional geometry. Still another example, which we will encounter below, are long-range terms arising due to the Jordan-Wigner transformation.

Let us assume that a Trotter step with interaction A_1 is decomposed as

$$e^{-i\frac{g\tau}{n}A_1} = e^{i\varphi C} e^{-i\frac{g\tau}{n}B_1} e^{i\varphi' C'}, \quad (4.7)$$

where B_1 and $C^{(\prime)}$ can be implemented on the hardware level. Sometimes, this describes a unitary transformation where $e^{i\varphi C}$ and $e^{i\varphi' C'}$ are inverse operators. This case is

relatively simple, and we return to it below. For the moment we consider the general case where the two transformations are independent of each other. Again we choose $\|B_1\| = \|C^{(\prime)}\| = 1$. Note, that the angles $\varphi^{(\prime)}$ are typically of order $\mathcal{O}(1)$, i.e., much larger than $\frac{g\tau}{n}$. It is more difficult to treat gate errors now, since commutators between exponentials with exponents of order $\mathcal{O}(\delta\varphi)$ of the gate errors and exponential with exponents of order $\mathcal{O}(1)$ have to be taken into account.

To calculate these commutators, we use the relation

$$e^X e^Y e^{-X} = e^{e^X Y e^{-X}} = e^{\text{Ad}_{e^X}(Y)}, \quad (4.8)$$

where for later convenience we introduced the notation $\text{Ad}_{e^X}(Y) = e^X Y e^{-X}$ for the adjoint representation. It follows that

$$\begin{aligned} e^X e^Y &= e^{\text{Ad}_{e^X}(Y)} e^X, \\ e^Y e^X &= e^X e^{\text{Ad}_{e^{-X}}(Y)}. \end{aligned} \quad (4.9)$$

Errors due to over-rotations, $\delta\varphi, \delta\varphi_1, \delta\varphi'$, in the gate (4.7) will enter in each of the three exponents. To evaluate their effects we use the above relations to commute the errors out of the original gate decomposition and arrive at

$$\begin{aligned} & e^{i\varphi C} e^{-i\frac{g\tau}{n} B_1} e^{i\varphi' C'} \\ \mapsto & e^{i(\varphi+\delta\varphi)C} e^{-i(\frac{g\tau}{n}+\delta\varphi_1)B_1} e^{i(\varphi'+\delta\varphi')C'} \\ = & e^{i\delta\varphi C} e^{i\varphi C} e^{-i\delta\varphi_1 B_1} e^{-i\frac{g\tau}{n} B_1} e^{i\varphi' C'} e^{i\delta\varphi' C'} \\ = & e^{i\delta\varphi C} e^{\text{Ad}_{e^{i\varphi C}}(-i\delta\varphi_1 B_1)} \underbrace{e^{i\varphi C} e^{-i\frac{g\tau}{n} B_1} e^{i\varphi' C'}}_{= e^{-i\frac{g\tau}{n} A_1}} e^{i\delta\varphi' C'} \\ = & e^{-i\frac{g\tau}{n} A_1} e^{i\delta\varphi C} e^{i\delta\varphi' C'} e^{-i\delta\varphi_1 \text{Ad}_{e^{i\varphi C}}(B_1)} + \mathcal{O}\left(\left(\frac{g\tau}{n}\right)^2\right). \end{aligned} \quad (4.10)$$

All the exponents are now of order $\mathcal{O}(\frac{g\tau}{n})$ such that commuting the exponentials contributes negligible errors of order $\mathcal{O}((\frac{g\tau}{n})^2)$. Hence, we can proceed with the Trotter expansion (4.2) and find the effective time-dependent Hamiltonian $H + \delta H(t)$ that is simulated with

$$\delta H(t) = -\frac{n}{\tau} \delta\varphi(t) C - \frac{n}{\tau} \delta\varphi'(t) C' + \frac{n}{\tau} \delta\varphi_1(t) \text{Ad}_{e^{i\varphi C}}(B_1). \quad (4.11)$$

The presented scheme can be applied iteratively for higher stage gate decompositions. Therefore, it is a scalable approach where algorithms can be analyzed piecewise.

The non-trivial addition $\text{Ad}_{e^{i\varphi C}}(B_1) = e^{i\varphi C} B_1 e^{-i\varphi C}$ as compared to Case 1 can be evaluated by using Hadamard's lemma (related to the Baker-Campbell-Hausdorff formula):

$$e^X Y e^{-X} = Y + [X, Y] + \frac{1}{2}[X, [X, Y]] + \frac{1}{3!}[X, [X, [X, Y]]] + \dots \quad (4.12)$$

However, since in the Trotter expansion we commute quantum gates, the exponentials often have simple representations in terms of Pauli matrices. Hence, the product $e^{i\varphi C} B_1 e^{-i\varphi C}$ can be calculated by expressing $e^{\pm i\varphi C}$ and B_1 in terms of Pauli matrices. This is evident for B_1 , since it describes an interaction between qubits, but also for $e^{i\varphi C}$, which might be a quantum gate like CNOT, (i)SWAP, CZ, and so forth.

In the cases where the unitary transformation $e^{i\varphi C}$ and $e^{i\varphi' C'}$ in eq. (4.7) are inverse operators we simply have $\text{Ad}_{e^{i\varphi C}}(B_1) = e^{i\varphi C} B_1 e^{-i\varphi C} = A_1$, and the disorder term in eq. (4.11) simplifies accordingly.

We have now established our method to treat gate errors in a digital quantum simulation. In order to render the description less abstract we will apply it in the next section to an example algorithm. We will explicitly show the structure of δH that is generated by the different parts of the algorithm.

4.2 Example system: Fermi-Hubbard model

4.2.1 Fermi-Hubbard model with spin-flip interaction

We will investigate now in detail the Fermi-Hubbard model including spin-flip interaction for a small system consisting only of two degenerate sites. This minimal model already allows us to illustrate several of the important issues. The Hamiltonian is

$$H = U \sum_{j=1}^2 c_{j\uparrow}^\dagger c_{j\uparrow} c_{j\downarrow}^\dagger c_{j\downarrow} - t_1 \sum_{s=\uparrow,\downarrow} (c_{1s}^\dagger c_{2s} + c_{2s}^\dagger c_{1s}) - t_2 \sum_{j=1}^2 (c_{j\uparrow}^\dagger c_{j\downarrow} + c_{j\downarrow}^\dagger c_{j\uparrow}), \quad (4.13)$$

where $c_{j,s}^{(\dagger)}$ stands for the fermionic annihilation (creation) operator of site j with spin s . The on-site interaction energy is U , the hopping amplitude between the sites is t_1 , and spin-flips on each site occur with amplitude t_2 . To perform the simulation we map the fermionic system on a system of spins/qubits via the Jordan-Wigner transformation. Because of the spin-flip interaction in addition to the hopping this mapping is non-trivial even for the small (one-dimensional) system considered, i.e., non-local terms as discussed in Sec. 2.1.1 will occur in the qubit system.

We first relabel the fermionic operators,

$$c_1 = c_{1\uparrow}, \quad c_2 = c_{2\uparrow}, \quad c_3 = c_{2\downarrow}, \quad c_4 = c_{1\downarrow}, \quad (4.14)$$

such that we can map them on Pauli matrices $\sigma^{x,y,z}$ and the ladder operators $\sigma^\pm = \frac{1}{2}(\sigma^x \pm i\sigma^y)$ via the Jordan-Wigner transformation

$$c_j = \prod_{k=1}^{j-1} (-\sigma_k^z) \sigma_j^-, \quad (4.15)$$

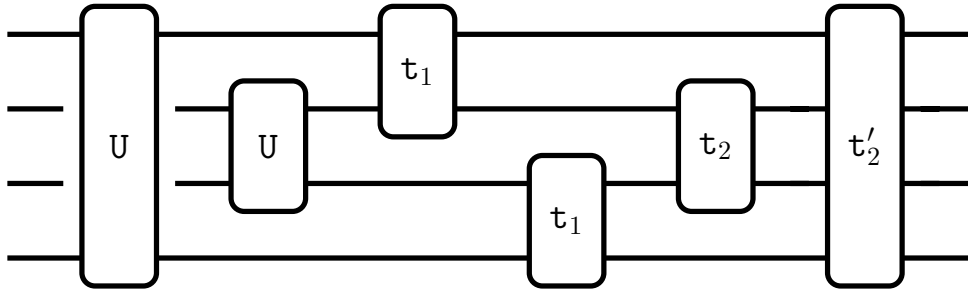


Figure 4.2: One Trotter step of an algorithm simulating the time evolution under the Hamiltonian (4.16). The horizontal lines represent the qubits and the boxes the gates of the algorithm. A qubit line connected to a gate is an in-/output of that gate. If a line is interrupted at a gate the corresponding qubit is not influenced by that gate. The two-qubit U gates implement the on-site interaction, the t_1 gates the hopping terms, the t_2 gate a part of the spin-flip interactions. The four-qubit gate t'_2 accounts for the non-local term which arises due to the Jordan-Wigner transformation.

as introduced in Sec.2.1.1. The Hamiltonian thus becomes

$$\begin{aligned}
 H = & U(\sigma_1^+ \sigma_1^- \sigma_4^+ \sigma_4^- + \sigma_2^+ \sigma_2^- \sigma_3^+ \sigma_3^-) \\
 & - t_1((\sigma_1^+ \sigma_2^- + \sigma_1^- \sigma_2^+) + (\sigma_3^+ \sigma_4^- + \sigma_3^- \sigma_4^+)) \\
 & - t_2((\sigma_2^+ \sigma_3^- + \sigma_2^- \sigma_3^+) + (\sigma_1^+ \sigma_2^z \sigma_3^z \sigma_4^- + \sigma_1^- \sigma_2^z \sigma_3^z \sigma_4^+)). \quad (4.16)
 \end{aligned}$$

We mentioned already in Sec. 2.1.1, that there exist alternative mappings between fermions and spins, e.g., the Bravyi-Kitaev transformation. In detail the effects of gate errors will depend on the transformation used and – as we show below – on aspects of the specific algorithm used. Here we have chosen the Jordan-Wigner transformation as it leads to an intuitive interpretation of the results. In addition it is known that algorithms based on the Jordan-Wigner mapping are very efficient for Hubbard-type models [113]. Note that, similar to Chap. 3, because $\sigma_j^+ \sigma_j^- = \frac{1}{2}(\sigma_j^z + 1)$, the on-site terms are effectively a ZZ interaction, and within the rotating wave approximation the terms $\sigma_j^+ \sigma_k^- + \sigma_k^+ \sigma_j^-$ are equivalent to an XX interaction.

We consider the situation where the hardware allows for XX and ZZ interactions between each pair of qubits (note that the two are related to each other via single-qubit gates, which we assume to be error free). In this case every term in H can be realized by a two-qubit gate, except for the non-local terms $-t_2 \sigma_1^\pm \sigma_2^z \sigma_3^z \sigma_4^\mp$. They contain a residual Jordan-Wigner string and arise in the considered model as a consequence of the Jordan-Wigner transformation. The terms are labeled in the following as t'_2 gate. They need to be decomposed into multiple two-qubit gates.

4.2.2 Algorithm and effects of gate errors

We implement the time evolution of the Hamiltonian (4.16) by a Trotter expansion, where the gates needed for one Trotter step are depicted in Fig. 4.2. It involves two-qubit gates labeled U , which account for the on-site interaction, two-qubit gates labeled

\mathfrak{t}_1 for the hopping terms, and a two-qubit gate \mathfrak{t}_2 which implements the first part of the spin-flip interaction. The non-local terms of the spin-flip interaction introduced by the Jordan-Wigner string are represented by a four-qubit gate \mathfrak{t}'_2 . We now will use the method laid out in Sec. 4.1.2 to analyze the effects of gate errors in the various parts of this algorithm and also propose an explicit decomposition of the four-qubit gate.

U gates. The first U gate in Fig. 4.2 has the representation

$$\mathbf{U}_{1,4} = e^{-iU \frac{\pi}{n} \sigma_1^+ \sigma_1^- \sigma_4^+ \sigma_4^-}, \quad (4.17)$$

where the indices indicate that the interaction occurs between qubit one and four. The effect of over-rotations is covered by Case 1 of Sec. 4.1.2, leading to

$$\mathbf{U}_{1,4} \mapsto e^{-i(U \frac{\pi}{n} + \delta\varphi_{1,4}^U) \sigma_1^+ \sigma_1^- \sigma_4^+ \sigma_4^-},$$

i.e., the Hamiltonian that will actually be simulated in the presence of over-rotation is

$$\begin{aligned} H &\mapsto H + \frac{n}{\tau} \delta\varphi_{1,4}^U(t) \sigma_1^+ \sigma_1^- \sigma_4^+ \sigma_4^- \\ &= H + \frac{n}{\tau} \delta\varphi_{1,4}^U(t) c_1^\dagger c_1 c_4^\dagger c_4, \end{aligned} \quad (4.18)$$

and likewise for the second gate $\mathbf{U}_{2,3}$. Hence, $\delta H(t)$ has the same structure as the original Hamiltonian but with a fluctuating strength of the on-site interactions.

\mathfrak{t}_1 and \mathfrak{t}_2 gates. The \mathfrak{t}_1 and \mathfrak{t}_2 gates of the algorithm in Fig. 4.2 apply similar exchange interactions. We label them by $\mathfrak{t}_{1,2}$, $\mathfrak{t}_{3,4}$, and $\mathfrak{t}_{2,3}$, where the first two have amplitude t_1 while the third has amplitude t_2 . For instance we have

$$\mathfrak{t}_{1,2} = e^{it_1 \frac{\pi}{n} (\sigma_1^+ \sigma_2^- + \sigma_1^- \sigma_2^+)}. \quad (4.19)$$

Again, errors in these gates are described by Case 1 of Sec. 4.1.2, i.e., they lead to contributions of the form

$$\begin{aligned} H &\mapsto H - \frac{n}{\tau} \delta\varphi_{1,2}^{t_1}(t) (\sigma_1^+ \sigma_2^- + \sigma_1^- \sigma_2^+) \\ &= H - \frac{n}{\tau} \delta\varphi_{1,2}^{t_1}(t) (c_1^\dagger c_2 + c_2^\dagger c_1), \end{aligned} \quad (4.20)$$

and likewise for the hopping gate $\mathfrak{t}_{3,4}$ and the spin-flip gate $\mathfrak{t}_{2,3}$. Again $\delta H(t)$ has the same structure as the original Hamiltonian but with a fluctuating strength of the hopping and spin-flip terms.

\mathfrak{t}'_2 gate. We assume that the hardware allows performing two-qubit ZZ and XX gates. But because of the Jordan-Wigner strings the \mathfrak{t}'_2 gate involves four different spins, an interaction which is usually not contained on the hardware level. Accordingly, this gate has to be decomposed into further gates, i.e., it falls into the scope of Case 2 of Sec. 4.1.2.

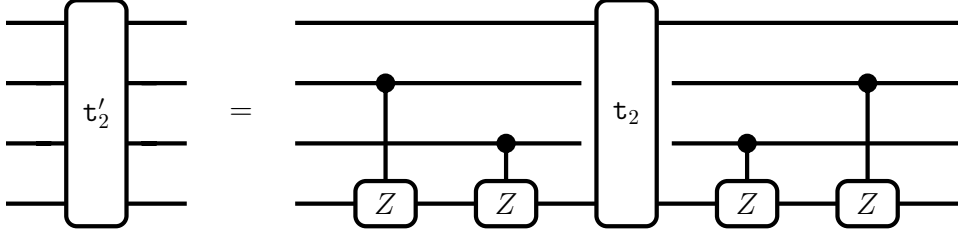


Figure 4.3: The four-qubit gate \mathfrak{t}'_2 can be decomposed into a two-qubit \mathfrak{t}_2 gate and additional CZs accounting for the Jordan-Wigner string.

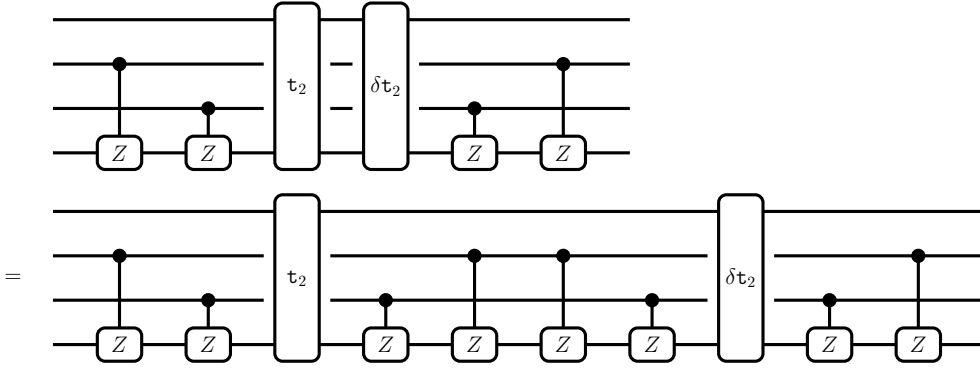


Figure 4.4: The gate \mathfrak{t}_2 gate and the error $\delta\mathfrak{t}_2$ are analyzed by writing the identity as a string of virtual CZ gates.

One possible decomposition is shown in Fig. 4.3. A central \mathfrak{t}_2 gate is performed involving qubits one and four, while the Jordan-Wigner string $\sigma_2^z \sigma_3^z$ is implemented by strings of controlled Z (CZ) gates. This can be understood as follows: The Jordan-Wigner strings introduce a sign change to the $\sigma_1^+ \sigma_4^- + \sigma_4^+ \sigma_1^-$ interaction for every qubit between one and four that is excited (see Eq. (4.15), this encodes the fermionic parity). The action of σ^z on qubit four via the CZs with control on qubits two and three does exactly that; for every excited qubit we get a product $\sigma_4^z \sigma_4^\pm \sigma_4^z = -\sigma_4^\pm$, hence, a minus sign in the interaction term.

A CZ gate between the control qubit j and the target qubit k has the form $\text{CZ}_{j,k} = e^{i\pi\sigma_j^+ \sigma_j^- \sigma_k^- \sigma_k^+}$. The CZ gates are diagonal and commute among each other. I.e., exponentials arising due to over-rotations are trivially shifted to the left and right of the original gate composition. Hence, errors in the CZ gates contribute to the simulated Hamiltonian terms of the form

$$\begin{aligned} H &\mapsto H - \frac{n}{\tau} \delta\varphi_{j,k}^{\text{CZ}}(t) \sigma_j^+ \sigma_j^- \sigma_k^- \sigma_k^+ \\ &= H - \frac{n}{\tau} \delta\varphi_{j,k}^{\text{CZ}}(t) c_j^\dagger c_j c_k c_k^\dagger, \end{aligned} \quad (4.21)$$

i.e., they introduce additional interaction terms beyond the original on-site interaction.

Errors in the \mathfrak{t}_2 interaction do not commute with the surrounding CZ gates, however.

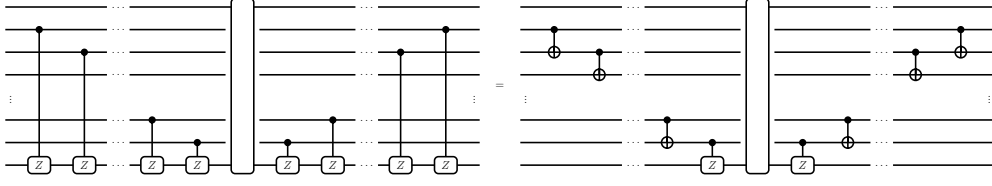


Figure 4.5: Instead of using CZ chains between far separated qubits for implementing the Jordan-Wigner string, one can use chains of CNOTs between nearest neighbors.

They require a more complicated analysis based on Eq. (4.10) with an evaluation of the adjoint. Here, instead of two embracing gates $e^{i\varphi^{(\prime)}C^{(\prime)}}$ we have four, namely the CZ gates in Fig. 4.3. Therefore, Eq. (4.10) would have to be applied twice. On the other hand, in the present case there exists an easier approach to this iterative process: We label the gate errors $\delta\mathbf{t}_2$ and use the fact that $(\text{CZ}_{j,k})^2 = \mathbb{1}$ to introduce additional (virtual) gates, depicted in Fig. 4.4. The figure illustrates that for the \mathbf{t}_2 as well as for the $\delta\mathbf{t}_2$ gate (compare to Fig. 4.3) the implementation of the Jordan-Wigner strings is the same. Accordingly, both are transformed in the same way by the inverse Jordan-Wigner transformation. Hence, the Hamiltonian effectively simulated is

$$\begin{aligned} H &\mapsto H - \frac{n}{\tau} \delta\varphi_{1,4}^{t_2}(t) (\sigma_1^+ \sigma_2^z \sigma_3^z \sigma_4^- + \sigma_1^- \sigma_2^z \sigma_3^z \sigma_4^+) \\ &= H - \frac{n}{\tau} \delta\varphi_{1,4}^{t_2}(t) (c_1^\dagger c_4 + c_4^\dagger c_1). \end{aligned} \quad (4.22)$$

Adding up the various contributions discussed in this subsection, we find that due to the effect of over-rotations we effectively simulate a *disordered* Hamiltonian with fluctuating hopping and spin-flip terms and strength of the on-site interaction, and in addition fluctuating interactions between different sites.

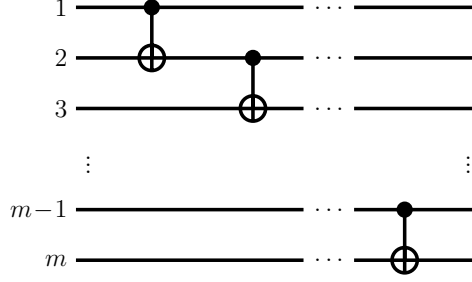
4.2.3 Scaling up to larger systems

In this subsection, we comment on the issue that emerges when scaling up the model system to more sites. A potential drawback of the implementation of Jordan-Wigner strings by CZ gates (see Fig. 4.3) are interactions between qubits that are far apart in the circuit. In devices where, e.g., qubits are arranged in chains with nearest-neighbor interaction only, this may become tedious.

Jordan-Wigner strings using CNOTs. One possible solution is to employ instead of CZs the gates CNOT, as depicted in Fig. 4.5. A CNOT with control and target qubit j and k has the form

$$\text{CNOT}_{j,k} = \sigma_j^+ \sigma_j^- \sigma_k^x + \sigma_j^- \sigma_j^+ = e^{i\frac{\pi}{2} \sigma_j^+ \sigma_j^- (1 - \sigma_k^x)}. \quad (4.23)$$

When using CNOT gates we encounter the following problems:


 Figure 4.6: A chain of CNOT gates in an array of m qubits, as it appears in Fig. 4.5.

(1) In a circuit with ZZ and XX interaction the CNOT requires an XZ -type mixture of these interactions. This can be achieved by adding extra single-qubit gates, which are assumed to have a negligible error (see the example in Sec. 2.3.1).

(2) Unlike CZ gates, the CNOT gates do not commute among each other. Consider a chain of CNOTs in an array of m qubits as depicted in Fig. 4.6. We allow for an over-rotation $\delta\varphi$ in the rightmost gate, which we would like to commute to the far left. This requires an analysis as discussed in Case 2 of Sec. 4.1.2. We commute the error gate by gate using Eq. (4.9). The first step yields the exponent

$$\begin{aligned} & \text{Ad}_{\text{CNOT}_{m-2,m-1}}(i\delta\varphi\sigma_{m-1}^+\sigma_{m-1}^-(1-\sigma_m^x)) \\ &= i\delta\varphi(1-\sigma_m^x)\text{Ad}_{\text{CNOT}_{m-2,m-1}}(\sigma_{m-1}^+\sigma_{m-1}^-) \\ &= i\delta\varphi(1-\sigma_m^x)(\sigma_{m-1}^+\sigma_{m-1}^- - \sigma_{m-2}^+\sigma_{m-2}^-)^2. \end{aligned} \quad (4.24)$$

Here, we calculated the adjoint $\text{Ad}_A(B) = ABA^{-1}$ by writing the CNOT gate in terms of Pauli operators (see Eq. (4.23), left representation), and evaluating the products of Pauli matrices. Commuting the result one gate further gives a term

$$\begin{aligned} & \text{Ad}_{\text{CNOT}_{m-3,m-2}}((\sigma_{m-1}^+\sigma_{m-1}^- - \sigma_{m-2}^+\sigma_{m-2}^-)^2) \\ &= (\sigma_{m-1}^+\sigma_{m-1}^- - \text{Ad}_{\text{CNOT}_{m-3,m-2}}(\sigma_{m-2}^+\sigma_{m-2}^-))^2 \\ &= (\sigma_{m-1}^+\sigma_{m-1}^- - (\sigma_{m-2}^+\sigma_{m-2}^- - \sigma_{m-3}^+\sigma_{m-3}^-))^2. \end{aligned} \quad (4.25)$$

We can iteratively continue this process until we commuted the error to the far left. On the Hamiltonian level this procedure leads to the extra contribution

$$\delta H(t) = \frac{n}{\tau}\delta\varphi(t)(1-\sigma_m^x)\Sigma_{m-1}^\pm, \quad (4.26)$$

with the nested operator Σ_{m-1}^\pm defined via $\Sigma_1^\pm = \sigma_1^+\sigma_1^-$ and $\Sigma_k^\pm = (\sigma_k^+\sigma_k^- - \Sigma_{k-1}^\pm)^2$ (for integers $k \geq 2$). Thus, we succeeded analyzing errors due to over-rotations in Jordan-Wigner strings by using CNOT gates and writing down the spin Hamiltonian that is simulated in the presence of gate errors. However, we still are left with a 3rd problem, namely:

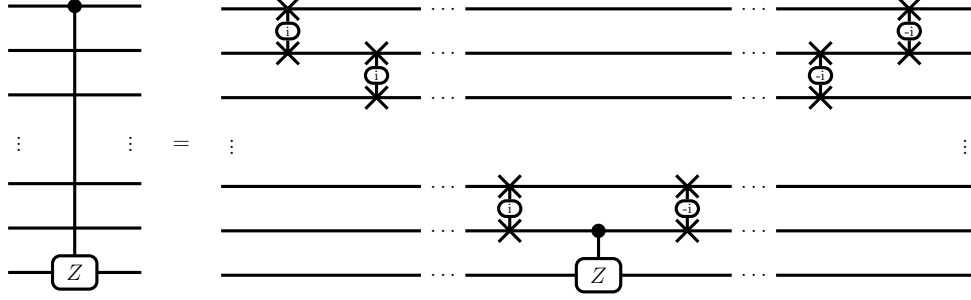


Figure 4.7: If the interaction of a CZ cannot be applied directly between two qubits that are far apart on the hardware, one can use chains of \pm iSWAPs to circumvent the problem.

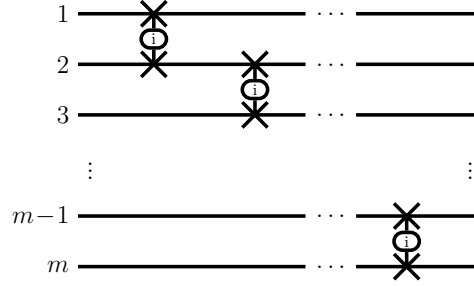


Figure 4.8: A chain of iSWAP gates in an array of m qubits, as it appears in Fig. 4.7.

(3) To interpret the result we should transform back into a fermionic representation. We apply the inverse Jordan-Wigner transformation $\sigma_m^+ = \prod_{k=1}^{m-1} (2c_k^\dagger c_k - 1)c_m$ to Eq. (4.26) using $\sigma_m^x = \sigma_m^+ + \sigma_m^-$ and $\sigma_j^+ \sigma_j^- = c_j^\dagger c_j$. This leads to a product of many fermionic operators in the effective Hamiltonian, i.e., it introduces effective many-particle interactions involving many sites. On top of it, we find terms containing an *odd* number of fermionic operators and therefore – unlike the original Hubbard model – violating particle number conservation. This can be seen from Eq. (4.26): Σ_{m-1}^\pm contains operator products $\sigma_j^+ \sigma_j^- = c_j^\dagger c_j$, which conserve the number of excitations, but also the operator $\sigma_m^x = \sigma_m^+ + \sigma_m^-$ that breaks particle number conservation.

Because of this problem we proceed with an alternative modeling of the CZ gates between distant qubits.

iSWAP chains. An alternative way to deal with a CZ gate where control and target are far apart, is to insert \pm iSWAPs as displayed in Fig. 4.7. An iSWAP between qubits j and k can be written as

$$\begin{aligned} \text{iSWAP}_{j,k} &= \sigma_j^+ \sigma_j^- \sigma_k^+ \sigma_k^- + \sigma_j^- \sigma_j^+ \sigma_k^- \sigma_k^+ + i(\sigma_j^+ \sigma_k^- + \sigma_j^- \sigma_k^+) \\ &= e^{i\frac{\pi}{2}(\sigma_j^+ \sigma_k^- + \sigma_j^- \sigma_k^+)}. \end{aligned} \quad (4.27)$$

Errors due to over-rotations appear in each gate. The contribution to the Hamiltonian from errors in the central CZ gate is not modified due to the chain of \pm iSWAPs. This can

be seen by introducing additional $\pm i$ SWAPs between the CZ gate and its errors, in analogy to the discussion presented above and illustrated in Fig. 4.4. Novel contributions arise due to over-rotations in the i SWAPs. Similar to the case of CNOT chains we consider a chain of i SWAPs as shown in Fig. 4.8. We allow for an over-rotation $\delta\varphi$ in the rightmost gate and, following the prescription explained in Sec. 4.1.2 (Case 2) commute it to the far left. Again, we commute the error gate by gate using Eq. (4.9). The first commutation yields

$$\text{Ad}_{i\text{SWAP}_{m-2,m-1}}(i\delta\varphi(\sigma_{m-1}^+\sigma_m^- + \sigma_{m-1}^-\sigma_m^+)) = i(\sigma_m^+(-\sigma_{m-1}^z)\sigma_{m-2}^- - \sigma_m^-(-\sigma_{m-1}^z)\sigma_{m-2}^+). \quad (4.28)$$

Proceeding iteratively until the error is shifted to the far left, one obtains the effective contribution to the simulated Hamiltonian,

$$\delta H(t) = \frac{n}{\tau}\delta\varphi(t)i^{m-2}\left(\sigma_m^+\prod_{k=2}^{m-1}(-\sigma_k^z)\sigma_1^- + (-1)^{m-2}\sigma_m^-\prod_{k=2}^{m-1}(-\sigma_k^z)\sigma_1^+\right). \quad (4.29)$$

While this looks like a complicated product of many operators, one finds after transforming it back to fermionic representation,

$$\sigma_m^+\prod_{k=2}^{m-1}(-\sigma_k^z)\sigma_1^- + (-1)^{m-2}\sigma_m^-\prod_{k=2}^{m-1}(-\sigma_k^z)\sigma_1^+ = c_m^\dagger c_1 + (-1)^{m-2}c_1^\dagger c_m, \quad (4.30)$$

i.e., the gate errors contribute hopping terms of the form $\delta t_{jk}c_j^\dagger c_k$ to the effective Hamiltonian. Analogous results follow for the chain of $-i$ SWAP gates when reversing the swap operations. This means that in the case of faulty i SWAPs we again introduce disorder to the simulated Hamiltonian. However, generalizing the original Hamiltonian, the errors introduce hopping terms between every pair (j, k) .

In summary: Errors occurring while performing the \mathbf{U} , \mathbf{t}_1 or \mathbf{t}_2 gates introduce disorder terms that are of the same form as the interaction, hopping or spin-flip terms which were already contained in the Hamiltonian, except that they introduce further interactions and transitions between the fermionic levels. Hence, the physical meaning was clear; we effectively simulate a disordered system. In the algorithm required to handle the Jordan-Wigner strings based on CNOT gates, over-rotation errors take us out of the scope of the unperturbed Hamiltonian and even introduce unphysical features such as violating the particle number conservation. A remedy is to handle the Jordan-Wigner strings using $\pm i$ SWAPs, which leads to a Hamiltonian consistent with conservation laws, but the price is that a much larger number of gates are needed, which may introduce quantitatively larger errors.

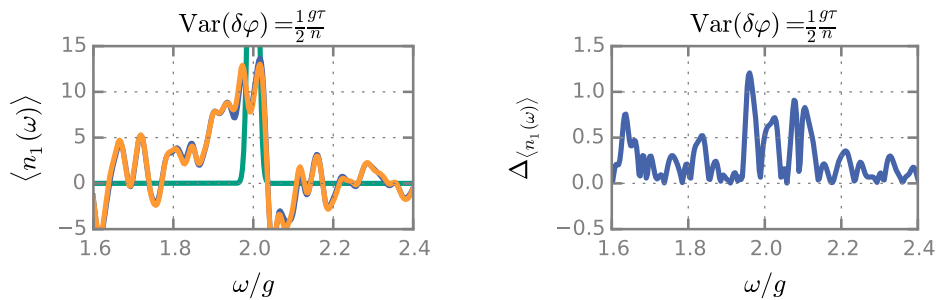


Figure 4.9: In the left panel a part of the Fourier spectrum $\langle n_1(\omega) \rangle$ is shown, where the green sharp peak is calculated with the ideal Hamiltonian H (and artificially broadened, see main text). The orange line is the calculation using the algorithm with gate errors by over-rotation, where we chose a large variance $\text{Var}(\delta\varphi) = \frac{1}{2} \frac{g\tau}{n}$ for the statistical gate errors. Under the orange line is a slightly deviating blue line representing the time evolution using the effective Hamiltonian $H + \delta H(t)$. In the right panel the difference $\Delta \langle n_1(\omega) \rangle$ between faulty algorithm and effective Hamiltonian calculation is shown on a much finer scale.

4.3 Numerical analysis

4.3.1 Verification of the method

The minimal model we have chosen is also suitable for a numerical analysis. For this purpose we choose in the Hamiltonian (4.16) the following parameters: $U = t_1 = t_2 = g$ and evaluate the time evolution of the initial state chosen as $|\psi(t=0)\rangle = c_2^\dagger c_1^\dagger |0\rangle$, where $|0\rangle$ is the vacuum state, up to the time $\tau = 1000/g$. We evaluate the probability of level 1 being occupied, $\langle n_1(t) \rangle = \langle c_1^\dagger(t) c_1(t) \rangle$, and its Fourier transform $\langle n_1(\omega) \rangle$. The time evolution is calculated in several ways:

(1) We use a Trotter expansion according to the algorithm depicted in Fig. 4.2, with the \mathfrak{t}'_2 decomposition using CZ gates depicted in Fig. 4.3. We Trotterize the time evolution with a fine step size $\frac{g\tau}{n} = 0.05$. After each Trotter step we evaluate $\langle n_1(t) \rangle$, such that every step defines a time slice. In each step we allow for each gate random over-rotations that are normally distributed with zero mean and given values of the variance.

(2) We use the effective disordered Hamiltonian $H + \delta H$, with H from Eq. (4.16) and the disorder terms $\delta H(t)$ derived in Sec. 4.2.2. We take the same time slices as in (1), and also the time-dependent disorder is chosen in accordance with the over-rotations in the respective Trotter steps.

(3) For comparison we also calculate numerically exact the discretized time evolution under the error-free Hamiltonian H .

In Fig. 4.9 we plot the result for a single run of the time evolution, where the random gate errors have a variance $\text{Var}(\delta\varphi) = \frac{1}{2} \frac{g\tau}{n}$. On the left, a part of the Fourier spectrum $\langle n_1(\omega) \rangle$ is shown. The green sharp peak corresponds to the ideal time evolution without errors. In this case the peak is artificially broadened; $\langle n_1(t) \rangle$ is calculated and multiplied by a Gaussian window function to ensure better convergence of the applied

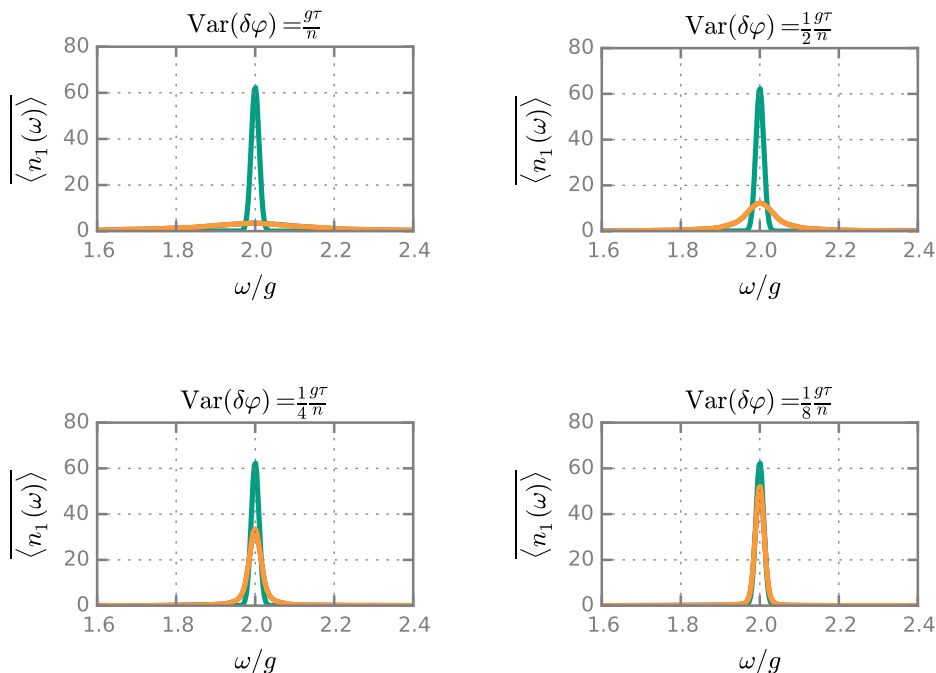


Figure 4.10: The Fourier spectrum $\overline{\langle n_1(\omega) \rangle}$ averaged over many runs of the calculation with different realizations of the random gate errors. The variance of the over-rotations $\text{Var}(\delta\varphi)$ differs in the four plots. The green curves are the spectrum for the ideal case with artificial broadening (see text), the orange ones show the results of the faulty algorithms. In this case, calculations based on the effective disordered Hamiltonian yield indistinguishable results. We find a broadening of the spectrum which scales with the strength of the over-rotations, corresponding to a system with disorder.

fast Fourier transform. The orange curve shows the distorted spectrum based on the Trotter expansion with gate errors. It strongly deviates from the ideal result since we have chosen a rather high variance of the gate errors. The orange line lies nearly on top of a blue line which represents the result following from the effective disordered Hamiltonian $H + \delta H(t)$. The small difference $\Delta_{\langle n_1(\omega) \rangle}$ between faulty algorithm and effective Hamiltonian with disorder is depicted on the right panel (note the difference in the scale). The comparison shows the equivalence of the faulty gates and the description by an effective disordered Hamiltonian.

While for the considered strong gate errors we find a strongly fluctuating distorted result for a single run, averaging over many runs with different random over-rotations produces smoother results. Fig. 4.10 shows the averaged result $\overline{\langle n_1(\omega) \rangle}$ for different variances of the normally distributed errors. We averaged over 1000 runs to guarantee for a smooth curve even for larger error variances. In green we depict again the ideal (artificially broadened) spectrum, in orange the result of the Trotterization with gate errors. After averaging, the description by the effective disordered Hamiltonian and by the Trotterization yield numerically indistinguishable results. As one could expect, errors lead to a broadening of the ideal spectrum which grows with the error variance.

The numerical analysis showed that strong statistically distributed over-rotations in the algorithm lead to a very distorted spectrum for individual runs, but averaging over many runs yields a spectrum with features equivalent to broadening by disorder. Overall we find that gate errors in the algorithm due to over-rotations are well described by an effective Hamiltonian with disorder as derived in Sec. 4.1.2 even for large gate errors.

4.3.2 Comparison of different implementations

We continue with the same model system as in the previous subsection and investigate now how gate errors in the different implementations of the Jordan-Wigner string discussed in Sec. 4.2.3, based either on CNOTs or on CZs with *i*SWAPs, influence the results. As discussed above we are prepared to discover different physics. We also vary the Trotter step size, as the effective disorder δH grows linearly with the number of Trotter steps (see Eqs. (4.6), (4.11), and Sec. 4.2).

Specifically we evaluate the spatial variance of excitations, $\langle \sigma^2(t) \rangle$, with

$$\sigma^2 = \sum_{j=1}^4 r_j^2 \tilde{n}_j - \left(\sum_{j=1}^4 r_j \tilde{n}_j \right)^2, \quad (4.31)$$

where $\tilde{n}_j = c_j^\dagger c_j / (\sum_{k=1}^4 c_k^\dagger c_k)$. The normalization is needed since for one of the algorithms the particle number is not conserved. We chose $r_1 = 0$, $r_2 = r_4 = 1$, and $r_3 = 2$.³ The spatial variance tells us how far excitations in the system are spread out, and thus provides information about charge diffusion [114, 115].

The time evolution under the Hamiltonian (4.16) is simulated with parameters as chosen before $U = t_1 = t_2 = g$, but for the initial state $|\psi(t=0)\rangle = c_1^\dagger |0\rangle$. We plot $\overline{\langle \sigma^2(t) \rangle}$ over t/g , i.e., the averaged result over many runs with random gate errors (normally distributed with zero mean). In this simulation, the errors are chosen to be quasi-static, i.e., for each run and gate a random over-rotation is chosen which does not vary for the different Trotter time steps, but different runs have different errors. Quasi-static errors are a valid noise model, e.g., for superconducting qubits where the noise spectrum is dominated by low frequencies [116]. The variance of the over-rotations $\text{Var}(\delta\varphi)$ and the Trotter step size $\frac{gT}{n}$ are parameters to be varied.

Fig. 4.11 shows the results. The dashed green line shows the error-free analytic result, where an excitation spreads across the system but then oscillates back due to the finite system size. The orange line represents a faulty algorithm using CZ and *i*SWAP gates for the Jordan-Wigner string (see Sec. 4.2.3). The induced disorder leads to a damping of the oscillation after averaging, i.e., it induces decoherence. The blue line displays the result of a faulty algorithm using CNOT gates for modeling the Jordan-Wigner string (see Sec. 4.2.3). As expected from the discussion in Sec. 4.2.3, in this algorithm the over-rotations lead to physics which differs from that produced by other algorithms. While

³Note that this choice for r_i represents the minimal number of hoppings to get an excitation from orbital 1 to orbital i . Applied to the minimal Hubbard model (with spin) discussed earlier one might choose the site locations $r_1 = r_4 = 0$, $r_2 = r_3 = 1$. The qualitative conclusions remain unchanged.

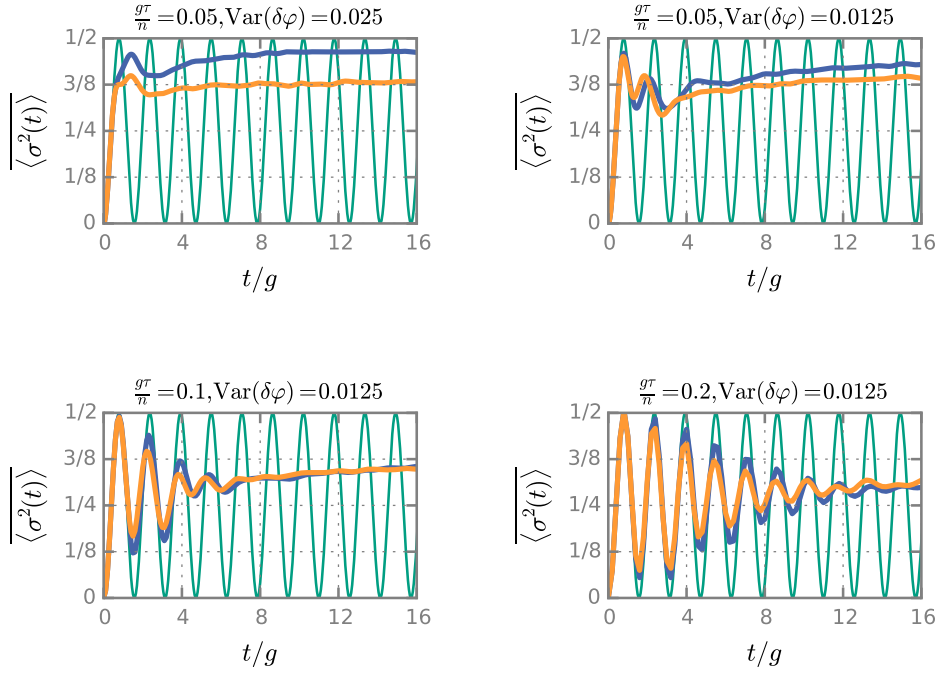


Figure 4.11: Simulation of the time evolution of the averaged spatial variance $\overline{\langle \sigma^2(t) \rangle}$ (see main text) using different algorithms with random quasi-static gate errors. The Trotter step size $\frac{g\tau}{n}$ and the variance of the over-rotations $\text{Var}(\delta\varphi)$ differ for each plot. The green line shows the ideal analytic result. The orange line represents a faulty algorithm using CZ and iSWAP gates for the Jordan-Wigner string. The blue line displays the result using CNOT gates for the Jordan-Wigner string. One can see how gate errors occurring in different algorithms lead to different physics, and how the influence of gate errors increases for shorter Trotter step size.

we find damping in all cases, the lines converge towards different values.⁴ The difference arises since the implementation based on CNOTs violates particle number conservation, and the system makes a transition from having a single excitation towards half filling. Responsible for this transition are errors which randomly excite or relax qubits and reach equilibrium at half filling (similar to classical noise leading to infinite temperature).

The results of this subsection illustrate how the choice of algorithm may affect the results of a digital quantum simulation. Another aspect illustrated in Fig. 4.11 is the fact that under the influence of gate errors it is – up to a certain point – advantageous to reduce the number of Trotter steps and thus of the gate numbers. The disorder of the effectively simulated Hamiltonian scales with their number (see Eqs. (4.6), (4.11), and Sec. 4.2). On the other hand, a coarse Trotterization leads to a large error from the Trotter expansion. Hence, there is an optimal number of Trotter steps to minimize the simulation error [70]. One should keep in mind that a finer Trotterization requires higher gate fidelities.

4.4 Gate fidelity and adiabatic state preparation

We extend the analysis of the above section with two remarks: One about the relation between gate fidelities and errors arising in the numerical simulations, the other about adiabatic state preparation [117] under the influence of disorder. In order to do this, let us first introduce the concept of gate fidelities and show their relation with over-rotations.

4.4.1 Fidelity of over-rotated gates

Before we derive the relation between the minimal gate fidelity \mathcal{F}_{\min} of faulty gate due to an over-rotation and the angle of over-rotation $\delta\varphi$, we first give a precise definition how we model an over-rotated gate. The gate is denoted by the unitary operator

$$U(\varphi) = e^{i\varphi A}, \quad (4.32)$$

where A is a Hermitian operator with a finite spectrum consisting of the eigenvalues $\lambda_1, \dots, \lambda_d$, where $|\lambda_j| \leq 1$, $\lambda_1 = 1$, and $\lambda_n = -1$. Note, that this is the case if A is a product of Pauli operators. In general, every finite Hermitian operator can be cast into this form through rescaling and shifting by constants. The faulty gate is represented by $U(\varphi + \delta\varphi)$, with an over-rotation angle $\delta\varphi$. Also the faulty gate error is therefore a unitary transformation.

Next, let us introduce *fidelities*: Consider two quantum states, denoted ψ and ϕ . In general they can be mixed states and characterized by their density matrices ρ_ψ and ρ_ϕ ,

⁴Note that the apparent different strength of the damping is due to a different total number of gates in the algorithm. Fewer gates result in fewer disorder terms in the effective Hamiltonian. This discrepancy disappears if one scales for the number of gates accordingly.

respectively. The fidelity $\mathcal{F}_{\psi,\phi}$ between the two states is defined as

$$\mathcal{F}_{\psi,\phi} = \text{Tr} \left(\sqrt{\sqrt{\rho_\psi} \rho_\phi \sqrt{\rho_\psi}} \right), \quad (4.33)$$

where $\text{Tr}(\cdot)$ denotes the trace, and $\sqrt{\rho_\psi}$ is an operator such that $\sqrt{\rho_\psi}^2 = \rho_\psi$ (which exists for density matrices, since they are positive semi-definite). Note, that this follows the notation of Nielsen and Chuang [63] and that often the square of $\mathcal{F}_{\psi,\phi}$ is called fidelity. The fidelity is also symmetrical with respect to interchanging ψ and ϕ , which is not obvious. The fidelity is an abstract, but widely used measure (with values between zero and one) to identify how close two quantum states are, where the fidelity is zero for orthogonal states, and one for identical states. We will now proceed with the definition of the *gate fidelity*.

With a unitary error model it is sufficient to regard pure states as input states. The fidelity between two pure states $|\psi\rangle$ and $|\phi\rangle$, i.e., with $\rho_\psi = |\psi\rangle\langle\psi|$ and $\rho_\phi = |\phi\rangle\langle\phi|$, is given by their overlap $|\langle\psi|\phi\rangle|$. This can be seen by using $\sqrt{|\psi\rangle\langle\psi|} = |\psi\rangle\langle\psi|$ for normalized states. Given an input state $|\psi_0\rangle$, the application of the gate would ideally yield the final state $U(\varphi)|\psi_0\rangle$ whereas the application of the over-rotated gate yields $U(\varphi + \delta\varphi)|\psi_0\rangle$. The minimal gate fidelity \mathcal{F}_{\min} is given by the overlap of the ideal and faulty final state, minimized over all input states, hence:

$$\begin{aligned} \mathcal{F}_{\min} &= \min_{|\psi_0\rangle} |\langle\psi_0|U^\dagger(\varphi)U(\varphi + \delta\varphi)|\psi_0\rangle| \\ &= \min_{|\psi_0\rangle} |\langle\psi_0|e^{i\delta\varphi A}|\psi_0\rangle|. \end{aligned} \quad (4.34)$$

Note, that this is again consistent with the definition of Nielsen and Chuang [63] and that often the square of \mathcal{F}_{\min} is called minimal gate fidelity.

We investigate the quantity to be minimized: One can diagonalize the Hermitian matrix $A = \text{diag}(\lambda_1, \dots, \lambda_d)$ and find its eigenbasis $\{|\lambda_1\rangle, \dots, |\lambda_d\rangle\}$. By writing $|\psi_0\rangle = \sum_{j=1}^d a_j |\lambda_j\rangle$ with $\sum_{j=1}^d |a_j|^2 = 1$ results in

$$|\langle\psi_0|e^{i\delta\varphi A}|\psi_0\rangle| = \left| \sum_{j=1}^d |a_j|^2 e^{i\delta\varphi\lambda_j} \right|. \quad (4.35)$$

Making use of the fact that the absolute value of a complex number is smaller than the magnitude of its real part for the expression $e^{i\delta\varphi\lambda_j} = \cos(\delta\varphi\lambda_j) + i\sin(\delta\varphi\lambda_j)$, we arrive at

$$|\langle\psi_0|e^{i\delta\varphi A}|\psi_0\rangle| \geq \left| \sum_{j=1}^d |a_j|^2 \cos(\delta\varphi\lambda_j) \right|. \quad (4.36)$$

It is reasonable to restrict $|\delta\varphi| \leq \pi/2$, since an over-rotation as a gate error should be

small. As $|\lambda_j| \leq 1$ it follows that $\cos(\delta\varphi\lambda_j) \geq \cos(\delta\varphi) \geq 0$, therefore

$$|\langle\psi_0|e^{i\delta\varphi A}|\psi_0\rangle| \geq \cos(\delta\varphi) \sum_{j=1}^d |a_j|^2 = \cos(\delta\varphi). \quad (4.37)$$

This establishes a lower bound of $\mathcal{F}_{\min} \geq \cos(\delta\varphi)$. For the special state

$$|\psi_{\min}\rangle = \frac{1}{\sqrt{2}}(|\lambda_1\rangle + |\lambda_d\rangle) \quad (4.38)$$

we indeed find

$$|\langle\psi_{\min}|e^{i\delta\varphi A}|\psi_{\min}\rangle| = \cos(\delta\varphi), \quad (4.39)$$

since $\lambda_1 = 1$ and $\lambda_d = -1$. Hence, the lower bound is actually tight and we obtain

$$\mathcal{F}_{\min} = \cos(\delta\varphi). \quad (4.40)$$

This concludes our derivation. Note, that the magnitude of the over-rotation $|\delta\varphi| = \arccos(\mathcal{F}_{\min})$ is in fact a metric, namely the Bures metric (resp. the Fubini-Study metric).

In an experiment $\delta\varphi$ is not fixed but rather a statistical variable. In this case it is sensible to consider the average minimal gate fidelity $\overline{\mathcal{F}}_{\min}$, i.e., the expectation value of \mathcal{F}_{\min} for a given distribution of $\delta\varphi$. For small $\delta\varphi$ one can expand Eq. (4.40), $\mathcal{F}_{\min} \approx 1 - \frac{\delta\varphi^2}{2}$, such that for a normally distributed $\delta\varphi$ with zero mean and variance $\text{Var}(\delta\varphi)$ we find $\overline{\mathcal{F}}_{\min} = 1 - \frac{\text{Var}(\delta\varphi)^2}{2}$.

4.4.2 Error size in the numerics

With the technicalities covered above, we study how large the errors assumed in the numerics of Sec. 4.3 are in terms of gate fidelities in order to estimate the applicability in actual experiments.

We have chosen the gate error strength to be independent of the Trotter step length. This covers, e.g., the case when the errors mostly arise from switching the control pulses. In addition, gate errors may increase with step length, e.g., if errors accumulate over time during the activation of a gate. These details depend on the actual hardware used in the experiment and what we described above represents an important limit. As a result of our assumption that the gate errors do not scale with the step size, the error-induced disorder scales linearly with n (see Eqs. (4.6), (4.11), and Sec. 4.2). Note, that this result is independent of the time dependence of the over-rotations $\delta\varphi(t)$, and hence of the time dependence of the disorder. Random gate errors with zero mean in the Trotter steps influence the simulation less severely than static errors.

Regardless of the error type, the gate errors have to be compared with errors arising from a non-vanishing Trotter step length. In our numerical simulations, the variance of the over-rotations $\text{Var}(\delta\varphi)$ was usually chosen to be comparable to the Trotter step size

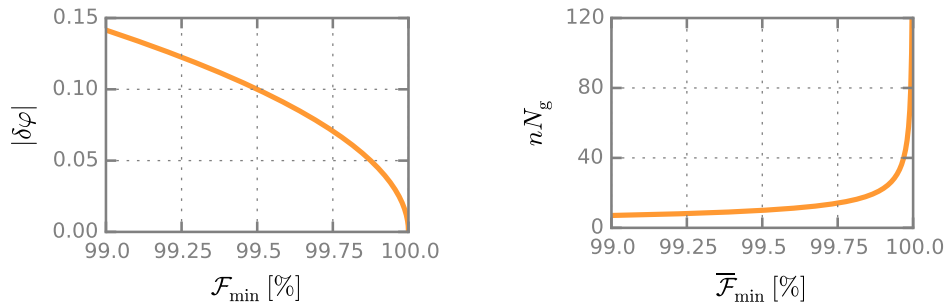


Figure 4.12: The left panel shows the over-rotation magnitude $|\delta\varphi|$ plotted over the minimal gate fidelity \mathcal{F}_{\min} of a faulty gate. The steep slope of $|\delta\varphi| = \arccos(\mathcal{F}_{\min}) \approx \sqrt{2(1 - \mathcal{F}_{\min})}$ as \mathcal{F}_{\min} approaches one requires gate fidelities to be very close to unity for the disorder in the effectively simulated Hamiltonian to be sufficiently low (the disorder strength scales linearly with $|\delta\varphi|$). The right plot shows the total number of faulty gates $N_g n$ that can be run for a given average minimal gate fidelity $\bar{\mathcal{F}}_{\min}$ according to Eq. (4.42). N_g is the number of faulty gates per Trotter step and n the number of Trotter steps.

$\frac{g\tau}{n}$, i.e., rather large. But as we chose a small step size to ensure the Trotter expansion to be valid, the resulting requirements on the gate fidelities are in fact rather high.

The strength of over-rotation is related to the minimal gate fidelity \mathcal{F}_{\min} . This was carefully derived in Sec. 4.4.1, but we can also make the connection more intuitive. As argued before, the application of a gate can be seen as a rotation of the state vector. In the worst case, a state vector orthogonal to the axis of rotation is over-rotated by an angle $\delta\varphi$. In this case, the absolute value of the inner product between ideal state vector and over-rotated state after the application of the gate is $\cos(\delta\varphi)$ (state vectors have unit norm). Hence, the magnitude of over-rotation and the minimum gate fidelity are related by $|\delta\varphi| = \arccos(\mathcal{F}_{\min})$. In our error analysis the value $|\delta\varphi|$ is the more useful measure for gate errors,⁵ since it linearly contributes to the strength of disorder in the effectively simulated Hamiltonian, and it has to be compared with the Trotter step size $\frac{g\tau}{n}$. In contrast, for the minimal gate fidelity \mathcal{F}_{\min} the question is how close it is to 100 %. For illustration we plot the relation between both in Fig. 4.12: It holds that $|\delta\varphi| = \arccos(\mathcal{F}_{\min}) \approx \sqrt{2(1 - \mathcal{F}_{\min})}$ for $\mathcal{F}_{\min} \approx 1$. The diverging slope requires \mathcal{F}_{\min} to get increasingly close to one to further reduce the disorder strength of the effective Hamiltonian. In the numerical results of Sec. 4.3.1 and Sec. 4.3.2 we used, e.g., $\text{Var}(\delta\varphi) = 0.025$ and $\text{Var}(\delta\varphi) = 0.0125$, which corresponds to an averaged minimal gate fidelity $\bar{\mathcal{F}}_{\min}$ of 99.969 % and 99.992 %, better than the values reached by present-day devices [34, 35, 38].

Averaging over the errors $\delta\varphi$ with a normal distribution and zero mean we find

$$\text{Var}(\delta\varphi) = \sqrt{2(1 - \bar{\mathcal{F}}_{\min})}, \quad (4.41)$$

where $\bar{\mathcal{F}}_{\min}$ denotes the averaged minimal gate fidelity. With this we can derive an estimate for the maximum number of Trotter steps for a given algorithm and gate

⁵As stated already in the above, the absolute value $|\delta\varphi|$ is in fact a metric called the Bures metric.

fidelity: As mentioned above (see Eqs. (4.6), (4.11), and Sec. 4.2), the disorder terms in the Hamiltonian have magnitude $\frac{n}{\tau} \text{Var}(\delta\varphi)$. If there are a total of N_g faulty (two-qubit) gates per Trotter step the total disorder is of magnitude $N_g \frac{n}{\tau} \text{Var}(\delta\varphi)$.⁶ The disorder strength should be (much) lower than the Hamiltonian energy scale g . If we set $\tau \sim \frac{1}{g}$ (see below), and use Eq. (4.41) for the over-rotation variance we arrive at

$$nN_g < \frac{1}{\sqrt{2(1 - \bar{\mathcal{F}}_{\min})}}. \quad (4.42)$$

This sets a limit on the maximum number of Trotter steps n and the maximum system size, which determines the number of faulty (two-qubit) gates N_g per Trotter time step. What we found here is a rough and worst-case estimate, but it illustrates that gate fidelities must be well above 99.9% to allow for a large number of gates (see Fig. 4.12).

There is a natural time scale of the dynamics of the Hamiltonian associated with its energy scale g . To resolve the relevant dynamics one has to simulate for times up to $\tau \sim \frac{1}{g}$. This yields a Trotter step size $\frac{g\tau}{n} \sim \frac{1}{n}$. For a gate fidelity of 99.0%, which can be reached by present day technology, it means $\text{Var}(\delta\varphi) \approx 0.142$, therefore the error quickly becomes stronger than $\frac{1}{n}$ for increasing n . Accordingly, the number of Trotter steps is very limited for current experimental gate fidelities [70]. In fact, for the algorithm of the previous subsection (Sec. 4.3.2) we found that a gate fidelity above 99.99% is necessary to allow for enough Trotter steps before the simulation shows the expected relaxation to an overdamped limit.

4.4.3 Adiabatic state preparation

An important problem to solve for digital quantum simulators is how to prepare non-trivial states in these devices. With the relation between gate fidelity and over-rotations at hand, we have also studied how adiabatic state preparation – as a possible solution to this problem – would perform with current state-of-the-art fidelities. Unfortunately, we found the time-dependent disorder induced by the gate errors to be very problematic during an adiabatic time evolution. During the adiabatic evolution the system is required to stay in an eigenstate while the system parameters are slowly changing (e.g., the on-site interaction U is adiabatically turned on). Gaps in the spectrum protect from crossings to different eigenstates as long as the time scale of the evolution is long enough. If the time evolution is influenced by time-dependent disorder, level crossings may occur if the energy scale of the disorder is comparable to the gap size in the spectrum.

In numeric calculations we found that even very low disorder hinders an adiabatic evolution to a final state with the correct properties. Due to the large number n of Trotter steps in a (slow) adiabatic time evolution, increasingly high fidelities would be needed to keep the disorder negligibly low, since it grows linearly with n (see Eqs. (4.6), (4.11),

⁶Note that this estimate involves using the triangle inequality $\|\sum_{j=1}^{N_g} A_j\| \leq \sum_{j=1}^{N_g} \|A_j\| = N_g$ (here $\|A_j\| = 1$ for all j). It is therefore a worst-case scenario where all gate errors of independent gates add up adversely. The number N_g could effectively be much lower.

and Sec. 4.2). In fact even for the small system under consideration and a gate fidelity of 99.9% (i.e., slightly better than currently available devices), simulations of the adiabatic evolution did not show an improvement from the initial state (the non-interacting ground state) towards the ground state of the interacting system (with on-site interaction). By improvement we mean an increase in the state overlap with the actual ground state. Rather, the initial situation was made worse; regardless of whether or not we tried to trade gate errors for Trotter errors by reducing n .

Hence, different approaches should be used for the state preparation in a digital quantum simulation without error correction, such as e.g., variational approaches [51, 52]. These algorithms need significantly less gates than an adiabatic time evolution. The much lower number of Trotter steps required reduces the disorder introduced in the simulation. Furthermore, these approaches can generally mitigate gate errors [118]. In the next chapter, we will investigate the performance of variational algorithms and compare with the adiabatic evolution. As we will see, it appears promising that variational methods could allow for efficient ground state preparation even with faulty gates.

4.5 Chapter conclusion

In this chapter we analyzed the effect of gate errors occurring during a digital quantum simulation of the time evolution of a quantum system with Hamiltonian H using algorithms based on the Trotter expansion. We showed that gate errors due to over-rotations effectively introduce an extra term $\delta H(t)$ in the Hamiltonian, which in many cases can be interpreted as a time-dependent disorder term. However, we also demonstrated that the nature of these contributions depends on the choice of the algorithms and that different algorithms may introduce different physics in a faulty simulation. The method was then applied to an explicit example, a Fermi-Hubbard model with spin-flip interaction, analyzed by algorithms based on various two-qubit gates. The example also demonstrates how the effects of over-rotations depend on the choice of algorithms. For instance in the example of Sec. 4.2.2 we showed that replacing CZ gates by a chain of CNOTs introduces unphysical multi-particle interactions violating particle conservation.

We also illustrated our findings by a numerical analysis of a small model system. The method can be extended beyond the small system. In such cases the algorithms can be performed and analyzed piecewise. In particular, the findings of Sec. 4.2.2 are valid for a large class of Hubbard-like Hamiltonians with general hopping terms $t_{jk}c_j^\dagger c_k$ and density-density interactions $V_{jk}c_j^\dagger c_j c_k^\dagger c_k$. This covers a wide variety of problems in quantum chemistry and solid state physics.

The method can also be extended to higher order Trotter expansions. For the second order expansion one has to require that over-rotations are restricted to $|\delta\varphi| \leq (\frac{g\tau}{n})^2$.

We established a connection between the errors due to over-rotation of gates and their fidelities in Sec. 4.4. This enables us to quantify the strength of the disorder in the effective Hamiltonian for a given fidelity and Trotter step size. We have to conclude that fidelities as presently achieved in experiments impose severe limitations on useful

applications. The quality of gates has to improve, i.e., the strength of error should decrease by orders of magnitude to allow for a useful number of Trotter steps without introducing too much disorder in the simulation. The induced disorder is particularly harmful to adiabatic state preparation.

Following Eq. (4.42), we find that gate fidelities of 99% only allow for approximately 10 gates to run in an algorithm. To allow for 100 gates, fidelities should improve towards 99.99%. But we would like to stress again that our modeling provides a worst-case estimate. For instance, the effective number of faulty gates N_g per Trotter step in Eq. (4.42) may be smaller than the number of two-bit gates since errors of independent gates do not need to add up adversely. In addition, our estimates are based on the assumption that gate errors are solely caused by over-rotations. In reality, there is a variety of error sources that reduce the measured gate fidelities. Other sources of errors and a combination of different errors might lead to a different scaling behavior, especially when gates could, e.g., be run in parallel. While parallelization would not make any difference in the case of pure over-rotation errors, it could greatly reduce the impact of environmentally induced decoherence.

An alternative route would be to combine digital quantum simulations with analog quantum emulations. For this purpose a part of the simulator should have a Hamiltonian which coincides with a part of the Hamiltonian of the system to be simulated. This block of the Hamiltonian evolves by itself, without the need of employing a Trotter expansion and applying appropriate gates [1, 119]. In this way the overall gate count can be lowered substantially.

Finally, we like to mention that the disorder arising from faulty gates in principle could correspond to disorder in natural systems which one might want to simulate. On the other hand, in realistic setups the disorder due to faulty gates may usually be stronger than what one intends to simulate.

Overall, we demonstrated in this chapter that the effects of gate errors in a digital quantum simulation of (fermionic) systems can be understood on the level of modified effective Hamiltonians, and the strength of the contributions from errors can be quantified for a given Trotter step size and gate fidelity.

The following chapter will analyze another promising approach for the application of imperfect quantum devices without error correction, namely variational algorithms. They show great performance despite a low number of necessary Trotter steps and the potential to mitigate errors. In the next chapter we will investigate explicitly the performance of a particular variational algorithm under the influence of over-rotation gate errors as presented in this chapter.

Chapter 5

Variational ground state preparation with gate errors

This chapter is based on the the publication

[3] J.-M. Reiner, F. Wilhelm-Mauch, G. Schön, and M. Marthaler, *Finding the ground state of the Hubbard model by variational methods on a quantum computer with gate errors*, Quantum Sci. Technol. **4**, 035005 (2019).

Reprinting of copyrighted material from this publication is explicitly permitted within this thesis by IOP Publishing Ltd.

In the previous chapter we investigated the effect of over-rotation gate errors on digital quantum simulation. One result was that, unfortunately, assuming realistic gate fidelities the total gate count that is feasible in a static simulation based on a Trotter expansion is very limited. Particularly, adiabatic preparation of the ground state of a small Hubbard model proved to be impossible as long as the gate fidelities were assumed to be within reach for state-of-the-art quantum devices. However, the preparation of non-trivial ground states, e.g., of model systems like the Hubbard model, is precisely one of the highly anticipated applications of digital quantum simulators. To utilize near-future quantum hardware – without quantum error correction – one has to find algorithms with very efficient gate count and a certain resilience to noise.

For the simulation of the ground state of a quantum system, it has been suggested and demonstrated in few-qubit experiments that variational algorithms require only a relatively low number of gates and, in addition, variational methods intrinsically suppress the impact of errors [51, 118, 120]. Such algorithms were described already in Sec. 2.4, but we repeat the main concept here again briefly. In general, variational approaches apply a unitary operator to an initial state $|\psi_0\rangle$ that is easy to prepare. The unitary operator $U(\boldsymbol{\theta})$ depends on a set of parameters $\boldsymbol{\theta}$ that is varied to minimize the energy

$$E(\boldsymbol{\theta}) = \langle \psi_0 | U^\dagger(\boldsymbol{\theta}) H U(\boldsymbol{\theta}) | \psi_0 \rangle \quad (5.1)$$

where H is the Hamiltonian of the system of interest.

In this chapter we study explicitly the effect of gate errors on a variational algorithm for finding the ground state of the Hubbard model. We will use a specific variational ansatz, namely the variational Hamiltonian ansatz (VHA) [52]. It is inspired by the adiabatic ground state evolution as explained in more detail below. Specifically, we address the following questions: How close can $E(\boldsymbol{\theta})$ get to the ground state energy E_g of the Hamiltonian H , and how close can $U(\boldsymbol{\theta})|\psi_0\rangle$ approximate the true ground state of H , if gate errors occur during the implementation of the unitary operator $U(\boldsymbol{\theta})$.

Generally the specific nature of gate errors is not known, therefore we work with the simple but representative model from Chap. 4. Every gate can be interpreted as a rotation of the qubit register. In our model gate errors are modeled as over-rotations (or under-rotations). As discussed in Chap. 4, specifically Sec. 4.4.1, the over-rotation angle $\delta\varphi$ can be related to the minimal gate fidelity \mathcal{F}_{\min} of the gate via $\mathcal{F}_{\min} = \cos(\delta\varphi)$. Because of the vanishing slope of the cosine at the maximum (i.e., $|\delta\varphi| = \arccos(\mathcal{F}_{\min}) \approx \sqrt{2(1 - \mathcal{F}_{\min})}$ for $\mathcal{F}_{\min} \approx 1$) gate fidelities need to get very close to 100 % to significantly limit the magnitude of the over-rotations.

Below we also compare the VHA to the adiabatic state preparation based on the Trotter expansion. We find that the VHA produces a better approximation to the ground state with far fewer steps, and therefore gates, than adiabatic state preparation. For adiabatic state preparation, even for weak gate errors, upon increasing the number of steps, the states created have decreasing overlap with the actual target ground state. In contrast, the VHA achieves high overlap with the exact ground state; even with gate errors. This is due to the error mitigation capabilities of variational approaches. For the (still small-size) Hubbard model considered as an example in the following we find that a gate fidelity of $\mathcal{F}_{\min} = 99.9\%$ is sufficient for a meaningful simulation.

5.1 From the adiabatic evolution to the variational Hamiltonian ansatz (VHA)

The unitary operator $U(\boldsymbol{\theta})$ of the variational Hamiltonian ansatz is based on the Hamiltonian itself: The different terms of H are separated and grouped into N sub-operators H_1, \dots, H_N such that $H = \sum_{\alpha=1}^N H_{\alpha}$. The unitary operator for the VHA with n steps is

$$U(\boldsymbol{\theta}) = \prod_{k=1}^n \prod_{\alpha=1}^N e^{i\theta_{\alpha,k} H_{\alpha}}, \quad (5.2)$$

where $\boldsymbol{\theta}$ collects all the variational parameters $\theta_{\alpha,k}$. The optimization criterion is the minimization of the energy expectation value (5.1) of the final state $|\psi_f\rangle = U(\boldsymbol{\theta})|\psi_0\rangle$ with respect to the $n \cdot N$ variation parameters $\boldsymbol{\theta}$ (the ground state is, per definition, the state with minimal energy).

The ansatz (5.2) is inspired by the adiabatic time evolution under the influence of

the Hamiltonian $H = H_0 + V$ composed of, e.g., a non-interacting part H_0 and the interaction V . If the interaction is turned on slowly on the time scales given by the inverse energy scales of the Hamiltonian, the initial ground state $|\psi_0\rangle$ of H_0 develops adiabatically into the ground state $|\psi_g\rangle$ of H (if the conditions of the adiabatic theorem are fulfilled). To simulate this evolution in a Trotter expansion the time τ of the evolution is divided into a large number n of Trotter time steps $\frac{\tau}{n}$, each shorter than the inherent time scales, leading to

$$U_{\text{ad}} = \prod_{k=1}^n e^{-i\frac{\tau}{n}H_0} e^{-i\frac{\tau}{n}V}. \quad (5.3)$$

During each of the short time steps one further decomposes the Hamiltonian into sub-operators. In a simulation using an available quantum computer the sub-operators are chosen such that the short time evolution can be realized by the available gate operations.

The similarity between the operators (5.2) and (5.3) justifies the expectation that the VHA can produce the evolution from a ground state $|\psi_0\rangle$ of the non-interacting system to the ground state $|\psi_g\rangle$ of the full Hamiltonian. In addition, by introducing variational parameters the VHA can deviate from the adiabatic path and follow, through optimization, a more efficient one. Having a more efficient evolution via VHA allows for greatly reducing the necessary number of steps n , as compared to the number of Trotter steps in an adiabatic evolution, while still achieving high accuracy.¹ Moreover, by optimizing the variational parameters one also mitigates the error introduced by faulty gates, an effect which had been termed *variational error suppression*.

5.2 Model Hamiltonian and its decomposition

The model system we investigate in this chapter is again the Hubbard Hamiltonian of spin- $\frac{1}{2}$ fermions

$$H = -t \sum_{\substack{\langle j,j' \rangle \\ s=\uparrow,\downarrow}} (c_{j,s}^\dagger c_{j',s} + c_{j',s}^\dagger c_{j,s}) + U \sum_j c_{j,\uparrow}^\dagger c_{j,\uparrow} c_{j,\downarrow}^\dagger c_{j,\downarrow}, \quad (5.4)$$

with hopping amplitude t between nearest neighbors $\langle j, j' \rangle$, on-site energy U , and $c_{j,s}^{(\dagger)}$ being the annihilation (creation) operator of a fermion on site j with spin s . In the following we consider two-dimensional square lattices and focus on the parameter values $U = 2t$ with repulsive on-site interaction, $U > 0$.

For the implementation of the variational unitary operation of Eq. (5.2) we separate the Hamiltonian into $N = 5$ parts: The non-interacting part is split into four terms, H_1, \dots, H_4 , as illustrated by Fig. 5.1. We distinguish between hopping terms in horizontal and vertical direction and for each direction we group even and odd terms, i.e.,

¹Note that to a certain degree the ansatz also helps us to cope with the so called Trotter error, which is the error introduced by decomposing the time evolution operator using a finite number of Trotter steps and grows as the number of steps is reduced.

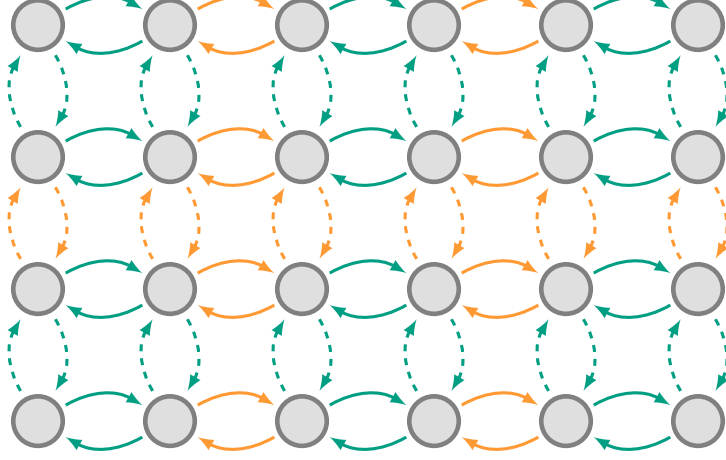


Figure 5.1: Sketch of the 2D Hubbard model on a square lattice. The arrows indicate the hopping terms between neighboring sites. For the simulation we divide them into four sets: First in horizontal (solid lines) and vertical (dashed lines) directions. Then we subdivide for each direction into even (green) and odd (orange) terms. Summing up all hopping terms for each of the four sets yields the sub-Hamiltonians H_1, \dots, H_4 . Note that the hopping terms within a set commute among each other.

every other term in each direction of the 2D system. The on-site interaction terms are collected in H_5 . Note, that all terms collected within one H_α commute among each other. Hence, the execution of an exponential $e^{i\theta_{\alpha,k}H_\alpha}$ in Eq. (5.2) can be performed exactly by sequentially applying the gates that account for the individual terms, without introducing an error associated with the Trotter expansion.

As written explicitly above we introduce a manageable number of 5 variational parameters per step and – as the example below shows – we reach high-quality results already for 10 steps or less.

5.3 Mapping to qubits and gate sequence

The mapping of the fermionic system onto qubits and the gate sequence to implement the VHA evolution is very similar to the methods used in Chap. 4. The mapping onto a qubit system is performed again via the Jordan-Wigner transformation. Gates performing on-site interaction terms are realized by ZZ -type interactions between qubits, hopping terms require $XX + YY$ interactions (similar to XX interactions in the rotating frame). In addition the transformation introduces Jordan-Wigner strings which are implemented by additional chains of controlled Z gates. To be more precise, we will show the gate sequence producing the unitary transformation $e^{i\theta_{\alpha,k}H_\alpha}$ from Eq. (5.2):

The different H_α , introduced above, contain either hopping terms $-t(c_{j',s}^\dagger c_{j,s} + c_{j',s}^\dagger c_{j,s})$ or on-site interactions $U c_{j,\uparrow}^\dagger c_{j,\uparrow} c_{j,\downarrow}^\dagger c_{j,\downarrow}$. We assume that the hardware of the quantum computer allows for ZZ -like and $XX + YY$ interaction and, for simplicity, unrestricted connectivity between the qubits. As mentioned above, the terms summarized in each of the H_α commute among each other making their ordering irrelevant.

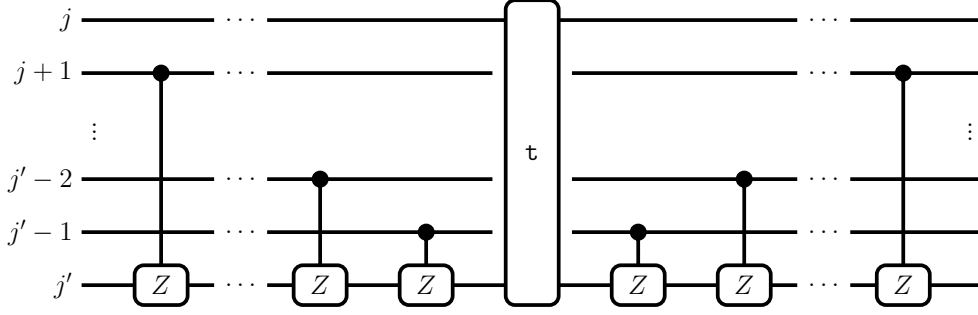


Figure 5.2: A \mathfrak{t} gate implementing an $XX + YY$ interaction between qubits j and j' is nested between controlled Z gates. The CZ gates introduce a Jordan-Wigner string such that the gate sequence implements a fermionic hopping term between the orbitals j and j' .

For the following discussion it is convenient to absorb the spin index in a consecutive numbering of the lattice sites via $(j, \uparrow) \mapsto j$ and $(j, \downarrow) \mapsto j + M$ where M is the total number of sites, similar to our approach in Chap. 3. We apply again the Jordan-Wigner transformation (introduced in Sec. 2.1.1):

$$c_j = \prod_{k=1}^{j-1} (-\sigma_k^z) \sigma_j^- . \quad (5.5)$$

The on-site terms now read $U \sigma_j^+ \sigma_j^- \sigma_{j+M}^+ \sigma_{j+M}^-$. In the variational approach the gate

$$e^{i\theta U \sigma_j^+ \sigma_j^- \sigma_{j+M}^+ \sigma_{j+M}^-} \quad (5.6)$$

needs to be implemented with some parameter θ . This is essentially a U gate from Sec. 4.2.2. It embodies a ZZ interaction (up to some single-qubit phases, which one can see by using $\sigma^+ \sigma^- = \frac{1}{2}(\sigma^z + 1)$). To account for the gate errors we add an over-rotation $\delta\theta$ to the parameter, the size of which depends on the assumed gate fidelity.

The hopping terms (where, say, $j < j'$) transform to $-t(\sigma_j^+ \sigma_{j'}^- \prod_{l=j+1}^{j'-1} (-\sigma_l^z) + \text{H.c.})$. We do not assume the hardware to allow for more than two-qubit interactions. A hopping term without residual Jordan-Wigner string $\prod_{k=1}^{j-1} (-\sigma_k^z)$, can be modeled by the $XX + YY$ interaction, i.e.,

$$e^{-i\theta t(\sigma_j^+ \sigma_{j'}^- + \sigma_{j'}^+ \sigma_j^-)} . \quad (5.7)$$

This we denote as \mathfrak{t} gate (see Sec. 4.2.2). Again, gate errors lead to an over-rotation $\delta\theta$ to be added to the parameter θ . Residual Jordan-Wigner strings can then be implemented by sandwiching the \mathfrak{t} gate with controlled Z gates (CZ) as displayed to Fig. 5.2, which is similar to the \mathfrak{t}'_2 gate in Sec. 4.2.2. The CZ gate has again ZZ -like interaction, and we implement it as $e^{i\pi \sigma_j^+ \sigma_j^- \sigma_{j'}^- \sigma_{j'}^+}$ for the control qubit j and the target qubit j' . Over-rotations are introduced as an addition $\delta\varphi$ to the angle π .

5.4 Error model and procedure

The goal is to prepare the ground state $|\psi_g\rangle$ of the Hubbard model (5.4) on a quantum computer. We start from the ground state $|\psi_0\rangle$ of the non-interacting model ($U = 0$),² which – in principle – can be prepared efficiently on a quantum computer [121], and we apply the variational Hamiltonian ansatz in order to evolve this state towards $|\psi_f\rangle$, which should be close to the ground state $|\psi_g\rangle$. We modeled the algorithm and the quantum gates including the gate errors on a classical computer. For the system sizes considered, $|\psi_0\rangle$ and $|\psi_g\rangle$ (without errors) can also be found exactly through classical numerical diagonalization. This allows us to test the quality of the results.

The unitary evolution is implemented by the gate based algorithm described in the preceding section. Each gate can be written in the form $e^{i\varphi A}$ with a real angle φ and an operator A composed of Pauli operators. Hence, it can be interpreted as a rotation of the quantum state. We use the gate error model from Chap. 4 and represent unitary gate errors by over-rotations $\delta\varphi$ (which may be positive or negative), such that the faulty gate reads $e^{i(\varphi+\delta\varphi)A}$. The magnitude of the random $\delta\varphi$ is given by the minimal gate fidelity \mathcal{F}_{\min} , where $\mathcal{F}_{\min} = \cos(\delta\varphi)$, as derived in Sec. 4.4.1. Performing a sequence of gates with random normally distributed over-rotations with zero mean and variance $\text{Var}(\delta\varphi)$ one finds – for weak over-rotations, i.e., fidelities close to one – an averaged minimal gate fidelity $\overline{\mathcal{F}}_{\min} = 1 - \text{Var}(\delta\varphi)^2/2$. When we introduce gate errors in the following, we assume a certain gate fidelity $\overline{\mathcal{F}}_{\min}$ and add random over-rotations to each gate according to the above relation. However, once the over-rotation for a specific gate is chosen, this value is kept constant during the consecutive stages of the optimization process. This accounts for quasi-static errors, which are considered an appropriate noise model for superconducting qubits, where the noise spectrum is dominated by low frequencies [116].

Finally, for given gate fidelities, we measure the performance of the VHA by evaluating the *final state fidelity*. This quantity is defined as the absolute value of the overlap $|\langle\psi_g|\psi_f\rangle|$ between the exactly known ground state $|\psi_g\rangle$ and the final state $|\psi_f\rangle = U(\boldsymbol{\theta})|\psi_0\rangle$ of the VHA according to Eq. (5.2), after the optimization of the parameters $\boldsymbol{\theta}$.³

5.5 VHA versus adiabatic evolution

We first study the quality of the variational Hamiltonian ansatz, Eq. (5.2), in comparison to the adiabatic evolution, Eq. (5.3). In both cases we start from the same initial state $|\psi_0\rangle$. For the comparison, the same number of steps n (steps of the VHA or Trotter steps) and the same gate sequence is used (with appropriately different parameters).

²Note that the non-interacting system has a degenerate ground state. We hand-picked the correct ground state $|\psi_0\rangle$ that evolves towards $|\psi_g\rangle$ when performing the VHA or the adiabatic evolution. To do this, we analyzed the spectrum where we lifted the degeneracy by applying a small perturbation through on-site interactions of negligible strength.

³Note that frequently the square of the overlap is denoted as state fidelity. We chose it such that it is consistent with our definition of the gate fidelity (see Sec. 4.4.1).

		Adiab. evo., 2×2						VHA, 2×2			
		$\overline{\mathcal{F}}_{\min} [\%]$						$\overline{\mathcal{F}}_{\min} [\%]$			
		100.0	99.99	99.90			100.0	99.99	99.90	99.90*	
	2	98.87	98.73	97.43	2		99.68	99.63	99.24	94.44	
	3	99.15	98.85	96.28	3		100.0	99.95	99.56	93.54	
n	4	99.23	98.95	96.51	n	4	100.0	99.96	99.68	88.77	
	5	99.55	99.14	95.62	5		100.0	99.98	99.82	83.69	

Table 5.1: The final state fidelity $|\langle \psi_g | \psi_f \rangle|$ for a given initial state $|\psi_0\rangle$ in percent for different numbers of (Trotter) steps n and different values of the average minimal gate fidelity $\overline{\mathcal{F}}_{\min}$ for a 2×2 Hubbard system. The left side shows the results of the adiabatic evolution, the right side of the VHA. Note the significantly better performance of the VHA as compared to the adiabatic evolution. For the data of the rightmost column denoted with 99.90*, instead of optimizing the parameters for the faulty gates, we used the parameters as obtained for optimizing with 100% fidelity. The comparison demonstrates the capabilities of the VHA in mitigating the errors.

For low n , the gate sequence introduces an error while implementing the exponential $e^{-i\frac{\tau}{n}H_0}$ for the adiabatic evolution, since the summands of H_0 do not commute. But for the comparison with the VHA at equal gate count we did not introduce finer Trotter time steps. On the other hand, the time τ in the adiabatic evolution was optimized for the given number of Trotter steps n .

Table 5.1 shows the results for a two-dimensional Hubbard lattice with 2×2 sites. We present the final state fidelity $|\langle \psi_g | \psi_f \rangle|$ in percent after performing, on one hand, the adiabatic evolution and, on the other hand, the VHA for different numbers of (Trotter) steps n and different averaged minimal gate fidelities $\overline{\mathcal{F}}_{\min}$. The algorithm we used requires 20 two-qubit gates per (Trotter) step, i.e., in total we perform from 40 to 100 two-qubit gates.

Even for perfect gate fidelities of 100% the adiabatic evolution does not improve the state fidelity significantly if we increase n . (Note, that the initial state fidelity $|\langle \psi_g | \psi_0 \rangle| = 98.87\%$ is already high due to the small system size; no improvement could be achieved for $n = 2$.) For a lower gate fidelity of 99.99% the adiabatic evolution barely increases the final state fidelity above 99%. For still lower gate fidelity of 99.9% the adiabatic evolution fails to improve the final overlap altogether. This was to be expected from the results of the previous chapter, where we – following Eq. (4.42) – provided estimates for the maximum number of gates that can be handled for a given gate fidelity in a quantum simulation with fixed parameters. Indeed for a gate fidelity of 99.9% the gate count for the adiabatic evolution exceeds this limit (of roughly 10 gates).

On the other hand, we observe significantly better performance for the VHA. For perfect gates two steps give already a very high final state fidelity; only three steps are necessary to achieve essentially a perfect result (an error of about 10^{-12} was observed, which is within numerical inaccuracies). Even with gate errors present we achieve high final state fidelities. The numbers clearly show that introducing more steps helps suppressing the quasi-static errors considered here.

The rightmost column, labeled by 99.90*, illustrates the error mitigation provided by

the VHA. For the data in this column we took the optimized parameters for perfect gates and used them in the evolution according to Eq. (5.2) with faulty gates with $\overline{\mathcal{F}}_{\min} = 99.9\%$ without any further optimization. This procedure does not take advantage of the potential of the VHA for error mitigation. The low performance of this method illustrates the power of variational error suppression.

The set of gate errors are chosen random but fixed (static) for both methods. However, in different runs they are chosen independent corresponding to the given gate fidelities. The results of Table 5.1 are averaged over many runs with different sets of errors. We can add that the error suppression of the VHA also reduces the standard deviation of the results for different error sets significantly. For the adiabatic evolution and lower gate fidelities we needed of the order of 10^5 runs in order to reach the shown accuracy of the average. The VHA, on the other hand, needs only a low number of runs for larger n (of the order of 10), even for low gate fidelities, to achieve the same accuracy, and even a single run is already quite reliable.⁴

5.6 Scaling up

Next we extend the analysis of the variational Hamiltonian ansatz to larger systems. Table 5.2 shows the final state fidelity $|\langle\psi_g|\psi_f\rangle|$ for various step numbers n and gate fidelities $\overline{\mathcal{F}}_{\min}$, now for the VHA applied to a 3×2 and a 3×3 Hubbard model. Here we show the results obtained for a single realization of the gate errors for each gate fidelity and step number. Statistical fluctuations are reduced due to the large number of gates per step. Averaging would introduce only small differences to the data presented. It can be ignored, especially for $n > 6$ where the variational error suppression is strong. For the 3×2 and 3×3 systems the algorithm requires 44 and 81 two-qubit gates per iteration step, respectively, i.e., overall up to 810 two-qubit gates were applied to the initial state.

We find again that the VHA produces very high final state fidelities. However, we also notice how high gate fidelities are necessary for a good performance of the algorithm. For a gate fidelity of $\overline{\mathcal{F}}_{\min} \leq 99.9\%$ which should be accessible in the next few years, we did not reach final state fidelities above 99%.

Further investigations showed that the limited final state fidelities are not necessarily a flaw of the VHA itself but rather of the required optimization. For increasing system size we found the results to be more and more sensitive to the choice of start parameters for the optimization problem. This suggests that the optimizer does not find the global optimum for the parameters but gets trapped in local extrema. The data of Table 5.2 (and Table 5.1) were obtained with a rather limited set of start parameters. We will now state how we chose the initial parameters in the above and give a larger set of start parameters that will be tested below in Sec. 5.6.2.

⁴This also alleviates the optimization overhead of the VHA; the algorithm has to be reinitiated hundreds of times in order to optimize the variational parameters.

		VHA, 3×2				
		$\overline{\mathcal{F}}_{\min} [\%]$				
		100.00	99.999	99.990	99.900	99.500
n	4	99.65	99.58	99.34	97.93	94.86
	6	99.81	99.85	99.74	98.24	97.26
	8	99.98	99.91	99.61	98.98	96.12
	10	100.0	99.95	99.82	98.83	97.78
		VHA, 3×3				
		$\overline{\mathcal{F}}_{\min} [\%]$				
		100.00	99.999	99.990	99.900	99.500
n	4	99.10	98.97	98.23	95.60	86.24
	6	99.59	99.46	99.27	95.55	90.06
	8	99.93	99.74	99.01	97.35	90.14
	10	99.97	99.89	99.77	98.04	90.69

Table 5.2: Again the final state fidelity $|\langle \psi_g | \psi_f \rangle|$ in percent for different values of n and $\overline{\mathcal{F}}_{\min}$, this time for the variational Hamiltonian ansatz in a 3×2 and a 3×3 system.

5.6.1 Choice of start parameters

When using the VHA, in order to minimize the energy according to Eq. (5.1), one has to start with an initial guess for the parameters θ . In Table 5.1 and Table 5.2 for each value of n and $\overline{\mathcal{F}}_{\min}$ we tried three different sets of start parameters, motivated by some physical reasoning:

(1) Since the VHA is inspired by the adiabatic evolution one of our choices of parameters $\theta_{\alpha,k}$ from Eq. (5.2) was to mimic the adiabatic evolution. We set $\theta_{\alpha,k} = \frac{1}{t}$ for $\alpha \in \{1, \dots, 4\}$ (i.e., the hopping elements) and $\theta_{5,k} = \frac{k}{n} \frac{1}{t}$ (i.e., the interaction terms), with t being the hopping energy of the Hamiltonian (5.4). This represents the adiabatic evolution (5.3) during time $\tau = \frac{n}{t}$.

(2) We chose a parameter set where not only the interaction but also the hopping is turned on gradually, i.e., $\theta_{\alpha,k} = \frac{k}{n} \frac{1}{t}$ for all α .

(3) We noticed that the optimized parameters of the VHA usually do not resemble an adiabatic path or show steady growth, rather they are more evenly distributed. Hence, we chose a set where $\theta_{\alpha,k} = \frac{1}{n} \frac{1}{t}$ for all α . This set represents a Trotter expansion with n steps for a time evolution for the duration $\tau = \frac{1}{t}$.

For all choices of initial parameters, after the optimization the final values were vastly different. This is why we concluded that for the larger systems we often get stuck in a local optimum. For this reason, we tried further sets of initial parameters in Table 5.3:

Firstly, we added initial parameters recreating an adiabatic evolution alike in above point (1), but for $\tau = \frac{1}{t}$. Secondly, we chose an even distribution, similar to point (3), but with $\theta_{\alpha,k} = \frac{r}{t}$ where we varied $r \in \{0.1, 0.2, \dots, 1.0\}$. We noticed that usually the magnitude of the final parameters were between zero and $\sim \frac{1}{t}$. These additional start parameters improved the data of Table 5.2 towards the results of Table 5.3, as we will see below.

Improved start parameters						
VHA, 3×2				VHA, 3×3		
$\overline{\mathcal{F}}_{\min}$ [%]				$\overline{\mathcal{F}}_{\min}$ [%]		
	99.90	99.50		99.90	99.50	
6	98.91	97.26		6	96.76	90.81
n 8	99.31	98.65	n	8	98.02	94.18
	10	99.52	98.91	10	98.91	92.55

Table 5.3: The final state fidelities in percent after reruns of the VHA for some values for $\overline{\mathcal{F}}_{\min}$ and n from Table 5.2, this time with improved sets of start parameters. One can see a significant enhancement of the final state fidelity for the new start parameters.

We realize that a deeper understanding how to deterministically find suitable initial parameters should be acquired. However, this is out of the scope of this work. We will see below that the tested parameter sets already helped to show the capabilities of the VHA, achieving remarkable results in the considered small systems.

5.6.2 Improved results

To substantiate our conclusion that the initial parameters have a great effect on the results, we performed the VHA for some values of $\overline{\mathcal{F}}_{\min} \leq 99.9\%$ and $n \geq 6$, exploring a larger set of start parameters, as states in Sec. 5.6.1. Table 5.3 displays the final state fidelity of the 3×2 and 3×3 systems for the optimized start parameters, showing a significant improvement of the final state fidelity over the results of Table 5.2. We emphasize that this was not because of a favorable set of random gate errors; once better start parameters were found the results are changing little with varying the gate errors.

To give more perspective on the scale of improvement, we can look at different measures for the quality of the final state other than the final state fidelity. While the fidelity is a commonly used measure, it is quite abstract.

Another way to quantify the performance of the VHA is to look at the value of the ground state energy. This is a quantity one might be particularly interested in when applying variational algorithms. For the 3×3 Hubbard model with $U = 2t > 0$ the exact value is $E_g = -9.67t$. For the chosen initial state the state fidelity is already 96.18%, but the expectation value of the Hamiltonian is only $\langle \psi_0 | H | \psi_0 \rangle = -9.29t$. After 10 steps of the VHA for a gate fidelity of 99.90% the final state fidelity has improved close to 99%, and the expectation value of the Hamiltonian reaches $\langle \psi_f | H | \psi_f \rangle = -9.60t$.

5.7 Chapter conclusion

In this chapter we studied in detail the quantum simulation of relatively small lattice Hubbard models with a specific type of gate errors, but our analysis still allows drawing several conclusions:

- (1) The variational Hamiltonian ansatz (VHA) produces the ground state wave function of the Hubbard model in good approximation with a number of steps which is much

lower than the number of Trotter steps needed in an adiabatic approach.

(2) The effects of (static) gate errors are strongly mitigated by the variational methods.

(3) For the considered system size gate fidelities of the order of 99.9%, which should be within reach for state-of-the-art digital quantum computers, allow preparation of the ground state with a final state fidelity above 99%.

(4) This performance can be reached with a low number of variational parameters per step (5 in our case for the 2D Hubbard model).

It is clear that introducing more variational parameters, up to one parameter per gate, would enhance the variational error suppression of quasi-static errors. Eventually it leads to approaches like the variational quantum eigensolver [51]. However, introducing more parameters poses a challenge to the classical optimization routines. We found that even for our small set of parameters, the emerging optimization problem poses a substantial obstacle, since with growing system size the gradients with respect to the variation of the parameters decrease [122]. The difficulties with the optimization algorithms appear a stronger limitation of the performance of variational algorithms than a limited set variational parameters.

Better optimization algorithms could help with further issues. One could consider non-static portions of gate errors and statistical measurement errors. Such fluctuating errors are difficult to manage for optimizers, particularly for gradient based optimization protocols. We also noted the need for a good choice of the initial set of variational parameters as well as of the initial state. The latter could be obtained, e.g., from mean field theory. Finally more advanced quantum gate sequences implementing the terms of the Hamiltonian can lower the gate count and reduce the impact of gate errors. We applied up to 810 two-qubit gates in our examples of rather small systems. Algorithms with superior scaling behavior for Hubbard models [113, 123] should be considered to improve the performance of the VHA for larger systems.

Overall, however, we obtained a rather promising outcome regarding useful applications of variational algorithms on near-future quantum hardware. Our analysis showed good performance of the VHA through efficient use of few resources (in terms of gate count) and great error mitigation capabilities. With the room for improvement considering gate fidelities, classical optimization algorithms and choice of start parameters, the variational Hamiltonian ansatz might soon be able to produce exciting results in experiments.

Chapter 6

Summary and outlook

In this thesis we studied analog and digital quantum simulations of fermionic systems. The work was motivated by the vast improvements of quantum hardware – in particular superconducting qubits – which allow for such simulations. We investigated the perspectives of applications of near-future quantum devices, which do not possess means for full quantum error correction. Specifically, we considered in detail three topics:

- Analog quantum simulation with superconducting circuits
- The effects of specific gate errors on digital quantum simulation
- The performance of variational quantum algorithms under the influence of such gate errors

In Chap. 3 we studied a particular setup for performing analog quantum simulation of fermionic systems. Currently, the leading technology for such emulations are ultra-cold fermionic gases [16–18]. However, these simulators are facing two major challenges. On the one hand, they are difficult to scale up much further. On the other hand, the strength of the particles’ interactions is weak in comparison to (or at most of the order of) the finite temperatures of the gas [16, 49]. Hence, large-scale simulations or simulation of low-temperature physics are difficult to conduct.

We explored possibilities for analog quantum simulation of fermionic systems with superconducting qubits: A double chain of qubits with XX and ZZ couplings of neighboring qubits along and between the chains, respectively, can be mapped via the Jordan-Wigner transformation on a spin-full 1D Fermi-Hubbard model. The qubit system can thus be used to emulate the quantum properties of this model. Chap. 3 established the relations between the parameters of the fermionic system and the qubit system, and presented two superconducting circuits as possible realizations.

The conceptually simpler realization is based on Josephson charge qubits. It offers a broad parameter range and high flexibility. Unfortunately, charge qubits are very susceptible to charge noise, which makes them difficult to handle in experiment. A

superconducting qubit design that is less sensitive to charge fluctuation is the transmon qubit. For this reason it is widely used nowadays. We discussed in detail an emulator realization based on tunable transmon qubits. Here, the ZZ interaction arises due to an inductive coupling and the XX interaction due to a capacitive interaction. This appears a promising approach as far as the experimental realization is concerned, when transmons with relatively large geometric inductance are considered. An example of such a transmon design is given in Appx. A.4.

The transmon realization has the downside of a restricted parameter range, specifically considering the chemical potential. Equilibrium simulations can only be performed at very low filling, unlike with the charge qubit realization where, e.g., also half-filling could be achieved. Still, we proposed several interesting scenarios to be explored in a transmon based analog quantum simulation, including protocols which help gaining confidence in the results of the emulation through measurements of local operators.

Chap. 4 was devoted to the analysis of digital quantum simulation. Specifically, we studied the effects of gate errors occurring during a digital quantum simulation of the time evolution of a quantum system with Hamiltonian H using algorithms based on the Trotter expansion. The gate errors were modeled as over-rotations. We showed that such errors effectively introduce an extra term $\delta H(t)$ in the Hamiltonian, which in many cases can be interpreted as a time-dependent disorder term. However, the nature of these contributions depend on the choice of the algorithms, i.e., different algorithms may introduce different physics in a faulty simulation.

As an explicit example we considered a Fermi-Hubbard model with spin-flip interaction. We applied our method to algorithms based on various two-qubit gates. The examples demonstrate explicitly how the effects of over-rotations depend on the choice of algorithms. For instance in the example of Sec. 4.2.2 we showed that replacing CZ gates by a chain of CNOTs introduces unphysical multi-particle interactions violating particle conservation.

The findings were substantiated by a numerical analysis of a small model system. However, the method can be extended beyond small systems, since larger algorithms can be analyzed piecewise. Particularly, the results of Sec. 4.2.2 are valid for a large class of Hubbard-like Hamiltonians with general hopping terms $t_{jk}c_j^\dagger c_k$ and density-density interactions $V_{jk}c_j^\dagger c_j c_k^\dagger c_k$. This covers a wide variety of problems in quantum chemistry and solid state physics.

Another important result of Chap. 4 is the relation between gate errors due to over-rotations and gate fidelities. This enables us to quantify the strength of the disorder in the effective Hamiltonian for a given fidelity and Trotter step size. Unfortunately, we find that fidelities as presently achieved in experiments impose severe limitations on useful applications. According to the estimate of Eq. (4.42), gate fidelities of 99% only allow for approximately 10 gates to run in an algorithm. To allow for 100 gates, fidelities should improve towards 99.99%. However, we presented a worst case estimate, which assumes errors of individual gate add up adversely. Effectively, the maximum gate count

could be larger. On the other hand, we assumed over-rotations to be the only source of gate errors. Other error types that lower the measured gate fidelities might lead to different scaling behavior.

Still, the estimate indicates that in order to utilize digital quantum simulation in the near future, we need to focus on algorithms with a relatively low gate count. Prime candidates in this respect are variational algorithms. They show remarkable performance regarding applications with low gate count, and are believed to mitigate errors [51, 52].

Chap. 5 then explicitly tested the capabilities of variational algorithms under the influence of gate errors, with the error model introduced in the preceding chapter. Specifically, the variational Hamiltonian ansatz (VHA) was studied as a tool to prepare the ground state of Fermi-Hubbard models. The algorithm was fully simulated on a classical computer for two-dimensional models with up to 3×3 sites (represented by 18 qubits), which is numerically demanding.

We found that the VHA produces the ground state of the Hubbard model in good approximation with a number of steps which is much lower than the number of Trotter steps needed in an adiabatic approach. Moreover, the variational algorithm suppresses (static) gate errors, making it even more superior over the adiabatic approach.

We showed that – for the considered system sizes – gate fidelities of about 99.9% allow for the preparation of the ground state with a final state fidelity above 99%. Such gate fidelities are within reach for state-of-the-art quantum hardware.

The performance of the VHA can be reached despite a low number of variational parameters per step (five in our case). It is clear how more variational parameters, up to one parameter per gate, would increase the performance, especially with respect to variational error suppression. This would be a similar approach to the variational quantum eigensolver [51]. However, the optimization of these parameters (using a classical computer) will quickly become tedious. We found that optimizing even our small set of parameters poses a substantial obstacle to overcome. It appears that using a small set of parameters is in fact more promising to achieve good overall performance.

In terms of an outlook for future research there is variety of aspects that should be mentioned:

Regarding analog quantum simulation with superconducting circuits, one can explore further qubit designs such as, e.g., the phase slip qubit [87–90], and consider additional systems to emulate [7]. However, the options for fermionic systems which are feasible to simulate seem limited because of the necessary mapping onto qubits. After a mapping using, e.g., the Jordan-Wigner transformation, one may end with a qubit system with complicated multi-qubit interactions that are unfeasible to implement on the hardware level.

An interesting approach would be to combine analog and digital quantum simulation. Parts of the simulated Hamiltonian could be solved through analog simulations (with reduced complexity), which could serve as large gates of an algorithm [119]. In this way

gate counts of digital simulations could be lowered substantially.

In terms of digital quantum simulation further sources of gate errors should be taken into account. If the reduced experimental gate fidelities are not solely caused by over-rotations, the estimate for the maximum feasible gate count could improve drastically. Considering, e.g., decoherence as error source, parallelization should allow for much higher overall gate count of algorithms.

Furthermore, the disorder arising from faulty gates in principle could correspond to disorder in natural systems which one might want to simulate.

With respect to variational algorithms we identified certain aspects with potential for improvement. The final state fidelity depends strongly on the initial guess for the variational parameters and methods for choosing suitable start parameters need to be developed. Also we only used non-interacting initial states. Other states that are easy to prepare (obtained, e.g., from Hartree-Fock solutions) should be considered, which should improve the performance, as these states are already closer to the final state than the non-interacting ground state. Finally, more sophisticated classical optimization routines need to be used.

Overall, however, we found that our results concerning variational algorithms look quite promising for near-future applications. If quantum hardware continues to improve at a steady rate we could see meaningful utilization of quantum simulators in already a few years – even though the scope of such utilization will probably remain limited for a while.

Since the first ideas in the early 80's, the prospect of multi-purpose quantum simulation and quantum computing has stimulated an ever-growing field of research. With the recent progress, it will be exciting to see if near-future quantum simulators will achieve an advantage over their classical counterparts, and how much of an advantage that becomes. We will see how this will affect further development, and how our means for computation will change in the coming decades.

Appendix

Appendix A

Transmon circuit calculations

This Appendix is based on the the publication

[1] J.-M. Reiner, M. Marthaler, J. Braumüller, M. Weides, and G. Schön, *Emulating the one-dimensional Fermi-Hubbard model by a double chain of qubits*, Phys. Rev. A **94**, 032338 (2016).

Reprinting of copyrighted material from this publication is explicitly permitted within this thesis by the American Physical Society (APS).

A.1 Tunable transmon

In order to demonstrate the ZZ and XX couplings between two transmons in the circuit shown in Fig. A.1, we expound our model of tunable transmon qubits. The transmon consists of a loop of two Josephson junctions J with critical current I_c . The loop has an intrinsic geometric inductance L , with an external magnetic flux Φ_e passing through the loop. A large capacitance C is shunted to each junction. The phases across the left and right junctions are denoted ϕ_l and ϕ_r , and we introduce the external phase $\phi_e = \frac{2e}{\hbar}\Phi_e$. We can derive the Hamiltonian by employing the methods explained in Sec. 2.2.1. Using the addition theorem for the cosine potentials and defining $\phi = \frac{1}{2}(\phi_l + \phi_r)$, and $\phi_- = \frac{1}{2}(\phi_l - \phi_r)$ the Hamiltonian of the circuit reads

$$H_T = 2E_C(N^2 + N_-^2) - 2E_J \cos(\phi) \cos(\phi_-) + \frac{E_L}{2}(\phi_- - \frac{\phi_e}{2})^2, \quad (\text{A.1})$$

where we introduced the canonical charge number operators N and N_- , as well as the energies $E_C = \frac{e^2}{2C}$, $E_J = \frac{\hbar}{2e}I_c$, and $E_L = \frac{\hbar^2}{e^2 L}$.

The geometric inductance L is very small, leading to $E_L \gg E_J$. Hence, we can neglect excitations of the degree of freedom associated with ϕ_- . We fix ϕ_- at the minimum of its steep potential, resulting in the effective transmon Hamiltonian

$$H_{T,\text{eff}} = 2E_C N^2 - 2E_J \cos(\frac{\phi_e}{2}) \cos(\phi). \quad (\text{A.2})$$

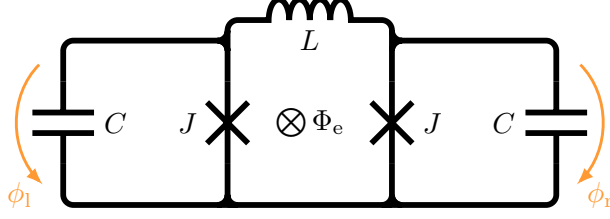


Figure A.1: Circuit diagram of a tunable transmon with Josephson junctions J , the capacitances C in parallel, and the intrinsic inductance L of the loop. The phase differences across the junctions (and capacitances) are labeled ϕ_l and ϕ_r , Φ_e denotes an external flux through the loop.

In the transmon limit, $E_J \gg E_C$, we can treat this as an anharmonic oscillator. For the lowest-lying states we can expand the cosine up to fourth order and obtain a Duffing oscillator

$$H_{T,\text{eff}} = \epsilon(a^\dagger a + \frac{1}{2}) - 2E_J \cos(\frac{\phi_e}{2}) - \frac{E_C}{24}(a^\dagger - a)^4 \quad (\text{A.3})$$

with $\epsilon = \sqrt{8E_C E_J \cos(\phi_e/2)}$, and

$$\phi = -i \frac{1}{\sqrt{2}} \left(\frac{2E_C}{E_J \cos(\frac{\phi_e}{2})} \right)^{\frac{1}{4}} (a^\dagger - a), \quad (\text{A.4})$$

$$N = \frac{1}{\sqrt{2}} \left(\frac{E_J \cos(\frac{\phi_e}{2})}{2E_C} \right)^{\frac{1}{4}} (a^\dagger + a). \quad (\text{A.5})$$

A projection on the first two states casts the operators into the qubit basis, which yields (up to a constant contribution)

$$H_{T,\text{eff}} = \frac{1}{2} \epsilon \sigma^z, \quad (\text{A.6})$$

with

$$\phi = \frac{1}{\sqrt{2}} \left(\frac{2E_C}{E_J \cos(\frac{\phi_e}{2})} \right)^{\frac{1}{4}} \sigma^y, \quad (\text{A.7})$$

$$N = \frac{1}{\sqrt{2}} \left(\frac{E_J \cos(\frac{\phi_e}{2})}{2E_C} \right)^{\frac{1}{4}} \sigma^x, \quad (\text{A.8})$$

$$\begin{aligned} \cos(\phi) &\approx 1 - \frac{\phi^2}{2} \\ &= \left(1 - \frac{1}{2} \sqrt{\frac{2E_C}{E_J \cos(\frac{\phi_e}{2})}} \right) \mathbb{1} - \frac{1}{4} \sqrt{\frac{2E_C}{E_J \cos(\frac{\phi_e}{2})}} \sigma^z. \end{aligned} \quad (\text{A.9})$$

A.2 ZZ coupling

To achieve a ZZ coupling between two transmons, we make use of the previously ignored degree of freedom associated with ϕ_- in Eq. (A.1). It couples to the cosine potential of

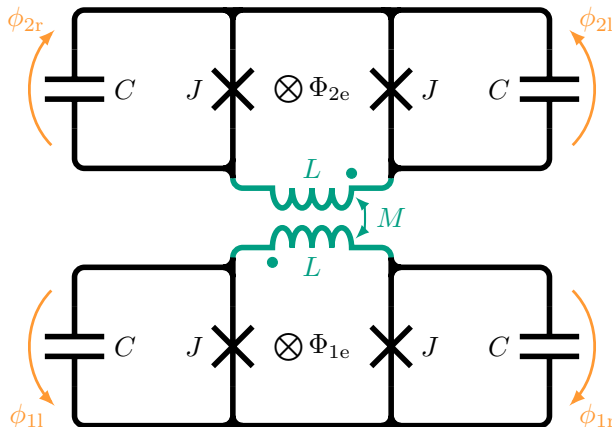


Figure A.2: Circuit diagram of two inductively coupled transmons, where their inductances L form a mutual inductance $M = k_M L$ with $k_M \in (0, 1)$. The transmons should be built identically with Josephson junctions J and shunt capacities C , but with individually controlled external fluxes Φ_{1e} and Φ_{2e} for tuning. $\phi_{(1,2)l}$ and $\phi_{(1,2)r}$ denote the phase differences across the junctions (and capacitances).

the qubit states, thus to σ^z (see Eq. (A.9)). By coupling the loop inductances of two transmons to form a mutual inductance M , the ϕ_- of each transmon interact with each other, mediating a ZZ interaction between the qubits.

For two inductances L coupled to form a mutual inductance M , we can express $M = k_M L$, with $k_M \in (0, 1)$ being a measure how close the inductances are coupled. We denote the currents through each inductance $I_{(1,2)}$, define the vector $\mathbf{I} = (I_1, I_2)$, and the matrix

$$\mathbf{L} = \begin{pmatrix} L & M \\ M & L \end{pmatrix}. \quad (\text{A.10})$$

For the magnetic fluxes through the inductances we write $\Phi_{(1,2)}$, and introduce $\Phi = (\Phi_1, \Phi_2)$. With $\Phi = \mathbf{L}\mathbf{I}$, the potential energy V_M of the mutual inductance reads

$$\begin{aligned} V_M &= \frac{1}{2} \mathbf{I}^T \mathbf{L} \mathbf{I} = \frac{1}{2} \Phi^T \mathbf{L}^{-1} \Phi \\ &= \frac{1}{1 - k_M^2} \frac{1}{2L} (\Phi_1 - \Phi_2)^2 + \frac{1}{1 + k_M} \frac{1}{L} \Phi_1 \Phi_2. \end{aligned} \quad (\text{A.11})$$

Now we will derive the ZZ interaction for the transmon from Appx. A.1. Consider two transmons coupled by their inductances L forming a mutual inductance $M = k_M L$ ($k_M \in (0, 1)$), with the phases across the junctions (and capacitances) of the two transmons being denoted $\phi_{(1,2)l}$ and $\phi_{(1,2)r}$ as shown in Fig. A.2. For the external magnetic fluxes $\Phi_{(1,2)e}$ we introduce the phases $\phi_{(1,2)e} = \frac{2e}{\hbar} \Phi_{(1,2)e}$. The Lagrangian of this setup

reads (using Eq. (A.11)):

$$\begin{aligned}
 \mathcal{L}^z &= \left(\frac{\hbar}{2e}\right)^2 \frac{1}{2} C(\dot{\phi}_{1l}^2 + \dot{\phi}_{1r}^2 + \dot{\phi}_{2l}^2 + \dot{\phi}_{2r}^2) \\
 &+ \frac{\hbar}{2e} I_c (\cos(\phi_{1l}) + \cos(\phi_{1r}) + \cos(\phi_{2l}) + \cos(\phi_{2r})) \\
 &- \left(\frac{\hbar}{2e}\right)^2 \frac{1}{2L} \left(\frac{1}{1-k_M^2} ((\phi_{1l} - \phi_{1r} - \phi_{1e}) - (\phi_{2l} - \phi_{2r} - \phi_{2e}))^2 \right. \\
 &\quad \left. + \frac{2}{1+k_M} (\phi_{1l} - \phi_{1r} - \phi_{1e})(\phi_{2l} - \phi_{2r} - \phi_{2e}) \right). \tag{A.12}
 \end{aligned}$$

Defining $\phi_{(1,2)} := \frac{1}{2}(\phi_{(1,2)l} + \phi_{(1,2)r})$ as well as $\phi_{\pm} := \frac{1}{2}((\frac{\phi_{1l} - \phi_{1r}}{2} - \frac{\phi_{1e}}{2}) \pm (\frac{\phi_{2l} - \phi_{2r}}{2} - \frac{\phi_{2e}}{2}))$, using that the external fields are constant, meaning $\dot{\phi}_{(1,2)e} = 0$, and using the addition theorem $\cos(\phi_{(1,2)l}) + \cos(\phi_{(1,2)r}) = 2 \cos(\frac{\phi_{(1,2)l} + \phi_{(1,2)r}}{2}) \cos(\frac{\phi_{(1,2)l} - \phi_{(1,2)r}}{2})$ for the cosine terms one can find the Hamiltonian

$$\begin{aligned}
 H^z &= 2E_C(N_1^2 + N_2^2 + \frac{1}{2}N_+^2 + \frac{1}{2}N_-^2) + \frac{1}{2}E_L\xi_+\phi_+^2 + \frac{1}{2}E_L\xi_-\phi_-^2 \\
 &- 2E_J \cos(\phi_1) \cos(\frac{\phi_{1e}}{2} + \phi_+ + \phi_-) \\
 &- 2E_J \cos(\phi_2) \cos(\frac{\phi_{2e}}{2} + \phi_+ - \phi_-), \tag{A.13}
 \end{aligned}$$

with the canonical charge numbers $N_{(1,2,\pm)}$, the energies E_C , E_J , and E_L as given in Appx. A.1, as well as $\xi_+ = \frac{2}{1+k_M}$ and $\xi_- = \frac{4}{1-k_M^2} - \frac{2}{1+k_M}$.

Recalling that L is very small, we find E_L to be very large (compared to E_J). We can therefore ignore terms proportional to $E_J\phi_{\pm}^2$ towards those proportional to $E_L\phi_{\pm}^2$, which justifies expanding the cosines for small ϕ_{\pm} yielding

$$\begin{aligned}
 H^z &= 2E_C(N_1^2 + N_2^2 + \frac{1}{2}N_+^2 + \frac{1}{2}N_-^2) + \frac{1}{2}E_L\xi_+\phi_+^2 + \frac{1}{2}E_L\xi_-\phi_-^2 \\
 &- 2E_J \cos(\phi_1) (\cos(\frac{\phi_{1e}}{2}) - \sin(\frac{\phi_{1e}}{2})(\phi_+ + \phi_-)) \\
 &- 2E_J \cos(\phi_2) (\cos(\frac{\phi_{2e}}{2}) - \sin(\frac{\phi_{2e}}{2})(\phi_+ - \phi_-)). \tag{A.14}
 \end{aligned}$$

We can identify the qubit energy terms $2E_C N_{(1,2)}^2 - 2E_J \cos(\frac{\phi_{(1,2)e}}{2}) \cos(\phi_{(1,2)}) = \frac{1}{2}\epsilon_{(1,2)}\sigma_{(1,2)}^z$, harmonic oscillators $E_C N_{\pm}^2 + \frac{1}{2}E_L\xi_{\pm}\phi_{\pm}^2 = \hbar\omega_{\pm}(a_{\pm}^{\dagger}a_{\pm} + \frac{1}{2})$, with $\omega_{\pm} = \frac{1}{\hbar}\sqrt{\xi_{\pm}2E_C E_L}$, and therefore $\phi_{\pm} = \frac{1}{\sqrt{2}}(\frac{2E_C}{\xi_{\pm}E_L})^{\frac{1}{4}}(a_{\pm}^{\dagger} + a_{\pm})$. We know that $\cos(\phi_{(1,2)})$ are diagonal in the qubit basis (see Eq. (A.9)), hence $\cos(\phi_{(1,2)}) = \alpha_{(1,2)}^z \sigma_{(1,2)}^z + \beta_{(1,2)} \mathbb{1}$. Following the above argument that ϕ_{\pm} is very small, we neglect terms proportional to $E_J \mathbb{1}\phi_{\pm} \approx 0$ and also leave out constant terms, resulting in

$$\begin{aligned}
 H^z &= \frac{1}{2}\epsilon_1\sigma_1^z + \frac{1}{2}\epsilon_2\sigma_2^z + \hbar\omega_+ a_+^{\dagger} a_+ + \hbar\omega_- a_-^{\dagger} a_- \\
 &+ (g_{1+}\sigma_1^z + g_{2+}\sigma_2^z)(a_+^{\dagger} + a_+) \\
 &+ (g_{1-}\sigma_1^z - g_{2-}\sigma_2^z)(a_-^{\dagger} + a_-), \tag{A.15}
 \end{aligned}$$

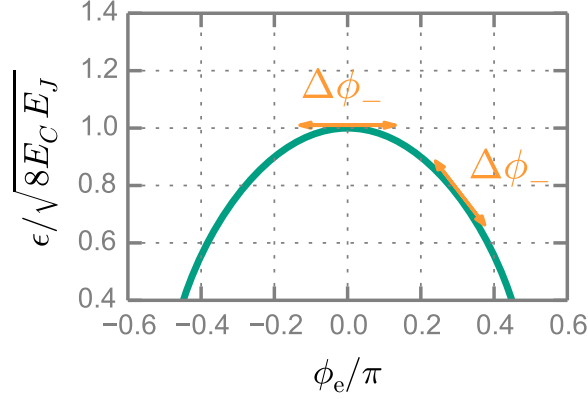


Figure A.3: The transmon's level splitting ϵ depends on the phase ϕ_e related to the external flux $\Phi_e = \frac{\hbar}{2e}\phi_e$. Fluctuations $\Delta\phi_-$ of the phase across the inductance of the transmon vary the energy splitting by an amount which depends on the slope of ϵ .

with $g_{(1,2)\pm} = 2E_J\alpha_{(1,2)}^z \sin(\frac{\phi_{(1,2)e}}{2}) \frac{1}{\sqrt{2}} (\frac{2E_C}{\xi_{\pm}E_L})^{\frac{1}{4}}$.

For the next step, we take the displacement operators $D_{\pm}(d) = e^{da_{\pm}^{\dagger} - d^{\dagger}a_{\pm}}$, and define the unitary operator

$$U = D_+(-\frac{g_{1+}\sigma_1^z + g_{2+}\sigma_2^z}{\hbar\omega_+})D_-(-\frac{g_{1-}\sigma_1^z - g_{2-}\sigma_2^z}{\hbar\omega_-}). \quad (\text{A.16})$$

By again neglecting constant terms, we transform the Hamiltonian to

$$U^{\dagger}H^zU = \frac{1}{2}\epsilon_1\sigma_1^z + \frac{1}{2}\epsilon_2\sigma_2^z + \hbar\omega_+a_+^{\dagger}a_+ + \hbar\omega_-a_-^{\dagger}a_- + g_z\sigma_1^z\sigma_2^z, \quad (\text{A.17})$$

with $g^z = -2(\frac{g_{1+}g_{2+}}{\hbar\omega_+} - \frac{g_{1-}g_{2-}}{\hbar\omega_-})$. Because of the small inductance of the transmons, the energy $\hbar\omega_{\pm}$ is very large compared to the qubit energies, thus, the oscillators' excitations can be ignored; however, they mediate an effective interaction between the qubits.

Finally, combining the findings of this section, the convenient identity $(\frac{1}{\xi_+} - \frac{1}{\xi_-}) = k_M$, and the results from Appx. A.1 one can check that for our effective Hamiltonian

$$H_{\text{eff}}^z = \frac{1}{2}\epsilon_1\sigma_1^z + \frac{1}{2}\epsilon_2\sigma_2^z + g_z\sigma_1^z\sigma_2^z, \quad (\text{A.18})$$

it holds that

$$g^z = -\frac{k_M}{16} \tan(\frac{\phi_{1e}}{2}) \tan(\frac{\phi_{2e}}{2}) \frac{\epsilon_1\epsilon_2}{E_L}. \quad (\text{A.19})$$

The coupling strength is tunable through the external phases $\phi_{(1,2)e}$, including the possibility of a sign change. This results from the fact, that the interaction is mediated through displacements of the coupled phases $\phi_{(1,2)-}$. In a transmon, the extent to which

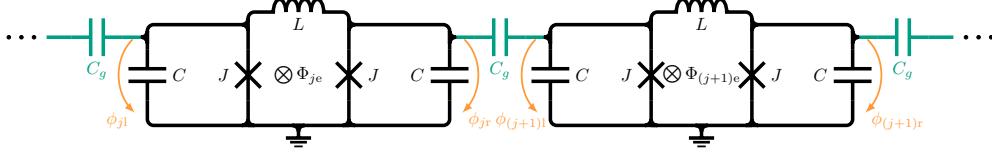


Figure A.4: Circuit diagram of a chain of coupled identical transmons, with Josephson junctions J (with critical current I_c), shunt capacitances C , and loop inductance L . They are individually tunable through external fluxes Φ_{je} , and the phase differences across the junctions (and capacitances) of the j^{th} qubit are denoted ϕ_{jl} and ϕ_{jr} . The transmons are coupled by capacitances C^x between neighboring transmons.

a displacement of ϕ_- affects ϵ depends on the external flux (as illustrated in Fig. A.3). Hence, the coupling strength is affected by the value of the external fluxes.

A.3 XX coupling

In a transmon the charge operator is proportional to σ^x (see Eq. (A.8)). We therefore suggest coupling the n identical tunable transmons through capacitances C^x as depicted in Fig. A.4. This way, an XX coupling should arise.

The phase differences across the junctions (and capacitances) of the j^{th} qubit are denoted ϕ_{jl} and ϕ_{jr} , and the external flux through the qubits are given by $\Phi_{je} = \frac{\hbar}{2e}\phi_{je}$. Introducing $\phi_j = \frac{1}{2}(\phi_{jl} + \phi_{jr})$, and $\phi_{j-} = \frac{1}{2}(\phi_{jl} - \phi_{jr})$ yields the Lagrangian

$$\begin{aligned} \mathcal{L}^x = & \sum_{j=1}^n \left(\left(\frac{\hbar}{2e} \right)^2 C (\dot{\phi}_j^2 + \dot{\phi}_{j-}^2) + \frac{\hbar}{e} I_c \cos(\phi_{j-}) \cos(\phi_j) - \left(\frac{\hbar}{2e} \right)^2 \frac{2}{L} (\phi_{j-} - \frac{\phi_{je}}{2})^2 \right) \\ & + \sum_{j=1}^{n-1} \left(\frac{\hbar}{2e} \right)^2 \frac{1}{2} C^x ((\dot{\phi}_j - \dot{\phi}_{j-}) - (\dot{\phi}_{(j+1)} + \dot{\phi}_{(j+1)-}))^2. \end{aligned} \quad (\text{A.20})$$

Regarding Appx. A.1, we already fix $\phi_{j-} = \phi_{je}/2$, $\dot{\phi}_{j-} = 0$ due to the steep potential created by the small value of L and, thus, find

$$\begin{aligned} \mathcal{L}^x = & \sum_{j=1}^n \left(\left(\frac{\hbar}{2e} \right)^2 (C + C^x) \dot{\phi}_j^2 + \frac{\hbar}{e} I_c \cos\left(\frac{\phi_{je}}{2}\right) \cos(\phi_j) \right) \\ & - \sum_{j=1}^{n-1} \left(\frac{\hbar}{2e} \right)^2 C^x \dot{\phi}_j \dot{\phi}_{j+1} - \left(\frac{\hbar}{2e} \right)^2 \frac{1}{2} C^x (\dot{\phi}_1^2 + \dot{\phi}_n^2). \end{aligned} \quad (\text{A.21})$$

We denote $\tilde{C} = C + C^x$ and $\lambda = \frac{C^x}{2\tilde{C}} \in (0, \frac{1}{2})$, also the tridiagonal $n \times n$ matrix

$$\mathbf{A}_\lambda = \begin{pmatrix} 1 & \lambda & 0 & \cdots \\ \lambda & 1 & \lambda & \cdots \\ 0 & \lambda & 1 & \cdots \\ \vdots & \vdots & \vdots & \ddots \end{pmatrix}, \quad (\text{A.22})$$

with ones on the diagonal and λ on the off-diagonals. Denoting the vector $\phi = (\phi_1, \dots, \phi_n)$ allows us to rewrite the Lagrangian as

$$\mathcal{L}^x = \left(\frac{\hbar}{2e}\right)^2 \tilde{C} \dot{\phi}^T \mathbf{A}_\lambda \dot{\phi} + \sum_{j=1}^n \frac{\hbar}{e} I_c \cos\left(\frac{\phi_{je}}{2}\right) \cos(\phi_j), \quad (\text{A.23})$$

where we neglected the boundary term $\frac{1}{2}C^x(\dot{\phi}_1^2 + \dot{\phi}_n^2)$. This is justified, as we will focus on the limit of small coupling, i.e., $C^x \ll C$. This limit is needed to apply the rotating wave approximation, as discussed in the main text.

It holds that $|\lambda| < \frac{1}{2}$ and one can show that in this case the matrix \mathbf{A}_λ is invertible with $\mathbf{A}_\lambda^{-1} = \mathbf{A}_{-\lambda} + \mathcal{O}(\lambda^2)$. In the limit of weak coupling, we can neglect terms of order $\mathcal{O}(\lambda^2)$, which allows us to easily transform the Lagrangian to the Hamiltonian

$$\begin{aligned} H^x &= 2E_{\tilde{C}} \mathbf{N}^T \mathbf{A}_{-\lambda} \mathbf{N} - \sum_{j=1}^n 2E_J \cos\left(\frac{\phi_{je}}{2}\right) \cos(\phi_j) \\ &= \sum_{j=1}^n (2E_{\tilde{C}} N_j^2 - 2E_J \cos\left(\frac{\phi_{je}}{2}\right) \cos(\phi_j)) + \sum_{j=1}^{n-1} 4E_{\tilde{C}} \lambda N_j N_{j+1}. \end{aligned} \quad (\text{A.24})$$

We can identify the qubit energies $\tilde{\epsilon}_j = \sqrt{8E_{\tilde{C}} E_J \cos(\phi_{je}/2)}$ with the findings of Appx. A.1, and use Eq. (A.8) to obtain $N_j = \alpha_j^x \sigma_j^x$ with $\alpha_j^x = \frac{1}{\sqrt{2}} \left(\frac{E_J \cos(\phi_{je}/2)}{2E_{\tilde{C}}}\right)^{\frac{1}{4}}$. This yields

$$H^x = \sum_{j=1}^n \frac{1}{2} \tilde{\epsilon}_j \sigma_j^z + \sum_{j=1}^{n-1} g_j^x \sigma_j^x \sigma_{j+1}^x, \quad (\text{A.25})$$

where $g_j^x = 2E_{\tilde{C}} \lambda \alpha_j^x \alpha_{j+1}^x = \frac{1}{2} \lambda \sqrt{\tilde{\epsilon}_j \tilde{\epsilon}_{j+1}}$.

For weak coupling we neglect the small change in the capacitive energy, especially since the transmons are tunable. Hence, we drop the tilde in the notation. Furthermore, we assume that the qubits are degenerate with respect to the energy ϵ . The second order terms, $\mathcal{O}\left(\left(\frac{C^x}{C}\right)^2\right)$, will also be dropped, yielding $\lambda = \frac{C^x}{2C}$. We thus obtain

$$H^x = \sum_{j=1}^n \frac{1}{2} \epsilon \sigma_j^z + g^x \sum_{j=1}^{n-1} \sigma_j^x \sigma_{j+1}^x, \quad (\text{A.26})$$

with

$$g^x = \frac{1}{4} \frac{C^x}{C} \epsilon. \quad (\text{A.27})$$

A.4 Experimental realization

We explore the concentric transmon qubit [91] as a potential candidate for the unit cell of the circuit diagram depicted in Fig. 3.3. It features a central disk island and a concentrically surrounding ring, constituting the shunt capacitance C of the transmon. The

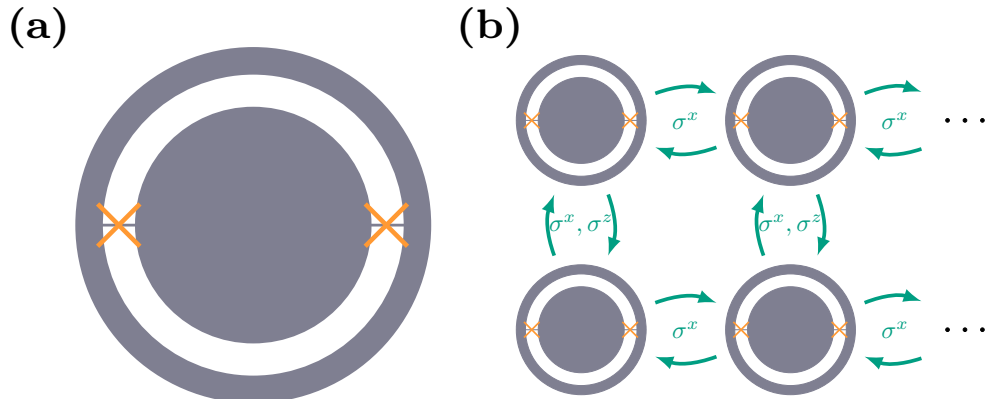


Figure A.5: **(a)** Schematic of the concentric transmon qubit: It consists of a large central disk electrode ($230\ \mu\text{m}$ diameter) surrounded by a ring electrode, constituting the shunt capacitance for the two Josephson junctions (orange) interconnecting the electrodes. **(b)** Possible implementation of the simulator scheme depicted in Fig. 3.1 with concentric transmon qubits. In the vertical direction, the magnetic ZZ coupling, mediated by a non-vanishing mutual inductance M , is relevant. The XX coupling can effectively be suppressed by detuning vertically adjacent qubits. Transverse coupling is dominant in horizontal direction, where the ZZ coupling is suppressed by exploiting the asymmetric gradiometry of the qubits.

two qubit electrodes are interconnected by two Josephson junctions (see Fig. A.5(a)). The formed gradiometric SQUID allows for a fast tuning of the qubit frequency by a magnetic field gradient provided by an on-chip flux line.

The geometric inductance of the large ring electrode, with $\sim 340\ \mu\text{m}$ diameter, provides a considerable magnetic dipole moment. Thereby, placing two devices near to each other results in a considerable mutual inductance between the devices, that allows for an inductive ZZ coupling to adjacent devices, as explained above in Appx. A.2 and in Sec 3.2. By exploiting its rotational asymmetry with respect to the location of Josephson junctions, the concentric transmon architecture furthermore promises to satisfy the proposed simulator scheme since it allows for a site-selective engineering of the ZZ coupling. The XX coupling merely relies on the geometric dimensions of the qubit electrodes and is in first order isotropic. For two adjacent concentric transmons, a capacitance is formed between the large rings and disks of the two qubits, which yields the desired XX interaction, as derived in Appx. A.3. A proposal for the simulator scheme reproduced with concentric transmon qubits is schematically depicted in Fig. A.5(b). Using this scheme, we obtain – additional to a ZZ coupling – also an XX coupling between two transmons of the same rung of the qubit ladder, which is not part of the proposed design in Fig. 3.1. This effective dispersive coupling may be suppressed by a mutual frequency detuning.

Estimates indicate a small ratio M/L between mutual and geometric inductance M and L , respectively, resulting in a ZZ coupling strength close to measured dephasing rates for the device. We are investigating design adaptations to increase the mutual inductance as well as the overall geometric inductance of the qubit circuit. One possible

route to achieve this could be an interlocking, i.e., overlapping, of the ring electrodes of adjacent concentric transmons, leading to an increase in the mutual inductance while suppressing the capacitive coupling due to proximity to the central island. The concentric transmon may be considered as a viable starting point to further explore geometries with longitudinal ZZ coupling eventually increased to an adequate strength.

Bibliography

- [1] J.-M. Reiner, M. Marthaler, J. Braumüller, M. Weides, and G. Schön, *Emulating the one-dimensional Fermi-Hubbard model by a double chain of qubits*, Phys. Rev. A **94**, 032338 (2016).
- [2] J.-M. Reiner, S. Zanker, I. Schwenk, J. Leppäkangas, F. Wilhelm-Mauch, G. Schön, and M. Marthaler, *Effects of gate errors in digital quantum simulations of fermionic systems*, Quantum Sci. Technol. **3**, 045008 (2018).
- [3] J.-M. Reiner, F. Wilhelm-Mauch, G. Schön, and M. Marthaler, *Finding the ground state of the Hubbard model by variational methods on a quantum computer with gate errors*, Quantum Sci. Technol. **4**, 035005 (2019).
- [4] P. Macha, G. Oelsner, J.-M. Reiner, M. Marthaler, S. André, G. Schön, U. Hübner, H.-G. Meyer, E. Il'ichev, and A. V. Ustinov, *Implementation of a quantum metamaterial using superconducting qubits*, Nat. Commun. **5**, 5146 (2014).
- [5] I. Schwenk, S. Zanker, J.-M. Reiner, J. Leppäkangas, and M. Marthaler, *Estimating the Error of an Analog Quantum Simulator by Additional Measurements*, Phys. Rev. Lett. **119**, 240502 (2017).
- [6] I. Schwenk, J.-M. Reiner, S. Zanker, L. Tian, J. Leppäkangas, and M. Marthaler, *Reconstructing the ideal results of a perturbed analog quantum simulator*, Phys. Rev. A **97**, 042310 (2018).
- [7] J. Leppäkangas, J. Braumüller, M. Hauck, J.-M. Reiner, I. Schwenk, S. Zanker, L. Fritz, A. V. Ustinov, M. Weides, and M. Marthaler, *Quantum simulation of the spin-boson model with a microwave circuit*, Phys. Rev. A **97**, 052321 (2018).
- [8] S. Zanker, I. Schwenk, J.-M. Reiner, J. Leppäkangas, and M. Marthaler, *Analyzing the spectral density of a perturbed analog quantum simulator using the Keldysh formalism*, Phys. Rev. B **97**, 214301 (2018).
- [9] A. C. Moule, *The Chinese South-Pointing Carriage*, T'oung Pao **23**, 83–98 (1924).
- [10] D. d. S. Price, *Gears from the Greeks. The Antikythera Mechanism: A Calendar Computer from ca. 80 B. C.* Transactions of the American Philosophical Society **64**, 1–70 (1974).
- [11] J. S. Small, *The Analogue Alternative: The Electronic Analogue Computer in Britain and the USA, 1930-1975* (Psychology Press, 2001).
- [12] *TOP500 List - November 2018 | TOP500 Supercomputer Sites*, <https://www.top500.org/list/2018/11/> (2018), accessed November 2018.
- [13] G. E. Moore, *Cramming more components onto integrated circuits*, Reprinted from *Electronics*, volume 38, number 8, April 19, 1965, pp.114 ff. IEEE Solid-State Circuits Society Newsletter **11**, 33–35 (2006).
- [14] M. Head-Gordon and E. Artacho, *Chemistry on the computer*, Physics Today **61**, 58–63 (2008).

-
- [15] R. P. Feynman, *Simulating physics with computers*, Int J Theor Phys **21**, 467–488 (1982).
- [16] A. Mazurenko, C. S. Chiu, G. Ji, M. F. Parsons, M. Kanász-Nagy, R. Schmidt, F. Grusdt, E. Demler, D. Greif, and M. Greiner, *A cold-atom Fermi–Hubbard antiferromagnet*, Nature **545**, 462–466 (2017).
- [17] I. Bloch, J. Dalibard, and S. Nascimbène, *Quantum simulations with ultracold quantum gases*, Nat. Phys. **8**, 267–276 (2012).
- [18] A. N. Wenz, G. Zürn, S. Murmann, I. Brouzos, T. Lompe, and S. Jochim, *From Few to Many: Observing the Formation of a Fermi Sea One Atom at a Time*, Science **342**, 457–460 (2013).
- [19] E. Zohar, J. I. Cirac, and B. Reznik, *Quantum simulations of gauge theories with ultracold atoms: Local gauge invariance from angular-momentum conservation*, Phys. Rev. A **88**, 023617 (2013).
- [20] D. Porras and J. I. Cirac, *Effective Quantum Spin Systems with Trapped Ions*, Phys. Rev. Lett. **92**, 207901 (2004).
- [21] A. Friedenauer, H. Schmitz, J. T. Glueckert, D. Porras, and T. Schaetz, *Simulating a quantum magnet with trapped ions*, Nat. Phys. **4**, 757–761 (2008).
- [22] R. Blatt and C. F. Roos, *Quantum simulations with trapped ions*, Nat. Phys. **8**, 277–284 (2012).
- [23] P. Benioff, *The computer as a physical system: A microscopic quantum mechanical Hamiltonian model of computers as represented by Turing machines*, J Stat Phys **22**, 563–591 (1980).
- [24] D. Deutsch, *Quantum Theory, the Church-Turing Principle and the Universal Quantum Computer*, Proc. R. Soc. A **400**, 97–117 (1985).
- [25] P. Shor, *Polynomial-Time Algorithms for Prime Factorization and Discrete Logarithms on a Quantum Computer*, SIAM J. Comput. **26**, 1484–1509 (1997).
- [26] L. M. K. Vandersypen, M. Steffen, G. Breyta, C. S. Yannoni, M. H. Sherwood, and I. L. Chuang, *Experimental realization of Shor’s quantum factoring algorithm using nuclear magnetic resonance*, Nature **414**, 883–887 (2001).
- [27] L. K. Grover, *A Fast Quantum Mechanical Algorithm for Database Search*, in *Proceedings of the Twenty-eighth Annual ACM Symposium on Theory of Computing*, STOC ’96 (ACM, New York, NY, USA, 1996) pp. 212–219.
- [28] A. W. Harrow, A. Hassidim, and S. Lloyd, *Quantum Algorithm for Linear Systems of Equations*, Phys. Rev. Lett. **103**, 150502 (2009).
- [29] D. S. Abrams and S. Lloyd, *Simulation of Many-Body Fermi Systems on a Universal Quantum Computer*, Phys. Rev. Lett. **79**, 2586–2589 (1997).
- [30] D. S. Abrams and S. Lloyd, *Quantum Algorithm Providing Exponential Speed Increase for Finding Eigenvalues and Eigenvectors*, Phys. Rev. Lett. **83**, 5162–5165 (1999).
- [31] C. Monroe, D. M. Meekhof, B. E. King, W. M. Itano, and D. J. Wineland, *Demonstration of a Fundamental Quantum Logic Gate*, Phys. Rev. Lett. **75**, 4714–4717 (1995).
- [32] N. Akerman, N. Navon, S. Kotler, Y. Glickman, and R. Ozeri, *Universal gate-set for trapped-ion qubits using a narrow linewidth diode laser*, New J. Phys. **17**, 113060 (2015).
- [33] T. F. Watson, S. G. J. Philips, E. Kawakami, D. R. Ward, P. Scarlino, M. Veldhorst, D. E. Savage, M. G. Lagally, M. Friesen, S. N. Coppersmith, M. A. Eriksson, and L. M. K. Vandersypen, *A programmable two-qubit quantum processor in silicon*, Nature **555**, 633–637 (2018).
-

BIBLIOGRAPHY

- [34] R. Barends, J. Kelly, A. Megrant, A. Veitia, D. Sank, E. Jeffrey, T. C. White, J. Mutus, A. G. Fowler, B. Campbell, Y. Chen, Z. Chen, B. Chiaro, A. Dunsworth, C. Neill, P. O'Malley, P. Roushan, A. Vainsencher, J. Wenner, A. N. Korotkov, A. N. Cleland, and J. M. Martinis, *Superconducting quantum circuits at the surface code threshold for fault tolerance*, Nature **508**, 500–503 (2014).
- [35] J. Kelly, R. Barends, A. G. Fowler, A. Megrant, E. Jeffrey, T. C. White, D. Sank, J. Y. Mutus, B. Campbell, Y. Chen, Z. Chen, B. Chiaro, A. Dunsworth, I.-C. Hoi, C. Neill, P. J. J. O'Malley, C. Quintana, P. Roushan, A. Vainsencher, J. Wenner, A. N. Cleland, and J. M. Martinis, *State preservation by repetitive error detection in a superconducting quantum circuit*, Nature **519**, 66–69 (2015).
- [36] J. M. Chow, J. M. Gambetta, A. D. Córcoles, S. T. Merkel, J. A. Smolin, C. Rigetti, S. Poletto, G. A. Keefe, M. B. Rothwell, J. R. Rozen, M. B. Ketchen, and M. Steffen, *Universal Quantum Gate Set Approaching Fault-Tolerant Thresholds with Superconducting Qubits*, Phys. Rev. Lett. **109**, 060501 (2012).
- [37] A. G. Fowler, M. Mariantoni, J. M. Martinis, and A. N. Cleland, *Surface codes: Towards practical large-scale quantum computation*, Phys. Rev. A **86**, 032324 (2012).
- [38] P. Schindler, J. T. Barreiro, T. Monz, V. Nebendahl, D. Nigg, M. Chwalla, M. Hennrich, and R. Blatt, *Experimental Repetitive Quantum Error Correction*, Science **332**, 1059–1061 (2011).
- [39] S. J. Devitt, W. J. Munro, and K. Nemoto, *Quantum error correction for beginners*, Rep. Prog. Phys. **76**, 076001 (2013).
- [40] B. Lekitsch, S. Weidt, A. G. Fowler, K. Mølmer, S. J. Devitt, C. Wunderlich, and W. K. Hensinger, *Blueprint for a microwave trapped ion quantum computer*, Sci. Adv. **3**, e1601540 (2017).
- [41] J. Preskill, *Quantum Computing in the NISQ era and beyond*, Quantum **2**, 79 (2018).
- [42] A. O. Niskanen, K. Harrabi, F. Yoshihara, Y. Nakamura, S. Lloyd, and J. S. Tsai, *Quantum Coherent Tunable Coupling of Superconducting Qubits*, Science **316**, 723–726 (2007).
- [43] Y. Wang, Y. Li, Z.-q. Yin, and B. Zeng, *16-qubit IBM universal quantum computer can be fully entangled*, npj Quantum Information **4**, 46 (2018).
- [44] S. S. Tannu and M. K. Qureshi, *A Case for Variability-Aware Policies for NISQ-Era Quantum Computers*, arXiv:1805.10224 (2018).
- [45] I. L. Markov, A. Fatima, S. V. Isakov, and S. Boixo, *Quantum Supremacy Is Both Closer and Farther than It Appears*, arXiv:1807.10749 (2018).
- [46] P. Jordan and E. Wigner, *Über das Paulische Äquivalenzverbot*, Zeitschrift für Physik **47**, 631–651 (1928).
- [47] H. F. Trotter, *On the product of semi-groups of operators*, Proc. Amer. Math. Soc. **10**, 545–551 (1959).
- [48] I. Buluta and F. Nori, *Quantum Simulators*, Science **326**, 108–111 (2009).
- [49] D. Mitra, P. T. Brown, E. Guardado-Sanchez, S. S. Kondov, T. Devakul, D. A. Huse, P. Schauf, and W. S. Bakr, *Quantum gas microscopy of an attractive Fermi–Hubbard system*, Nat. Phys. **14**, 173–177 (2018).
- [50] J. Koch, T. M. Yu, J. Gambetta, A. A. Houck, D. I. Schuster, J. Majer, A. Blais, M. H. Devoret, S. M. Girvin, and R. J. Schoelkopf, *Charge-insensitive qubit design derived from the Cooper pair box*, Phys. Rev. A **76**, 042319 (2007).

BIBLIOGRAPHY

- [51] J. R. McClean, J. Romero, R. Babbush, and A. Aspuru-Guzik, *The theory of variational hybrid quantum-classical algorithms*, New J. Phys. **18**, 023023 (2016).
- [52] D. Wecker, M. B. Hastings, and M. Troyer, *Progress towards practical quantum variational algorithms*, Phys. Rev. A **92**, 042303 (2015).
- [53] A. Kandala, A. Mezzacapo, K. Temme, M. Takita, M. Brink, J. M. Chow, and J. M. Gambetta, *Hardware-efficient variational quantum eigensolver for small molecules and quantum magnets*, Nature **549**, 242 (2017).
- [54] A. Kandala, K. Temme, A. D. Córcoles, A. Mezzacapo, J. M. Chow, and J. M. Gambetta, *Error mitigation extends the computational reach of a noisy quantum processor*, Nature **567**, 491 (2019).
- [55] S. B. Bravyi and A. Y. Kitaev, *Fermionic Quantum Computation*, Annals of Physics **298**, 210–226 (2002).
- [56] P. Hauke, F. M. Cucchietti, L. Tagliacozzo, I. Deutsch, and M. Lewenstein, *Can one trust quantum simulators?* Rep. Prog. Phys. **75**, 082401 (2012).
- [57] J. W. Britton, B. C. Sawyer, A. C. Keith, C.-C. J. Wang, J. K. Freericks, H. Uys, M. J. Biercuk, and J. J. Bollinger, *Engineered two-dimensional Ising interactions in a trapped-ion quantum simulator with hundreds of spins*, Nature **484**, 489–492 (2012).
- [58] M. H. Devoret, *Quantum Fluctuations in Electrical Circuits*, Fluctuations Quantiques/Quantum Fluctuations: Les Houches Session LXIII, 351 (1997).
- [59] G. Wendin and V. S. Shumeiko, *Superconducting Quantum Circuits, Qubits and Computing*, arXiv:cond-mat/0508729 (2005).
- [60] T. Toffoli, *Bicontinuous extensions of invertible combinatorial functions*, Math. Systems Theory **14**, 13–23 (1981).
- [61] D. E. Deutsch, *Quantum computational networks*, Proc. R. Soc. Lond. A **425**, 73–90 (1989).
- [62] A. W. Harrow, B. Recht, and I. L. Chuang, *Efficient Discrete Approximations of Quantum Gates*, Journal of Mathematical Physics **43**, 4445–4451 (2002).
- [63] M. A. Nielsen and I. L. Chuang, *Quantum Computation and Quantum Information: 10th Anniversary Edition* (Cambridge University Press, 2010).
- [64] A. Barenco, *A Universal Two-Bit Gate for Quantum Computation*, Proc. Royal Soc. Lond. A **449**, 679–683 (1995).
- [65] J.-L. Brylinski and R. Brylinski, *Universal quantum gates*, arXiv:quant-ph/0108062 (2001).
- [66] Y. Shi, *Both Toffoli and Controlled-NOT need little help to do universal quantum computation*, arXiv:quant-ph/0205115 (2002).
- [67] S. Lloyd, *Almost Any Quantum Logic Gate is Universal*, Phys. Rev. Lett. **75**, 346–349 (1995).
- [68] M. Suzuki, *Generalized Trotter’s formula and systematic approximants of exponential operators and inner derivations with applications to many-body problems*, Commun.Math. Phys. **51**, 183–190 (1976).
- [69] N. Hatano and M. Suzuki, *Finding Exponential Product Formulas of Higher Orders*, in *Quantum Annealing and Other Optimization Methods*, Lecture Notes in Physics, edited by A. Das and B. K. Chakrabarti (Springer Berlin Heidelberg, Berlin, Heidelberg, 2005) pp. 37–68.

BIBLIOGRAPHY

- [70] G. C. Knee and W. J. Munro, *Optimal Trotterization in universal quantum simulators under faulty control*, Phys. Rev. A **91**, 052327 (2015).
- [71] G. Rosenberg, M. Vazifeh, B. Woods, and E. Haber, *Building an iterative heuristic solver for a quantum annealer*, Comput Optim Appl **65**, 845–869 (2016).
- [72] A. G. Taube and R. J. Bartlett, *New perspectives on unitary coupled-cluster theory*, Int. J. Quantum Chem. **106**, 3393–3401 (2006).
- [73] R. J. Bartlett and M. Musiał, *Coupled-cluster theory in quantum chemistry*, Rev. Mod. Phys. **79**, 291–352 (2007).
- [74] X.-W. Guan, M. T. Batchelor, and C. Lee, *Fermi gases in one dimension: From Bethe ansatz to experiments*, Rev. Mod. Phys. **85**, 1633–1691 (2013).
- [75] K. M. O’Hara, S. L. Hemmer, M. E. Gehm, S. R. Granade, and J. E. Thomas, *Observation of a Strongly Interacting Degenerate Fermi Gas of Atoms*, Science **298**, 2179–2182 (2002).
- [76] G. B. Partridge, W. Li, R. I. Kamar, Y.-a. Liao, and R. G. Hulet, *Pairing and Phase Separation in a Polarized Fermi Gas*, Science **311**, 503–505 (2006).
- [77] K. Kim, M.-S. Chang, S. Korenblit, R. Islam, E. E. Edwards, J. K. Freericks, G.-D. Lin, L.-M. Duan, and C. Monroe, *Quantum simulation of frustrated Ising spins with trapped ions*, Nature **465**, 590–593 (2010).
- [78] B. S. Shastry, *Infinite Conservation Laws in the One-Dimensional Hubbard Model*, Phys. Rev. Lett. **56**, 1529–1531 (1986).
- [79] T. Prosen and M. Žnidarič, *Diffusive high-temperature transport in the one-dimensional Hubbard model*, Phys. Rev. B **86**, 125118 (2012).
- [80] J. E. Mooij, B. J. van Wees, L. J. Geerligs, M. Peters, R. Fazio, and G. Schön, *Unbinding of charge-anticharge pairs in two-dimensional arrays of small tunnel junctions*, Phys. Rev. Lett. **65**, 645–648 (1990).
- [81] R. Fazio and G. Schön, *Charge and vortex dynamics in arrays of tunnel junctions*, Phys. Rev. B **43**, 5307–5320 (1991).
- [82] A. Shnirman, G. Schön, and Z. Hermon, *Quantum Manipulations of Small Josephson Junctions*, Phys. Rev. Lett. **79**, 2371–2374 (1997).
- [83] V. Bouchiat, D. Vion, P. Joyez, D. Esteve, and M. H. Devoret, *Quantum coherence with a single Cooper pair*, Phys. Scr. **1998**, 165 (1998).
- [84] Y. Nakamura, Y. A. Pashkin, and J. S. Tsai, *Coherent control of macroscopic quantum states in a single-Cooper-pair box*, Nature **398**, 786–788 (1999).
- [85] J. J. García-Ripoll, E. Solano, and M. A. Martin-Delgado, *Quantum simulation of Anderson and Kondo lattices with superconducting qubits*, Phys. Rev. B **77**, 024522 (2008).
- [86] J. Q. You, Z. D. Wang, W. Zhang, and F. Nori, *Encoding a qubit with Majorana modes in superconducting circuits*, Scientific Reports **4**, 5535 (2014).
- [87] J. E. Mooij and Y. V. Nazarov, *Superconducting nanowires as quantum phase-slip junctions*, Nat. Phys. **2**, 169–172 (2006).
- [88] J. E. Mooij and C. J. P. M. Harmans, *Phase-slip flux qubits*, New J. Phys. **7**, 219 (2005).
- [89] O. V. Astafiev, L. B. Ioffe, S. Kafanov, Y. A. Pashkin, K. Y. Arutyunov, D. Shahar, O. Cohen, and J. S. Tsai, *Coherent quantum phase slip*, Nature **484**, 355–358 (2012).

BIBLIOGRAPHY

- [90] J. E. Mooij, G. Schön, A. Shnirman, T. Fuse, C. J. P. M. Harmans, H. Rotzinger, and A. H. Verbruggen, *Superconductor–insulator transition in nanowires and nanowire arrays*, New J. Phys. **17**, 033006 (2015).
- [91] J. Braumüller, M. Sandberg, M. R. Vissers, A. Schneider, S. Schlör, L. Grünhaupt, H. Rotzinger, M. Marthaler, A. Lukashenko, A. Dieter, A. V. Ustinov, M. Weides, and D. P. Pappas, *Concentric transmon qubit featuring fast tunability and an anisotropic magnetic dipole moment*, Appl. Phys. Lett. **108**, 032601 (2016).
- [92] M. Sarovar, J. Zhang, and L. Zeng, *Reliability of analog quantum simulation*, EPJ Quant. Technol. **4**, 1 (2017).
- [93] I. Schwenk and M. Marthaler, *Distortion of a reduced equilibrium density matrix: Influence on quantum emulation*, Phys. Rev. B **93**, 014305 (2016).
- [94] R. Barends, J. Kelly, A. Megrant, D. Sank, E. Jeffrey, Y. Chen, Y. Yin, B. Chiaro, J. Mutus, C. Neill, P. O’Malley, P. Roushan, J. Wenner, T. C. White, A. N. Cleland, and J. M. Martinis, *Coherent Josephson Qubit Suitable for Scalable Quantum Integrated Circuits*, Phys. Rev. Lett. **111**, 080502 (2013).
- [95] J. Salfi, J. A. Mol, R. Rahman, G. Klimeck, M. Y. Simmons, L. C. L. Hollenberg, and S. Rogge, *Quantum simulation of the Hubbard model with dopant atoms in silicon*, Nat. Commun. **7**, 11342 (2016).
- [96] U. L. Heras, L. García-Álvarez, A. Mezzacapo, E. Solano, and L. Lamata, *Fermionic models with superconducting circuits*, EPJ Quant. Technol. **2**, 8 (2015).
- [97] R. Barends, L. Lamata, J. Kelly, L. García-Álvarez, A. G. Fowler, A. Megrant, E. Jeffrey, T. C. White, D. Sank, J. Y. Mutus, B. Campbell, Y. Chen, Z. Chen, B. Chiaro, A. Dunsworth, I.-C. Hoi, C. Neill, P. J. J. O’Malley, C. Quintana, P. Roushan, A. Vainsencher, J. Wenner, E. Solano, and J. M. Martinis, *Digital quantum simulation of fermionic models with a superconducting circuit*, Nat. Commun. **6**, 7654 (2015).
- [98] D. Nigg, M. Müller, E. A. Martinez, P. Schindler, M. Hennrich, T. Monz, M. A. Martin-Delgado, and R. Blatt, *Quantum computations on a topologically encoded qubit*, Science **345**, 302–305 (2014).
- [99] D. Hangleiter, M. Kliesch, M. Schwarz, and J. Eisert, *Direct certification of a class of quantum simulations*, Quantum Sci. Technol. **2**, 015004 (2017).
- [100] K. Temme, S. Bravyi, and J. M. Gambetta, *Error Mitigation for Short-Depth Quantum Circuits*, Phys. Rev. Lett. **119**, 180509 (2017).
- [101] S. Lloyd, *Universal Quantum Simulators*, Science **273**, 1073–1078 (1996).
- [102] R. Babbush, D. W. Berry, I. D. Kivlichan, A. Y. Wei, P. J. Love, and A. Aspuru-Guzik, *Exponentially more precise quantum simulation of fermions in second quantization*, New J. Phys. **18**, 033032 (2016).
- [103] D. Banerjee, M. Bögli, M. Dalmonte, E. Rico, P. Stebler, U.-J. Wiese, and P. Zoller, *Atomic Quantum Simulation of $U(N)$ and $SU(N)$ Non-Abelian Lattice Gauge Theories*, Phys. Rev. Lett. **110**, 125303 (2013).
- [104] P.-L. Dallaire-Demers and F. K. Wilhelm, *Quantum gates and architecture for the quantum simulation of the Fermi-Hubbard model*, Phys. Rev. A **94**, 062304 (2016).
- [105] L. Lamata, A. Mezzacapo, J. Casanova, and E. Solano, *Efficient quantum simulation of fermionic and bosonic models in trapped ions*, EPJ Quant. Technol. **1**, 9 (2014).

BIBLIOGRAPHY

- [106] D. Poulin, M. B. Hastings, D. Wecker, N. Wiebe, A. C. Doberty, and M. Troyer, *The Trotter step size required for accurate quantum simulation of quantum chemistry*, QIC **15**, 361–384 (2015).
- [107] D. Willsch, M. Nocon, F. Jin, H. De Raedt, and K. Michielsen, *Gate-error analysis in simulations of quantum computers with transmon qubits*, Phys. Rev. A **96**, 062302 (2017).
- [108] C. Ballance, T. Harty, N. Linke, M. Sepiol, and D. Lucas, *High-Fidelity Quantum Logic Gates Using Trapped-Ion Hyperfine Qubits*, Phys. Rev. Lett. **117**, 060504 (2016).
- [109] X. Rong, J. Geng, F. Shi, Y. Liu, K. Xu, W. Ma, F. Kong, Z. Jiang, Y. Wu, and J. Du, *Experimental fault-tolerant universal quantum gates with solid-state spins under ambient conditions*, Nat. Commun. **6**, 8748 (2015).
- [110] J. Gaebler, T. Tan, Y. Lin, Y. Wan, R. Bowler, A. Keith, S. Glancy, K. Coakley, E. Knill, D. Leibfried, and D. Wineland, *High-Fidelity Universal Gate Set for $^9\text{Be}^+$ Ion Qubits*, Phys. Rev. Lett. **117**, 060505 (2016).
- [111] T. Gefen, D. Cohen, I. Cohen, and A. Retzker, *Enhancing the fidelity of two-qubit gates by measurements*, Phys. Rev. A **95**, 032314 (2017).
- [112] S. Debnath, N. M. Linke, C. Figgatt, K. A. Landsman, K. Wright, and C. Monroe, *Demonstration of a small programmable quantum computer with atomic qubits*, Nature **536**, 63–66 (2016).
- [113] I. D. Kivlichan, J. McClean, N. Wiebe, C. Gidney, A. Aspuru-Guzik, G. K.-L. Chan, and R. Babbush, *Quantum Simulation of Electronic Structure with Linear Depth and Connectivity*, Phys. Rev. Lett. **120**, 110501 (2018).
- [114] R. Steinigeweg, F. Jin, H. De Raedt, K. Michielsen, and J. Gemmer, *Charge diffusion in the one-dimensional Hubbard model*, Phys. Rev. E **96**, 020105 (2017).
- [115] C. D’Errico, M. Moratti, E. Lucioni, L. Tanzi, B. Deissler, M. Inguscio, G. Modugno, M. B. Plenio, and F. Caruso, *Quantum diffusion with disorder, noise and interaction*, New J. Phys. **15**, 045007 (2013).
- [116] J. Bylander, S. Gustavsson, F. Yan, F. Yoshihara, K. Harrabi, G. Fitch, D. G. Cory, Y. Nakamura, J.-S. Tsai, and W. D. Oliver, *Noise spectroscopy through dynamical decoupling with a superconducting flux qubit*, Nat. Phys. **7**, 565 (2011).
- [117] A. Aspuru-Guzik, A. D. Dutoi, P. J. Love, and M. Head-Gordon, *Simulated Quantum Computation of Molecular Energies*, Science **309**, 1704–1707 (2005).
- [118] J. Colless, V. Ramasesh, D. Dahlen, M. Blok, M. Kimchi-Schwartz, J. McClean, J. Carter, W. de Jong, and I. Siddiqi, *Computation of Molecular Spectra on a Quantum Processor with an Error-Resilient Algorithm*, Phys. Rev. X **8**, 011021 (2018).
- [119] L. Lamata, A. Parra-Rodriguez, M. Sanz, and E. Solano, *Digital-analog quantum simulations with superconducting circuits*, Adv. Phys. X **3**, 1457981 (2018).
- [120] J. R. McClean, M. E. Kimchi-Schwartz, J. Carter, and W. A. de Jong, *Hybrid quantum-classical hierarchy for mitigation of decoherence and determination of excited states*, Phys. Rev. A **95**, 042308 (2017).
- [121] D. Wecker, M. B. Hastings, N. Wiebe, B. K. Clark, C. Nayak, and M. Troyer, *Solving strongly correlated electron models on a quantum computer*, Phys. Rev. A **92**, 062318 (2015).
- [122] J. R. McClean, S. Boixo, V. N. Smelyanskiy, R. Babbush, and H. Neven, *Barren plateaus in quantum neural network training landscapes*, Nat. Commun. **9**, 4812 (2018).
- [123] Z. Jiang, K. J. Sung, K. Kechedzhi, V. N. Smelyanskiy, and S. Boixo, *Quantum Algorithms to Simulate Many-Body Physics of Correlated Fermions*, Phys. Rev. Applied **9**, 044036 (2018).

Danksagungen

Zuerst möchte ich mich bei Prof. Gerd Schön dafür bedanken, mir eine Doktorandenstelle am Institut für Theoretische Festkörperphysik angeboten zu haben sowie für all seine Bemühungen und die Unterstützung während meiner wissenschaftlichen Arbeit. Des Weiteren möchte ich Prof. Alexander Shnirman dafür danken, sich als Korreferent dieser Dissertation zur Verfügung gestellt zu haben.

Ich blicke gern auf meine Zeit an diesem Institut zurück, die schon eine Weile vor der Doktorarbeit mit Hauptseminar, sowie Bachelor- und Masterarbeit begann. Ich empfand die Arbeitsatmosphäre immer als sehr angenehm, was nicht nur an guten Voraussetzungen zum Arbeiten, wie der hervorragenden IT-Infrastruktur liegt, oder der Möglichkeit beim Nachdenken den Blick aus dem elften Stockwerk über Karlsruhe bis zum Schwarzwald schweifen zu lassen, sondern vor allem auch an den Kollegen: Es gab zahlreiche spaßige Momente zusammen mit meinen Mitstreitern zur Promotion, besonders Christian Karlewski, Daniel Mendler, Iris Schwenk und Sebastian Zanker – nicht nur während der Arbeitszeit, sondern zum Beispiel auch bei einer Runde Basketball oder Billard.

Ich bedanke mich außerdem bei Michael Marthaler für die Betreuung während meiner Doktorarbeit. Ich bin gespannt, wo uns die weitere Zusammenarbeit, auch mit Iris und Sebastian, hinführen wird.

Nicht zu vergessen ist schließlich die Unterstützung von Seiten von Familie und Freunden, auf die ich mich immer verlassen konnte. Besonderer Dank geht an Lena, für viel Verständnis und Geduld in der letzten Zeit.

